UMBC

DISSERTATION APPROVAL SHEET

Title of Dissertation: AERODYNAMIC ANALYSIS OF STATIONARY AND FLAPPING WINGS IN UNSTEADY FLOW ENVIRONMENTS AT LOW REYNOLDS

Name of Candidate: Naresh Poudel

Doctor of Philosophy, 2022

Graduate Program: Mechanical Engineering

Dissertation and Abstract Approved:

Melin Yu

Melin Yu
Associate Professor
Department of Mechanical Engineering
4/29/2022 | 9:14:17 AM EDT

Dr. John T. Hrynuk

Dr. John T. Hrynuk
Special Member, Graduate Faculty
Department of Mechanical Engineering
4/29/2022 | 9:54:27 AM EDT

NOTE: *The Approval Sheet with the original signature must accompany the thesis or dissertation. No terminal punctuation is to be used.

ABSTRACT

Title of dissertation: AERODYNAMIC ANALYSIS OF STATIONARY AND FLAPPING WINGS IN UNSTEADY FLOW ENVIRONMENTS AT LOW REYNOLDS NUMBERS

Naresh Poudel, Doctor of Philosophy, 2022

Dissertation directed by: Professor Meilin Yu
Department of Mechanical Engineering
John T. Hrynuk
Combat Capabilities Development Command
U.S. Army Research Lab

This thesis investigates nonlinear flow physics of flapping wings in unsteady ambient flow environments at low Reynolds numbers, where most birds, insects, and small unmanned aerial vehicles (UAVs) maneuver or operate, with high-fidelity numerical simulations enabled by high-order accurate computational fluid dynamics (CFD) methods.

The first objective of this research is to investigate gust-wing interaction and to unravel the mechanism of gust mitigation with flapping wings. The interaction of a gust with a stationary airfoil produces large undesirable unsteady forces, which exceed the peak static lift coefficient. A simple pitch-down maneuver and oscillating airfoil motion were tested to mitigate the gust. A rapid pitch-down maneuver in response to a gust sometimes exceeds the negative stall angle, causing an inadvertent stall. A step-wise change in the angle of attack, as the gust develops, is shown to

be effective at mitigating the negative effects of the gust. However, if the gust continues to grow in magnitude, this strategy may be ineffective. Low amplitude wing oscillations are then tested as a novel method for gust mitigation. Increasing the oscillating airfoil's reduced frequency dominates the gust.

The second objective of the research is to examine highly nonlinear flow physics of stationary/flapping wings in unsteady ambient flow environments at low Reynolds numbers. The dependence of a pitching airfoil's thrust on Reynolds and Strouhal numbers is investigated first, and it is discovered that an unsteady flow environment can enhance its thrust production. The thrust scaling law of a pitching airfoil, when operating in highly unsteady flow environments, is extended as a function of Reynolds number, Strouhal number, and turbulence intensity. To quantify the effect of the unsteady flow environment on pitching airfoil thrust production, an effective Reynolds number concept is also introduced. It is also found that moderate freestream turbulence ($\sim 5\%$) can alter the formation of laminar separation bubbles near a stationary wing's leading edge and obtain larger lift coefficients when compared to those in a uniform freestream. This is critical for UAV design and control at low Reynolds numbers as large-scale flow separation can create undesired stall effects over wings at moderate angles of attack due to the weak resistance of unfavorable pressure gradients at low Reynolds numbers.

In conclusion, on using high-fidelity numerical simulation tools, this research contributes to novel design and control of future unconventional UAVs by providing key insights into unsteady aerodynamics in highly unstructured real-world flight environments.

AERODYNAMIC ANALYSIS OF STATIONARY AND FLAPPING WINGS IN UNSTEADY FLOW ENVIRONMENTS AT LOW REYNOLDS NUMBERS

by

Naresh Poudel

Dissertation submitted to the Faculty of the Graduate School of the
University of Maryland, Baltimore County in partial fulfillment
of the requirements for the degree of
Doctor of Philosophy
2022

Advisory Committee:
Professor Meilin Yu, Chair/Advisor
Dr. John T. Hrynuk, Co-Advisor
Professor Ruey-Hung Chen
Professor Charles Eggleton
Professor Liang Zhu

Dedication

To my family and friends

Acknowledgments

First and foremost, I would like to express my heartfelt gratitude and appreciation to my advisor, Professor Meilin Yu, for giving me the opportunity to work on this challenging project during my graduate studies. I am grateful to him for his invaluable guidance, unending patience, and encouragement in completing this work. I'd also like to thank my co-adviser, Dr. John T. Hrynuk, for his advice and support. This work would not have been possible without his experimental results validating our CFD Solver. I'd like to express my gratitude to my committee members, Professor Ruey-Hung Chen, Professor Charles Eggleton, and Professor Liang Zhu, for their time and comments.

This Research was sponsored by the U.S. Army Research Laboratory (ARL) and was accomplished under Cooperative Agreement Number W911NF-20-2-0028 through Oak Ridge Associated Universities (ORAU). I am grateful to ORAU and ARL for providing me with the Journeyman fellowship to carry out this research.

I'd like to thank the UMBC High Performance Computing Facility (HPCF) for providing the computational resources and the staff for their technical assistance. Special thanks to the staff and faculty of the UMBC Mechanical Engineering department for their kind assistance and support throughout this journey. I'd also like to thank Dr. Devdas Shetty, Dr. Abose Adebayo, Dr. Kate Klein, Dr. Pawan Tyagi, Dr. Jiajun Xu, and Surya Chapagain for their invaluable advice and encouragement in helping me achieve my goal. Finally, I'd like to express my heartfelt gratitude to my family and friends.

Table of Contents

List of Tables

List of Figures

List of Abbreviations

A	Area
A_{pitch}	Pitching amplitude of the trailing edge of the airfoil
α	Angle of attack
c	Chord length of the airfoil
d	Cylinder diameter
C_D	Drag coefficient
C_L	Lift coefficient
C_P	Power coefficient
C_T	Thrust coefficient
f	Frequency
F_x	Force in horizontal direction with respect to the position of airfoil
F_y	Force in vertical direction with respect to the position of airfoil
k	Reduced frequency
L	Distance between cylinders
s	Spanwise length
St	Strouhal number
t	Dimensional time
t^*	Non-dimensional time
θ_0	Amplitude of the pitching angle
ϕ	Initial phase angle
θ_m	Mean angle of attack
U_∞	Freestream velocity
2D	Two dimensional
3D	Three dimensional
ARL	U.S. Army Research Lab
CFD	Computational Fluid Dynamics
DNS	Direct Numerical Simulation
ESDIRK	Explicit First Stage, Singly Diagonally Implicit Runge-Kutta
FR/CPR	Flux Reconstruction/Correction Procedure via Reconstruction
GR	Gust ratio
LES	Large Eddy Simulation
LEVs	Leading Edge vortices
LSB	Laminar Separation Bubble
MAV	Micro Air Vehicle
MEMS	Micro Electro-Mechanical Sensor
MTG	Medium Turbulence Generator
NACA	National Advisory Committee for Aeronautics
PSD	Power Spectral Density
Re	Reynolds number
TEVs	Trailing Edge Vortices
TG	Turbulence Generator
UAV	Unmanned Aerial Vehicle

Chapter 1: Introduction

1.1 Motivation

Studying aerodynamics at low Reynolds (Re) numbers, associated with fixed and flapping wings, has attracted extensive attention of researchers with the hope to better design Micro Air Vehicles (MAVs), small unmanned aerial vehicles (UAVs), and small-scale wind turbines [1]. In this work the low Reynolds number regime is defined as a wing chord length-based Reynolds number range of $10^4 - 10^5$. During the early stage of flight development, the research focus was on the design of aircraft that could fly faster and higher with increased payload, reliability, safety, and low cost. Conventional aerodynamics focused on steady and high Reynolds number flow was widely studied for over a century. Nowadays, due to the advancement of Micro Electro-Mechanical Sensor (MEMS) and actuators, unmanned flight at the size of insects and birds has become more feasible [2]. Birds and insects also provide examples of systems that can alleviate the adverse effects of unsteady ambient flows, but man-made vehicles cannot yet match this performance. Most studies on flapping wing aerodynamics at low Reynolds numbers have neglected the effect of highly unsteady environments such as gusts or turbulence on the aerodynamic performance of flapping wings [3–8]. However, the basic understanding of how flying and swimming animals can mitigate the turbulence, gusts, and vortices developed due to the upstream objects/obstacles, atmospheric conditions, or ground effects remains largely unknown. This motivates us to investigate the underlying aerodynamics of stationary and flapping wings in unsteady flow environments.

1.2 Problem Statement

MAVs and small-scale UAVs operate in the low Reynolds number regime of $10^4 - 10^5$. As the size of MAVs become smaller, its weight shrinks as shown in 1.1, and as a consequence they have unfavorable aerodynamic characteristics, like having a low lift-to-drag ratio [9] and easy to be affected by unsteady flow environments, such as gusts [10]. The aerodynamic performance of wings at low Reynolds numbers is different from that at high Reynolds numbers due to thick boundary layers, severe flow separation, and laminar-turbulent transition [11,12]. There exists strong nonlinearity in low-Reynolds-number flow around airfoils since the increasing viscous effects, with respect to inertial effects, can substantially influence the boundary layer physics such as separation, transition and reattachment. These events can all occur within a short distance and significantly affect the performance of the lifting surface [9]. Often the separated shear layer does not reattach on the surface and large wake is formed in the low Reynolds number range.

Due to their small size and low speed, MAVs are prone to encounter flight control issues due to ambient unsteady flow environments, such as strong wind gusts [10]. These unsteady loads caused by cross-wind and vertical gusts play a

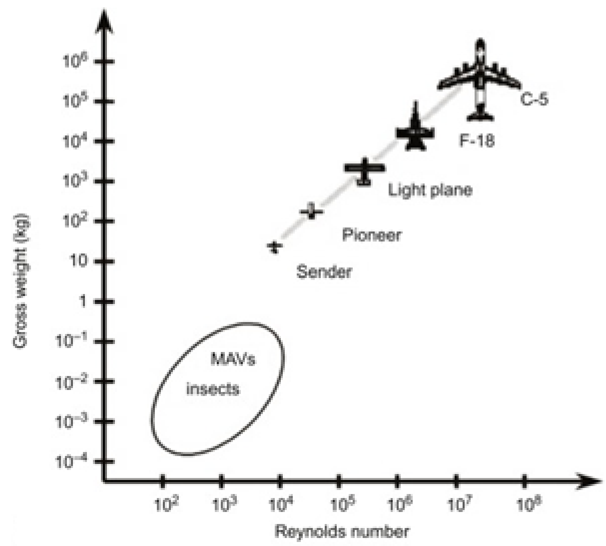

Figure 1.1: Classification of air vehicles based on their mass and Reynolds number [13].

significant role in the design and operation of MAVs. Early in aviation history, gust research focused primarily on the response of large aircraft [14], but these tests seldom reflect the aerodynamic conditions experienced by MAVs. Due to the gusty wind conditions in low atmospheric urban areas and the relative speed of the vehicle, MAVs may experience large changes in freestream speed and angle of attack as shown in 1.2.

Flow in the low-Reynolds-number regime is highly dictated by the nonlinear mechanisms and resolving the unsteady flow features more accurately due to non-linearity is challenging. In numerical studies the accurate prediction of lift and drag forces under the higher turbulence level environment is challenging [16–19]. Olson *et al.* [17] suggested that the accurate characterization of separation bubbles over an airfoil at low Reynolds numbers is also particularly challenging and discrepancies appears in experiments and computations due to facility dependent freestream turbulence level and other experimental uncertainties. Coder and Maughmer [18]

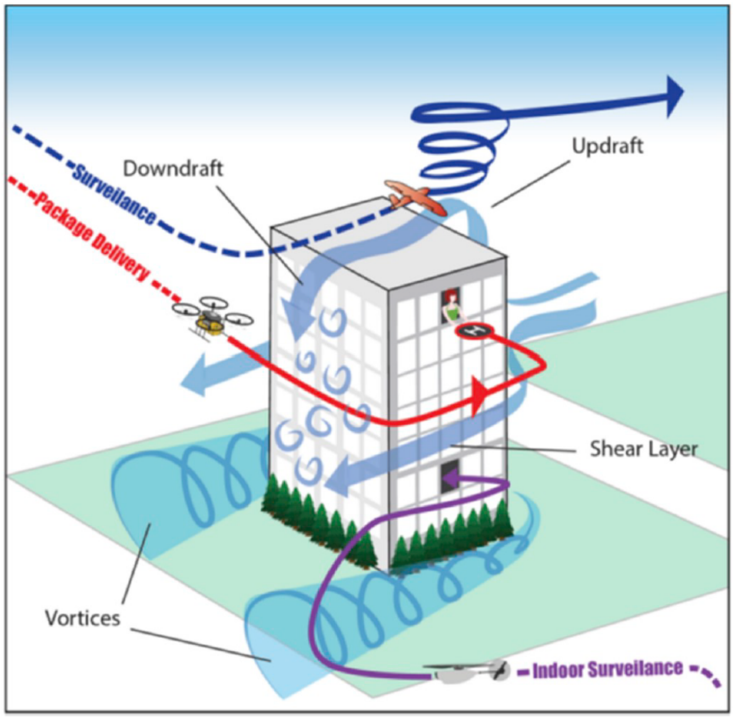

Figure 1.2: Schematic of MAVs operating in urban may encounter a variety of flow environments caused by the interaction of atmospheric wind with buildings [15].

observed that theoretical methods tend to over-predict the maximum lift coefficient when compared with experimental results for airfoils at low Reynolds numbers. High-order computational fluid dynamics (CFD) methods have been proven more accurate and efficient than the conventional methods at capturing complex flow structures [20, 21]. However, simulating freestream turbulence and its interaction with the boundary layer is still challenging in computational studies. Therefore, in this study, High-order CFD methods are used to accurately unravel the complex flow phenomena due to unsteady flow conditions. There exists rich flow physics in the interaction between unsteady flow environments, such as freestream turbulence and vertical gusts on airfoil performance at low Reynolds numbers ($10^4 < Re < 10^5$).

The impact of these unsteady flow environments on the wing performance is not well understood. The proposed research will investigate the fundamental flow physics underlying boundary layer development over stationary and flapping wings in the presence of the freestream turbulence and vertical gusts. It will also characterize the corresponding aerodynamic performance of airfoils in these flows. In addition, a series of high-order numerical simulations will be compared to determine the model fidelity required to accurately predict airfoil performance under highly unsteady flow conditions. The results from these simulations will also be compared with experimental results.

1.3 Outline of Dissertation

The remainder of the dissertation is organized as follows. A literature review highlighting previous attempts to study the effects of gust interactions with stationary/flapping wings and unsteady freestream flow conditions is presented in Chapter 2. The introduction of the high-order Flux Reconstruction (FR) method, dynamic mesh deformation algorithms, and solver validation are presented in Chapter 3. Chapter 4 discusses the interaction of a vertical gust and stationary/flapping wings, as well as gust mitigation strategies using flapping wings. Chapters 5 and 6 discuss the effects of unsteady freestream on the propulsive performance of a 2D flapping airfoil and the aerodynamic performance of a 3D stationary wing at low Reynolds numbers, respectively. Chapter 7 concludes with the work's conclusions and recommendations for future research.

Chapter 2: Literature Review and Research Objectives

This chapter will provide an overview of the existing literature on the effect of vertical gust and unsteady freestream on the performance of stationary and oscillating airfoils. The research objectives of this thesis are outlined at the end based on the gaps identified from the literature review.

2.1 Previous Studies on the Interaction between Gusts and Stationary Wings

In addition to turbulence, large amplitude unsteady disturbances like gusts are also common for small flying vehicles. Study of the fundamental response of airfoils to vertical gusts is key to the development of active and passive gust rejection methods for future MAVs. Küssner [22], and von Karman and Sears [23] pioneered the study of the interaction between a thin airfoil and a sharp edged gust with a small amplitude using the unsteady thin airfoil theory. Following studies usually focused on modeling small amplitude transient and oscillating vertical gusts, where a small change in the wing AoA (α) was modeled as a transient lift effect. These methods include Wagner's indicial function and Küssner's function for estimating the lift changes during a gust encounter. These methods assume low gust ratios, inviscid flows, and attached flow conditions. While these methods are reflective of large-scale aircrafts interacting with updrafts, they do not match the gusts experiences by modern MAVs. Recent work by Smith *et al.* [24,25] demonstrated a vertical gust in a wind tunnel environment that bears little resemblance to the flow conditions required for traditional gust models, but more closely matched MAV flight environments. Many recent experimental and numerical studies have been carried out to study nonlinear, high magnitude gust-wing interactions [26–36].

Experimental studies on gust-wing interaction are always limited by the methods that researchers have used to generate gusts in the experimental setting. For example, a diffuse vortex generated upstream of test models has commonly been used as a type of gust [37,38], but this method has some drawbacks. While the generated vortex has diffused before hitting the model, this method can only provide transient up- and down-draft behaviors. Another common gust generation method is to mimic a gust by moving the wing itself, e.g., through a plunge motion [39]. Plunging wings are effective at mimicking a gust, but it remains unknown the extent of the differences between moving-body and moving-fluid gust interactions. Tow tank studies [32] produce high quality results but are usually limited in their transient nature, where the wing must keep moving to maintain its forward velocity while it passes through the vertical gust. This limits the ability to create a step-function-like gust, which would simulate a MAV flying into an updraft longer than the vehicle itself. This tow-tank gust method has been the most heavily studied in recent years including numerical comparisons. Biler *et al.* [40] performed experimental and computational studies and found that leading edge effective AoA is responsible for the

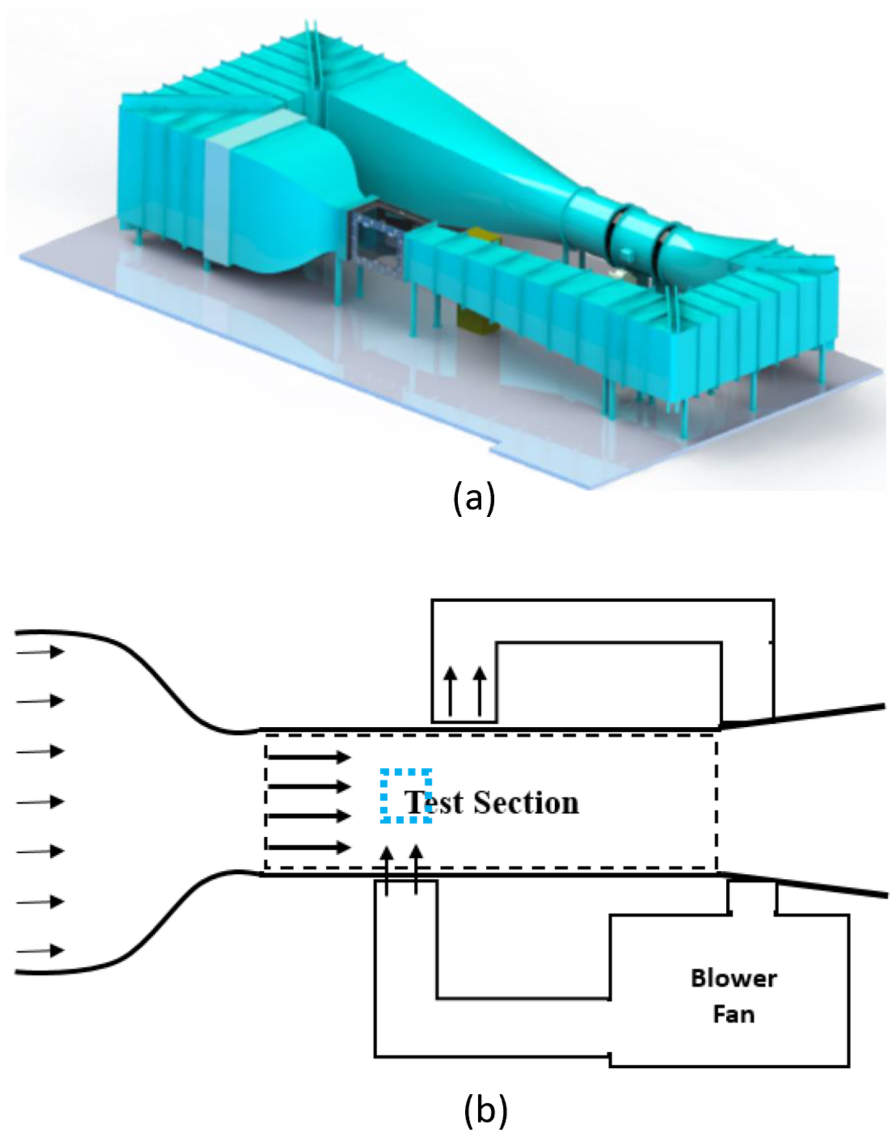

Figure 2.1: (a) Microsystem Aeromechanics Wind Tunnel (MAWT) facility at ARL and (b) Sketch of vertical gust generator [24, 25]

peak lift coefficient, rather than gust ratio or geometric AoA. Badrya *et al.* [41], [42] compared the experimental results of Perrotta and Jones [32] and their numerical ones, with a goal of widening the gust in a numerical environment. Their results showed that the maximum lift peak increases with the gust width and asymptotically reaches to a stable value, which suggests that a longer gust generates a different result when compared to shorter, more transient gusts.

The gust-wing interaction studies done previously move the wing through the gust, and the time duration of gust wing interaction is very short. In real scenarios, the gust effects of the wing could be longer and the change in effective angle of attack that the wing can experience may be larger.

2.2 Previous Studies on the Effects of Unsteady Freestream and Vertical Gusts over Flapping Wings

Many studies have been conducted to investigate the flight instabilities of flapping or oscillating wings in gusty or turbulent conditions. Objects such as circular cylinders in tandem configurations with flapping wings placed downstream are commonly used in these studies. Sometimes the shedding frequencies of these upstream bodies are used to mimic gust conditions. Shyy *et al.* [43] performed an experimental and numerical study on rigid and flexible airfoils under the effects of gust. They demonstrated that the flexible airfoil performs better under gust conditions than the rigid airfoil, specifically in terms of lift to drag ratio. Prater and Lian [44] numerically studied the flight characteristics of stationary and flapping wings in a single and tandem wing configuration. The wings were tested under uniform flow with sinusoidal velocity inflow conditions to model an oscillating gust. Lian and Shyy [45] found that when the flow accelerates/decelerates, the transition position moves upstream/downstream due to the increasing/decreasing Reynolds number under a gusty flow. Jones and Yamaleev [31] numerically studied the performance of flapping wings under the influence of different gust conditions, namely frontal, downward, and side gust. They demonstrated that flapping wings can effectively recover from the gust fluctuations they tested. Lian [28] conducted another numerical study of flapping wings and reported that the gust fluctuations effects can be alleviated under different flapping frequencies and amplitudes. Gao and Lu [46] reported three different behaviors observed for force production of flapping wings in ground effects. Specifically they observed periods of force enhancement, force reduction, and force recovery, which are closely associated with the evolution of vortex structures due to ground effects in insect normal hovering.

The performance of two-dimensional (2D) oscillating airfoils subject to sinusiodal gusts has been studied by Lian and Shyy [27, 28] and three-dimensional (3D) flapping wings subject to discrete gusts have been studied by Jones and Yamaleev [31]. It has been shown in these studies that flapping wings can be more resistant to gusts and freestream turbulence [31, 47]. There are also parallel efforts studying the flight performance of flying insects in gusty environments [47–52], and turbulence conditions [53–59]. Nakata *et al.* [60] showed that flexible flapping wings can be beneficial for longitudinal gust mitigation. Badger *et al.* [61] found that the use of a deflectable tail on a glider model can enhance the stability of Anna's hummingbirds flying into a vertical gust. Jakobi *et al.* [62] studied the effects of gusts impinging from different directions on bumblebees and found that bees can mitigate the gust influence by using different maneuvering strategies. Cheney *et al.* [59] also reported that birds can mitigate gusts through a complex variety of inertial and aerodynamic mechanisms.

More work has been done in the area of dynamic stall in unsteady environments, using oscillating inflow velocity conditions [63–66], turbulence grids [67–69] and upstream cylinders to create disturbances [70,71]. In the presence of freestream turbulence, these studies demonstrated a delay in boundary-layer separation and a smaller separation bubble over the maneuver's surface. When the turbulence intensity is increased, the dynamic stall process is delayed to higher incidence angles [72]. Gharali and Johnson [66] conducted a two-dimensional (2D) numerical study of a pitching airfoil with the unsteady inflow velocity to investigate the velocity phase difference between the freestream velocity oscillation and the pitching pattern oscillation, similar to Favier's experiment [63]. This work indicated that for in-phase oscillations, the lift could be about 5 times greater than that in the static freestream and this value could be amplified as the reduced frequency increased. Yu *et al.* [67] used particle-image velocimetry to study dynamic stall in a water tunnel with turbulence intensities of 0.5 and 6.9% at low Reynolds number, Re = 4,500. They found that higher turbulence intensity (6.9%) delays the dynamic stall event due to a reduction in velocity deficit and flow reversal. Amandolése and Széchényi [68] demonstrated that the lift overshoot hysteresis loop decreased with increasing turbulence. The experimental study by Li *et al.* [69] also discovered that the size of the hysteresis loop caused by dynamic stall gradually decreases with increasing turbulence intensity. Chen and Choa [70] performed an experimental study on the effect of turbulent wakes on a pitching airfoil. In this work, a small cylinder was placed upstream at different vertical positions relative to the pitching airfoil at Reynolds number 80,000 with low reduced frequencies ($k = 0.01 - 0.04$). They compared the aerodynamic forces and moments with those from the undisturbed freestream case, where they observed that dynamic stall occurs at higher angles of attack due to the turbulent wake. The growth of the leading-edge suction peak was also found to be particularly sensitive to the vertical position of the cylinder. Merrill and Peet similarly [71] studied a pitching airfoil in the presence of a turbulent wake produced by an upstream small cylinder. Their study showed that in the presence of upstream wake turbulence the magnitude of drag and pitching moment were greatly reduced over the majority of the pitching cycle. They also found that dynamic stall starts at a later time and at higher angles of attack due to delayed formation and detachment of the dynamic stall vortex. Conger and Ramaprian [73] investigated a pitching NACA 0015 airfoil in a water channel with a relatively high level of freestream turbulence (0.8–1.0%) compared to other water tunnels. They reported a greater magnitude of pressure and aerodynamic forces in their study than was previously reported for similar pitch rates, implying that turbulence effects may extend to dynamic motions of wings. Kay *et al.* [74] demonstrated similar effects as the other studies but at higher Reynolds number (50,000-200,000) and higher turbulence intensities (5-15%).

We also notice that fish swimming in an unsteady environment have been studied extensively, both experimentally and numerically, to see how they can use it to their advantage. In these studies, upstream objects like circular cylinders or D-cylinders are placed upstream of the pitching foils to characterize the aerodynamic characteristics and propulsion efficiency of the foils. Gopalakrishnan *et al.* [75] performed an experiment with a heaving and pitching NACA0012 airfoil in the wake of a heaving D-cylinder. They identified three distinct wake structures in the airfoil, i.e., expanding wake, destructive interaction wake, and constructive interaction wake between the airfoil motion and the vortex street. Liao *et al.* [76–78] conducted experiments on rainbow trout downstream of the D-section cylinder and observed that fish synchrorise their body kinematics to extract energy from incoming vortices. Furthermore, Akayeti and Liao [79] proposed a Karman gait analytical model that fully describes rainbow trout responses to vortex street based on the experiments. In the numerical study by Chao *et al.* [80], they found that the propulsion efficiency was affected by the lateral gap of the D-cylinders, the lateral distance between the D-cylinder and the airfoil, and the oscillating frequency of the airfoil. Xiao *et al.* [81] also did a numerical study on the performance of the undulating NACA0012 foil behind the wake of a D-cylinder and revealed that the foil's thrust coefficient improves with the presence of the upstream D-cylinder. Shao *et al.* [82] numerically studied the interaction between a flapping airfoil in the wake of an oscillating D-cylinder. They discovered that during the expanding wake and destructive interaction modes, the strong interaction of the incoming vortices with the airfoil induced low pressure at the leading edge, resulting in a large thrust, whereas in the constructive mode, the interaction with the incoming vortices is weak, and the thrust is increased only slightly compared to the other two modes. Li *et al.* [83] investigated the hydrodynamics of foil in the streets of the D-cylinder, quantifying the effects of the foil–vortex phase and downstream distance on vortex energy extraction efficiency, hydrodynamic force coefficients, and wake structures using the Kármán gaiting model. Shao *et al.* [84] investigated the interaction between an undulating foil and a passing vortex numerically. The impacts of several controlling parameters on the thrust and input power are explored, including the distance between the foil and the D-cylinder, the frequency and phase angle of the foil's undulation, and the phase angle of heaving motion.

2.3 Previous Studies on the Effects of Unsteady Freestream on Stationary Wings

The influence of freestream turbulence on airfoil performance is significant, especially at low Reynolds numbers. In this low Reynolds number range the size and location of Laminar Separation Bubbles (LSBs) are altered due to the presence of freestream turbulence. The freestream turbulence can be quantified by turbulence intensity which is defined as the ratio between the standard deviation of the velocity fluctuation to the mean velocity. These flow features typically modify airfoil performance by increasing the maximum lift coefficient, resulting in an airfoil that behaves similar to its performance at higher Reynolds number.

Stack [85] in 1931 conducted one of the first wind tunnel experiments on airfoils with and without turbulence grids to study the effects of freestream turbulence. Stack found that an increase of the turbulence level can significantly increase the maximum lift coefficient. Mueller *et al.* [86] studied the influence of freestream turbulence on the aerodynamic performances of a Lissaman 7769 airfoil at Reynolds number of 1.5×10^5. They observed typical hysteresis characteristics in the lift and drag coefficients at low freestream turbulence intensity (around 0.10

% of freestream). Increasing or decreasing of angle of attack results in different lift and drag coefficients at the same angle of attack based on history of flow is defined as hysteresis as shown in Figure 2.2. This hysteresis is associated with the laminar separation and flow reattachment behaviors of an airfoil [11]. This hysteresis in the lift and drag curves disappeared as freestream turbulence intensity was increased to 0.30 % by causing the flow to reattach to the upper surface of the airfoil at higher angles of attack.

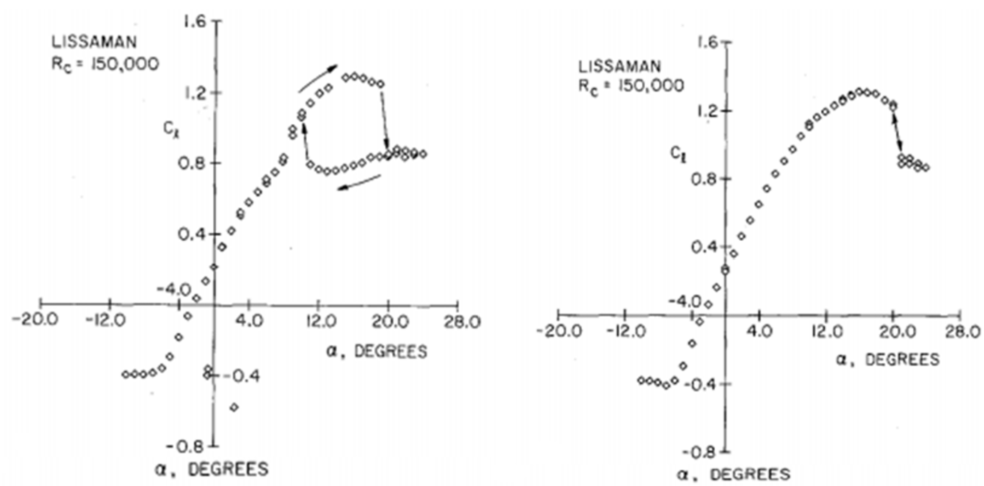

without turbulence screen　　with screen turbulence screen

Figure 2.2: An Example of Hysteresis Effect [86].

Hoffmann [87] performed an experimental study on a NACA0015 airfoil at Reynolds number of 2.5×10^5, varying the turbulence intensities from 0.25% to 9.0%. Their results showed that freestream turbulence increased the maximum lift coefficient by up to 30 %. Laitone [88] measured the lift and drag for Reynolds numbers less than 70,000 on a NACA0012 airfoil, a thin flat plate and a cambered plate. The NACA0012 airfoil was observed to be particularly sensitive to Reynolds number variations and upstream turbulence level at low Reynolds numbers, whereas flat and cambered plates were not. Mish and Devenport [89] and Gilling *et al.* [90] also showed that an increase in turbulence intensity can enhance the maximum lift for a NACA0015 airfoil at much higher Reynolds numbers, $1.17 - 1.5 \times 10^6$. Huang and Lee [91] studied the freestream turbulence effects on the aerodynamics characteristics of a NACA0012 airfoil at Reynolds number $0.5-1.5\times10^5$ with varying turbulence intensities from 0.2 % to 0.65 %. Their study showed that the increase in the maximum lift coefficient is significant when the turbulence intensity increases. Their results also showed that the when turbulence intensity is smaller than 0.45 % the turbulence delayed stall, but further increasing turbulence didn't further delay stall. Wang *et al.* [92] found that the freestream turbulence has more influence on the shear layer separation, reattachment, transition, and formation of the separation bubble at low Reynolds numbers compared to higher Reynolds number. Devinant *et al.* [93] performed the wind tunnel experiments on NACA 654-421 airfoil varying turbulence levels of 0.5-16 % and also found that the higher turbulence level can increase the maximum lift.

A laminar separation bubble occurs when a laminar boundary layer on the suction side of a wing lifts off the surface and reattaches further downstream. The region enclosed by the laminar separation point and the point of turbulence reattachment is called the laminar separation bubble (LSB). At low Reynolds number the flow is particularly susceptible to the formation of LSBs and adverse pressure gradients causing early separation and stall. Long separation bubbles are found in low Reynolds number flows which also significantly influences the pressure and velocity distributions over the airfoil. As such, LSBs are a key flow feature at low Reynolds numbers and often determine the performance of airfoils.

An increase in turbulence intensity can eliminate or shorten the length of laminar separation bubbles [94]. Bursting of these laminar separation bubbles, where the bubble collapses and flow separates, is a common cause of stall at low Reynolds numbers. Sicot *et al.* [95] showed that the oscillating length the LSB increases when the LSB separation point moves towards the leading edge, occurring at higher angles of attack and near stall. Flows with small-scale free stream turbulence exhibit a smoother behavior in the near-stall region. Studies done by Cruz [94], Tsuchiya *et al.* [96], Ravi *et al.* [97] and Delnero *et al.* [98] all showed that the stall angle is increased with increased freestream turbulence. The studies conducted by Cruz [94] and Ravi *et al.* [97] also showed that the increase in freestream turbulence levels results in an increase in C_{Lmax}, but this was not observed in other studies and appears to be dependent on the airfoil and Reynolds numbers.

Breuer [99] performed numerical investigations on the effect of inflow turbulence on a SD7003 airfoil at Reynolds number of 60,000 and an angle of attack 4° with turbulence intensities varying between 0 % to 11.2 % using large eddy simulation (LES). Results showed that the increase in the turbulence intensity can delay flow separation on the suction side of the airfoil, and the boundary layer transition to turbulence occurred earlier. The study also suggests that by decreasing length and time scales of the turbulence have the similar effects observed for increasing the turbulence intensity. Yang and Abdalla [100] also used an LES approach to simulate flow over a flat plat with 2 % turbulence intensity at a Reynold number of 6,500. They found that the turbulence causes earlier transition and the instability mechanism, i.e., Kelvin-Helmholtz instability without freestream turbulence, is present in the case with turbulence. Balzer and Fasel [101] and Hosseinverdi and Fasel [102] used direct numerical simulation (DNS) to investigate influence of turbulence on a flat plate with 0.1 % - 0.3 % turbulence intensities. They found a fast boundary layer transition due to the increase in turbulence intensity reducing the separation bubble length. They showed that 3D Klebanoff-modes (streamwise streaks) are formed inside the boundary layer by the freestream turbulence.

2.4 Research Objectives

The current understanding of both steady and unsteady aerodynamics of stationary and flapping wings are primarily based on uniform flow conditions, but this is not reflective of the operating environment of small UAVs. Basic understanding of the flow physics of stationary and flapping wings under non-uniform flow conditions at low Reynolds numbers is lacking. The specific objectives of the proposed research are to investigate the effects of highly unsteady flow conditions, caused by gusts and turbulence, on airfoil performance and how to mitigate the negative effects of this unsteadiness. In the proposed work, unsteady flow conditions will be modeled by modeling a vertical gust generator based on previous wind tunnel tests by Smith *et al.* [24, 25] and by placing different configurations of upstream cylinders to generate turbulence. These configurations will be used to help determine the effects of upstream turbulence and gusts on airfoils at low Reynolds number with implications for design of small UAVs.

2.4.1 Objective 1 – Gust mitigation

The first objective of this research is to *investigate a mechanism of gust mitigation using oscillating wings.* Typically gust-wing interactions are studied over a short interaction time but the approach in the proposed research is to model the vertical gust similar to the gust generator developed in the U.S. Army Research Lab (ARL) [24, 25]. This gust generator creates a vertical gust similar to an updraft an MAV may encounter in the real world. Current understanding of gusts is usually limited by the methods researchers have used to develop vertical gusts in an experimental setting. While CFD studies of gust interactions are not uncommon, they are seldom compared directly to experimental results. This study plans to undertake a comparison of gust wing interaction simulated experimentally with a vertical gust generator in a wind tunnel environment and numerically with advanced unsteady CFD tools. This CFD model will be used to further explore extremely time-consuming experimental variables, such as turbulence reduction, and widen the understanding of mechanism of gust generation in a wind tunnel.

Recently, simple control techniques have been applied to mitigate gust effects. Sedky *et al.* [103,104] used both closed- and open-loop strategies to control the pitch motion to mitigate the gust effect. Andreu-Angulo and Babinsky [105, 106] used a pitch-down motion control to maintain a zero mean effective AoA during the gust encounter. It should be noted that these experiments in water allowed for response to large magnitude gusts and do not necessarily scale well for air vehicles. In these studies, the duration of the gust acting on the wing is short. The impact of the gust on the wing for a long-duration gust can be significantly different.

Similar to the study of smaller scale unsteadiness (turbulence), this study will also evaluate oscillating airfoils experiencing a gust. When the Strouhal number and reduced frequency fall in an optimal range where the airfoil produces thrust, gust-wing interactions are likely to be dominated by the wing kinematics. Using oscillating motions has potential to mitigate the detrimental effects of the gust.

In summary, the following specific research will be presented on Gust Mitigation :

1. Characterization of dominant flow features in the interaction between a vertical gust and a wing, either fixed or under oscillation.

2. An investigation of gust mitigation mechanisms using an oscillating wing motion.

2.4.2 Objective 2 - Turbulence effects

The second objective of this research is to *explore the flow physics and influence of unsteady freestream on the aerodynamic performance of static and oscillating airfoils*. Using experiments to widen the understanding of underlying mechanisms of flow- structure interactions are not always possible, so using high-fidelity numerical simulation will help to quickly investigate the flow physics. The effects of unsteady flow will be investigated for both oscillating wing motions and on a static airfoil. A previous study done by Visbal [107] on plunging motion of an airfoil showed the lift coefficient from the 2D and 3D simulations were independent of Reynolds number and three-dimensional transitional flow under uniform flow conditions. However, this has not yet been studied with an unsteady freestream condition. The following research questions will be answered:

- Is the freestream turbulence or the oscillation motion of the wing more important to the end flow state?
- How does the thrust coefficient vary with Reynolds number under unsteady freestream flow conditions?
- Is the optimal Strouhal number for thrust production within the typical range ($St = 0.2 - 0.3$) relatively insensitive to Reynolds number under unsteady flow environments?

In summary, the following will be presented on Turbulence Effects:

1. An investigation of the impact of Reynolds numbers and Strouhal numbers on the performance of 2D airfoils in highly unsteady freestream.
2. Development of new scaling laws between aerodynamic forces and flow dynamic parameters for oscillating wings in highly unsteady freestream.
3. Quantification of different flow features of 2D and 3D stationary wings in highly unsteady freestream and compare to experiments.

Chapter 3: Computational Methods

3.1 High-Order CFD Methods

This section will provide an overview of the computational methods used in the current study. The FR/CPR method is a high-order computational fluid dynamics method used in this study. Previous studies [20, 108–110] have shown that these methods are accurate and applicable to the types of problems in the current research.

3.1.1 Governing Equations

Unsteady compressible Navier-Stokes equations in the conservation form are considered in this study. They can be expressed in the physical domain (t, x, y, z) as follows:

$$\frac{\partial Q}{\partial t} + \frac{\partial F}{\partial x} + \frac{\partial G}{\partial y} + \frac{\partial H}{\partial z} = 0, \tag{3.1}$$

where $Q = (\rho, \rho u, \rho v, \rho w, E)^T$ are conservative variables, ρ is the density of fluid, u, v and w are the x-, y- and z-components of the velocity and E is the total energy given by $E = \frac{p}{\gamma-1} + \frac{1}{2}\rho(u^2 + v^2 + w^2)$ for a perfect gas in which p is the pressure and γ is the constant specific heat capacity ratio. The total energy formula closes the solution system. F, G and H are total flux vectors including the inviscid and viscous flux terms in the x-, y- and z-direction, respectively, which are expressed as

$$F = F^i - F^v = \begin{Bmatrix} \rho u \\ \rho u^2 + p - \tau_{xx} \\ \rho v u - \tau_{xy} \\ \rho w u - \tau_{xz} \\ u(E+p) - u\tau_{xx} - v\tau_{xy} - w\tau_{xz} - \frac{\mu C_p}{Pr} T_x \end{Bmatrix},$$

$$G = G^i - G^v = \begin{Bmatrix} \rho v \\ \rho u v - \tau_{yx} \\ \rho v^2 + p - \tau_{yy} \\ \rho w v - \tau_{yz} \\ v(E+p) - u\tau_{yx} - v\tau_{yy} - w\tau_{yz} - \frac{\mu C_p}{Pr} T_y \end{Bmatrix},$$

$$H = H^i - H^v = \begin{Bmatrix} \rho w \\ \rho u w - \tau_{zx} \\ \rho v w - \tau_{zy} \\ \rho w^2 + p - \tau_{zz} \\ w(E+p) - u\tau_{zx} - v\tau_{zy} - w\tau_{zz} - \frac{\mu C_p}{Pr} T_z \end{Bmatrix}.$$

where μ is the dynamic viscosity, C_p is the specific heat at constant pressure, Pr is the Prandtl number and T is the temperature. For the Newtonian fluids, the viscous stresses are given as follows:

$$\tau_{xx} = 2\mu(u_x - \tfrac{u_x+v_y+w_z}{3})$$

$$\tau_{yy} = 2\mu(v_y - \tfrac{u_x+v_y+w_z}{3})$$

$$\tau_{zz} = 2\mu(w_z - \tfrac{u_x+v_y+w_z}{3})$$

$$\tau_{xy} = \tau_{yx} = \mu(v_x + u_y)$$

$$\tau_{xz} = \tau_{zx} = \mu(w_x + u_z)$$

$$\tau_{yz} = \tau_{zy} = \mu(w_y + v_z)$$

To facilitate numerical simulation, the governing equation (3.1) in the physical domain (t, x, y, z) is transformed into computational domain (τ, ξ, η, ζ) as shown in Figure 3.1. Eq. (3.1) can be written as follows:

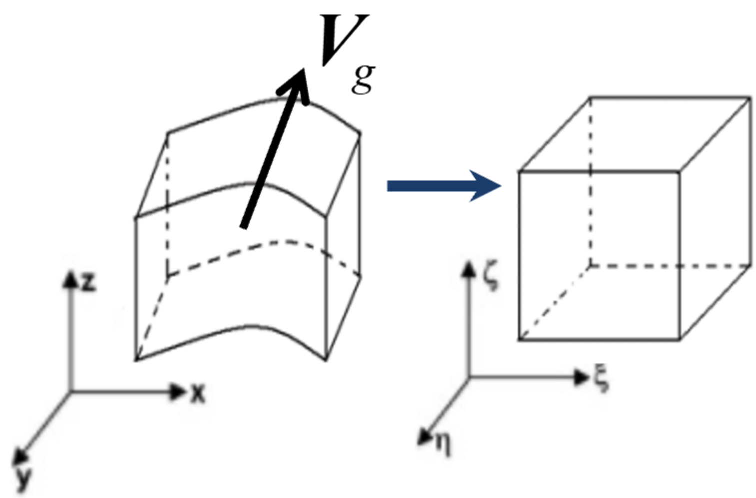

Figure 3.1: Coordinate transformation from a moving physical domain to a fixed computational domain.

$$\frac{\partial \tilde{Q}}{\partial \tau} + \frac{\partial \tilde{F}}{\partial \xi} + \frac{\partial \tilde{G}}{\partial \eta} + \frac{\partial \tilde{H}}{\partial \zeta} = 0, . \tag{3.2}$$

where

$$
\begin{cases}
\tilde{Q} = |J|Q \\
\tilde{F} = |J|(Q\xi_\tau + F\xi_x + G\xi_y + H\xi_z) \\
\tilde{G} = |J|(Q\eta_\tau + F\eta_x + G\eta_y + H\eta_z) \\
\tilde{H} = |J|(Q\zeta_\tau + F\zeta_x + G\zeta_y + H\zeta_z)
\end{cases}
. \tag{3.3}
$$

Note that in the coordinate transformation, $\tau = t$ and $(\xi, \eta, \zeta) \in [-1, 1] \times [-1, 1] \times [-1, 1]$ is a standard element in the computational domain. The Jacobian matrix of the coordinate transformation can be written as the following form:

$$
J = \frac{\partial(x, y, z, t)}{\partial(\xi, \eta, \zeta, \tau)} = \begin{pmatrix} x_\xi & x_\eta & x_\zeta & x_\tau \\ y_\xi & y_\eta & y_\zeta & y_\tau \\ z_\xi & z_\eta & z_\zeta & z_\tau \\ 0 & 0 & 0 & 1 \end{pmatrix}. \tag{3.4}
$$

The inverse transformation must also exist for a non-singular transformation. Therefore, the inverse of the Jacobian matrix can be written as:

$$
J^{-1} = \frac{\partial(\xi, \eta, \zeta, \tau)}{\partial(x, y, z, t)} = \begin{pmatrix} \xi_x & \xi_y & \xi_z & \xi_t \\ \eta_x & \eta_y & \eta_z & \eta_t \\ \zeta_x & \zeta_y & \zeta_z & \zeta_t \\ 0 & 0 & 0 & 1 \end{pmatrix}. \tag{3.5}
$$

The metrics ξ_t, η_t and ζ_t are related to the grid velocity vector $\vec{v}_{grid}$ as

$$
\begin{cases}
\xi_t = -\vec{v}_{grid} \cdot \nabla\xi, \\
\eta_t = -\vec{v}_{grid} \cdot \nabla\eta, \\
\zeta_t = -\vec{v}_{grid} \cdot \nabla\zeta,
\end{cases} \tag{3.6}
$$

The geometric conservation law (GCL) has been enforced following the error compensation approach [111].

3.1.2 Spatial Discretization and Time Integration Methods

The Flux Reconstruction/Correction Procedure via Reconstruction (FR/CPR) [20,21,108,110,112–114] method was used to solve the governing equations. A brief introduction of the FR/CPR method is discussed in this section for the sake of completeness, but a full discussion of the method can be found in [20]. In FR/CPR methods, the flux terms in Eq. (3.2) are divided into two parts, i.e. local fluxes $\tilde{F}^{loc}$ constructed from local solutions and correction fluxes $\tilde{F}^{cor}$ by mapping the differences between the local fluxes and the common fluxes on the element interfaces into the entire element with high-order correction functions. This can be expressed as:

$$\begin{cases} \tilde{F}(\xi,\eta,\zeta) = \tilde{F}^{loc}(\xi,\eta,\zeta) + \tilde{F}^{cor}(\xi,\eta,\zeta) \\ \tilde{G}(\xi,\eta,\zeta) = \tilde{G}^{loc}(\xi,\eta,\zeta) + \tilde{G}^{cor}(\xi,\eta,\zeta) \\ \tilde{H}(\xi,\eta,\zeta) = \tilde{H}^{loc}(\xi,\eta,\zeta) + \tilde{H}^{cor}(\xi,\eta,\zeta) \end{cases}. \tag{3.7}$$

On substituting Eq. (3.7) into Eq. (3.2), the governing equations in the computational domain can be reformulated as:

$$\frac{\partial \tilde{Q}}{\partial \tau} + \left(\frac{\partial \tilde{F}^{loc}}{\partial \xi} + \frac{\partial \tilde{G}^{loc}}{\partial \eta} + \frac{\partial \tilde{H}^{loc}}{\partial \zeta}\right) + \left(\frac{\partial \tilde{F}^{cor}}{\partial \xi} + \frac{\partial \tilde{G}^{cor}}{\partial \eta} + \frac{\partial \tilde{H}^{cor}}{\partial \zeta}\right) = 0. \tag{3.8}$$

In this study, the inviscid common fluxes on the element interfaces were calculated using the Roe approximate Riemann solver [115] and the common viscous fluxes were obtained by the second approach (BR2) developed by Bassi and Rebay [116]. To minimize numerical errors when performing simulations on curved elements [117], Eq. (3.8) can be transformed back to the physical domain as

$$\frac{\partial Q}{\partial \tau} + \left(\frac{\partial F^{loc}}{\partial \xi} + \frac{\partial G^{loc}}{\partial \eta} + \frac{\partial H^{loc}}{\partial \zeta} \right) + \delta^{cor} - \vec{v}_{grid} \cdot \nabla Q = 0. \tag{3.9}$$

To solve Eq. 3.9, it can be rewritten as

$$\frac{\partial Q}{\partial \tau} = R(Q, \nabla Q), \tag{3.10}$$

and the linearly implicit Rosenbrock-Wanner (ROW) Runge-Kutta method [108] was used for time integration. The general formulation of ROW is written as

$$\begin{cases} Q^{n+1} = Q^n + \sum_{j=1}^{K} m_j Y_j, \\ (\frac{I}{\gamma \Delta t} - \frac{\partial R}{\partial Q})^n Y_i = R(Q^n + \sum_{j=1}^{i-1} a_{ij} Y_j) \\ \quad + \frac{1}{\Delta t} \sum_{j=1}^{i-1} c_{ij} Y_j, \quad i = 2, \dots K \end{cases} . \tag{3.11}$$

Herein, K is the number of stages, Δt is the time step, and m_j, γ, a_{ij} and c_{ij} are the coefficients of the ROW scheme. In chapter 4 and 5 for the moving grids, a third-order accurate spatial discretization and a third-order, four-stage ROW scheme with the time step of 1×10^{-4} were used in all simulations.

In chapter 6, for the stationary 3D simulations, explicit first stage, singly diagonally implicit Runge-Kutta (ESDIRK) method [108,114] was used in the simulations in order to save computational costs. The general formulation of ESDIRK is written as

$$\begin{cases} Q^{n+1} = Q^n + \Delta t \sum_{i=1}^{s} b_i R(Q_i), \\ Q_i = Q^n + \Delta t \sum_{j=1}^{i} a_{ij} R(Q_j), \quad i = 1, \dots s, \end{cases} . \tag{3.12}$$

where s is the number of stages and

$$a_{ii} = \begin{cases} 0, & i = 1 \\ \omega, & i \neq 1 \end{cases} . \tag{3.13}$$

Equation (3.12) can then be written as

$$\begin{cases} Q^{n+1} = Q^n + \Delta t \sum_{i=1}^{s} b_i R(Q_i), \\ Q_1 = Q^n, \\ Q_i = \Delta t \omega R(Q_i) + Q^n + \Delta t \sum_{j=1}^{i-1} a_{ij} R(Q_j), \quad i = 2, \dots s, \end{cases} \tag{3.14}$$

In this study for the 3D simulations, the second-order, three-stage ESDIRK2 and forth-order, sixth-stage ESDIRK4 with the time step of 10^{-2} were used.

3.1.3 Dynamic Grids Deformation

Dynamically deforming grids are needed to accurately model the oscillating wing problems in this study. Herein, the algebraic grid deformation algorithm based on the earlier work [111, 118] was used to reconstruct the whole physical domain. A fifth-order blending function with $r(0) = 0$ and $r(1) = 1$ was used for dynamic mesh deformation. It is written as

$$r_5\ (s) = 10s^3 - 15s^4 + 6s^5, \quad s\ \in [0, 1] \tag{3.15}$$

where s represents the normalized distance between the present grid node and the moving boundaries. The change in the position vector $\vec{P}$ for an arbitrary grid node can then be obtained as follows:

$$\Delta \vec{P}_{present} = (1 - r_5) \Delta \vec{P}_{rigid} \tag{3.16}$$

When $r_5\,(0) = 0$, the grid node will move at the same speed with the moving boundary; and when $r_5\,(1) = 1$, the grid node will stay stationary.

3.2 Verification and Validation (V&V) of CFD Solver

As a first step, verification and validation (V&V) of the flow solver was conducted under uniform flow conditions, without the gust or array of circular cylinders present. The surface forces acting on the fluid particle are due to pressure and viscous stress. The forces (drag and lift) were calculated by integrating the pressure and viscous forces acting on the surface. The net pressure and viscous stress forces acting on the fluid can be expressed as

$$\vec{F} = \vec{F}_p + \vec{F}_v$$

$$\vec{F}_p = -\oint_S p\hat{n}\, dS$$

$$\vec{F}_v = \oint_S \hat{n} \cdot \bar{\bar{\tau}}\, dS$$

where $\bar{\bar{\tau}}$ is the viscous stress tensor. Notably, pressure acts normal to the surface, whereas viscous stress has components that act both normal and tangent to the surface in general.

Numerical results were compared with published data from previous experiments and computations. Table 3.1 shows a comparison of drag coefficient (C_D) at Reynolds number (Re) = 12,000 at zero AoA under uniform flow conditions. The current drag coefficient agrees well with the reference data [88, 119–121].

For V&V of the flow solver when using moving grids, a common set of airfoil kinematics was implemented on the solver. In this study a NACA0012 airfoil was pitched about its 1/4 chord with a sinusoidal motion, specifically expressed as:

$$\theta(t) = \theta_m + \theta_o \sin(2\pi f t + \phi), \tag{3.17}$$

Table 3.1: Comparison of C_D for NACA0012 at $Re = 12,000$ and $AoA = 0°$ in a uniform flow.

Source	C_D
Current	0.0347
Hammer *et al.* [119]	0.0350
Laitone [88]	0.0334
Liu and Kawachi [120]	0.0346
Young and Lai [121]	0.0361

where θ_m is the mean angle of attack, θ_o is the amplitude of the pitching angle, ϕ is the initial phase, f is the oscillating frequency, and t is the dimensional time. These types of problems are typically classified by using reduced frequency, k, and Strouhal number, S_t, which are defined as

$$k = \frac{\pi f c}{U_\infty}, \tag{3.18}$$

$$S_t = \frac{2 f A_{pitch}}{U_\infty}, \tag{3.19}$$

where c is the chord length of the airfoil, A_{pitch} is the pitching amplitude of the trailing edge of the airfoil, and U_∞ is the freestream velocity. The airfoil was oscillated at a variety of reduced frequencies for comparison with other work [122]. Figure 3.2 shows a comparison of average thrust coefficients for the pitching airfoil simulation with a pitching amplitude of 2° and 4° at Reynolds number 12,000. The results agree well with the results in the prior study [122] for identical flow conditions.

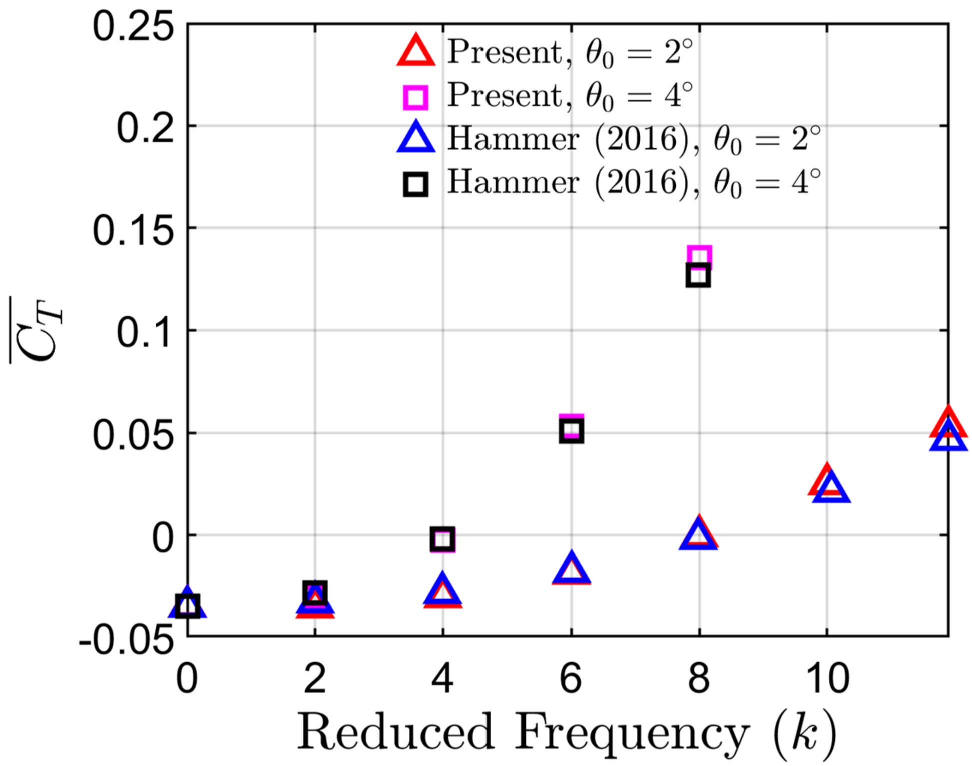

Figure 3.2: Time-averaged thrust coefficients over a NACA0012 airfoil pitching about its quarter chord length at Re = 12,000 compared with the results from Hammer [122].

In the recent studies [25, 34], a comparison of gust-wing interaction between experimental results from a vertical gust generator in a wind tunnel and numerical ones with the high-order CFD tool, also used in this study, has been carried out. Reasonable agreement with experimental flow fields around a stationary airfoil interacting with a gust was achieved in those studies.

Furthermore, a range of Strouhal numbers were compared with results from Sentruk and Smits [123], shown in Fig. 3.3, which numerically analyzed thrust production of oscillating airfoils. Figure 3.3 shows that the average thrust coefficient for different Reynolds numbers over a range of Strouhal numbers. The results of the current study agreed well with the Sentruk & Smits results, which showed that increasing Reynolds number acts to increase mean thrust generation at a fixed Strouhal number.

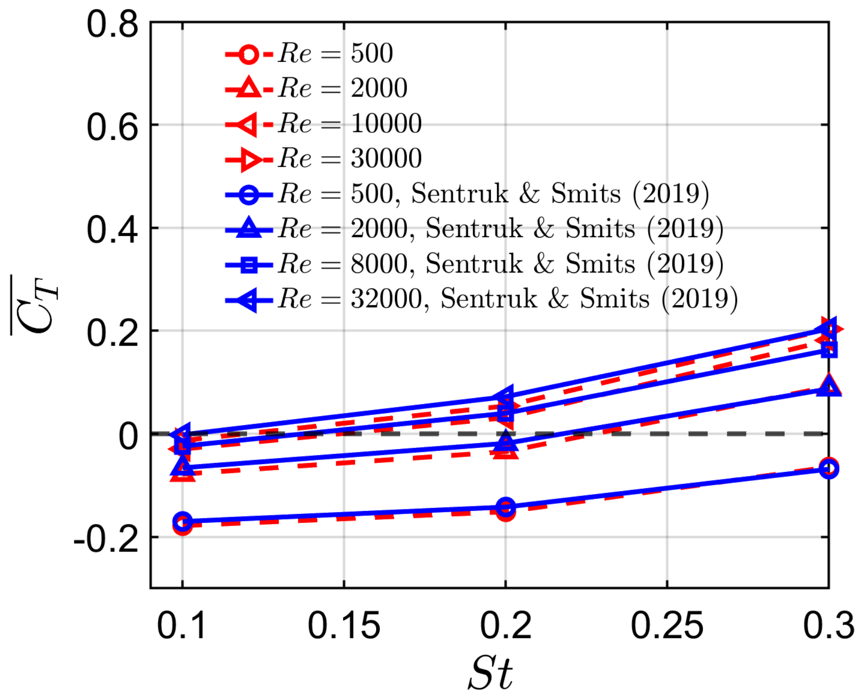

Figure 3.3: Time-avereaged thrust coefficients over airfoil under uniform flow condition at different st for different Reynolds numbers and comparison with Sentruk & Smits [123] .

Chapter 4: Gust-Wing Interaction over an Airfoil at Low Reynolds Numbers

This chapter presents the impact of vertical gusts on stationary and oscillating NACA0012 (National Advisory Committee for Aeronautics) airfoils at low Reynolds numbers using high-order computational fluid dynamics (CFD) methods, and identifies key dynamics that dominate gust mitigation. The gust is created by a cross-flow interaction of a ducted floor jet and a freestream flow, which causes the jet to bend downstream creating a blockage effect and modifying the effective angle of attack (AoA) over an airfoil in the freestream flow. These findings give the reader a better understanding of the underlying flow physics of gust wing interactions for stationary wings, as well as gust mitigation strategies, which answer the thesis's first objective in Chapter 2.

4.1 Computational Setup

The computational domain shown in Fig. 4.1 was used in the current study. The distance between the quarter chord location of the NACA 0012 airfoil to the center of the gust is $1.08c$, where c is the chord length of the airfoil. The gust width at the exit in this study is $1.06c$. Note that the dimensions of the computational domain are calculated to match those from a wind tunnel experiment [25].

For this simulation a far field boundary was used for the top of the computational domain, which is different from the top wall of the wind tunnel. Results in previous studies [34] showed that this has a limited effect when compared to the wind tunnel tests. Fixed inlet and outlet boundaries, and an inviscid wall boundary on the bottom of the computational domain were enforced in the simulation. As observed in Fig. 4.1, a uniform incoming flow in the horizontal direction interacted with a jet of a uniform vertical velocity generated ahead of and below the airfoil. Since non-dimensionalized Navier-Stokes equations were solved, the incoming flow velocity U_∞ was set as 1, and correspondingly, the Mach number was 0.1. The chord length of the airfoil was selected to generate a chord Reynolds number of Re = 12,000. The transient gust was generated by a cross-flow ducted floor jet and its interaction with the freestream flow caused the jet to bend downstream, thus creating a blockage effect and modifying the effective AoA over the airfoil in the freestream flow. For the gust inlet, a uniform vertical gust velocity of similar magnitude as the experimental setup [25] was given. The gust ratio (GR) is defined as the vertical speed V of gust divided by the freestream flow U_∞ (i.e. V/U_∞) which was 0.42 for all simulations presented in this paper.

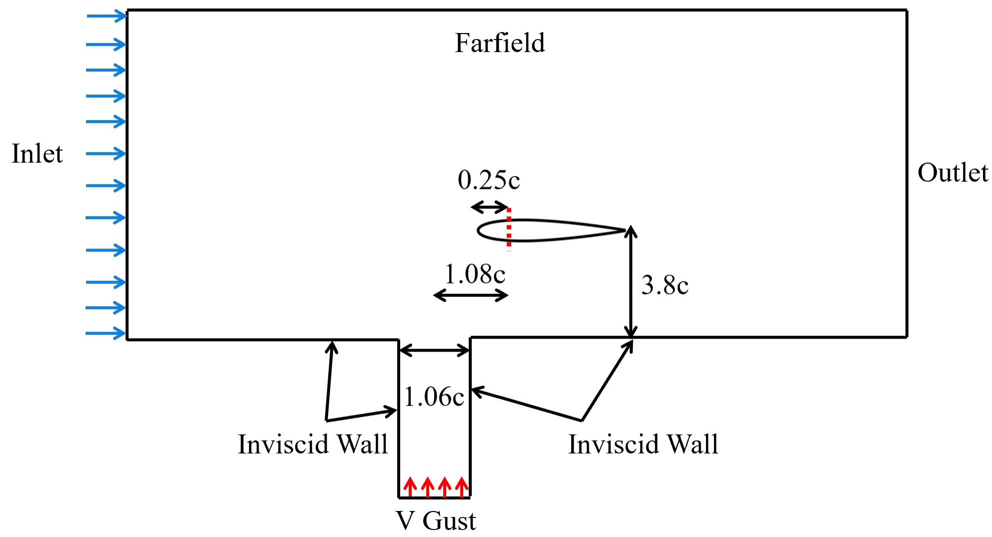

Figure 4.1: An illustration of the computational domain.

4.2 Results and Discussion

4.2.1 Gust-Wing Interaction over a Stationary Airfoil

To explore the effect of a vertical gust on the stationary airfoil, a simulation was first conducted with the airfoil placed at zero AoA (i.e. $\alpha = 0°$) at a Reynolds number of Re = 12,000. To understand the effects of the gust the forces acting on the airfoil were decomposed into horizontal (drag or thrust) and vertical (lift) directions with respect to the position of airfoil. The drag and lift coefficients are defined as

$$C_D = \frac{2F_X}{\rho {U_\infty}^2 A}, \tag{4.1}$$

$$C_L = \frac{2F_Y}{\rho {U_\infty}^2 A}, \tag{4.2}$$

where F_X is the drag force, F_Y is the lift force, ρ is the fluid density, U_∞ is the freestream velocity and A is the area. Note that when C_D is negative, it indicates that a thrust is generated. For 2D problems, the force is measured per unit length; therefore, A is replaced with the chord length of the airfoil.

Figure 4.2 shows the lift and drag coefficient histories of the stationary NACA0012 airfoil with the gust developing in the vertical direction. Figure 4.2 clearly depicts the effect of the gust on lift and drag over time due to the continuous change of the effective AoA. Before $t^* = 20$, the gust was in an early development stage, and the airfoil experienced a sudden pressure wave propagation from the gust, resulting in several spikes in the lift coefficient history, such as a spike around the non-dimensionalized time $t^* = tU_\infty/c = 6$. After $t^* = 20$ the gust starts to interact with the airfoil more significantly. The results suggest that vertical gusts can cause a highly unsteady stall event on the airfoil. After around $t^* = 50$ the lift on the airfoil experienced fluctuations on the order of the peak steady lift. A lower gust ratio (GR = 0.21) was tested and showed similar results to the higher gust ratio case. For this lower gust ratio the lift evolved more slowly and transitioned to unsteadiness later than the higher gust ratio shown in Fig. 4.2, but the same trend was observed.

Instantaneous vorticity fields around the airfoil at different times during the gust interaction are shown in Fig. 4.3. At early time ($t^* = 10$) the effect of the gust was minimal but after $t^* = 24$, the effects became more easily observed. At this time the trailing edge separation became more pronounced with a notable vortex roll up. When the gust continued to develop a separation bubble on the suction side near the trailing edge grew, with some shear layer roll up approaching the leading edge.

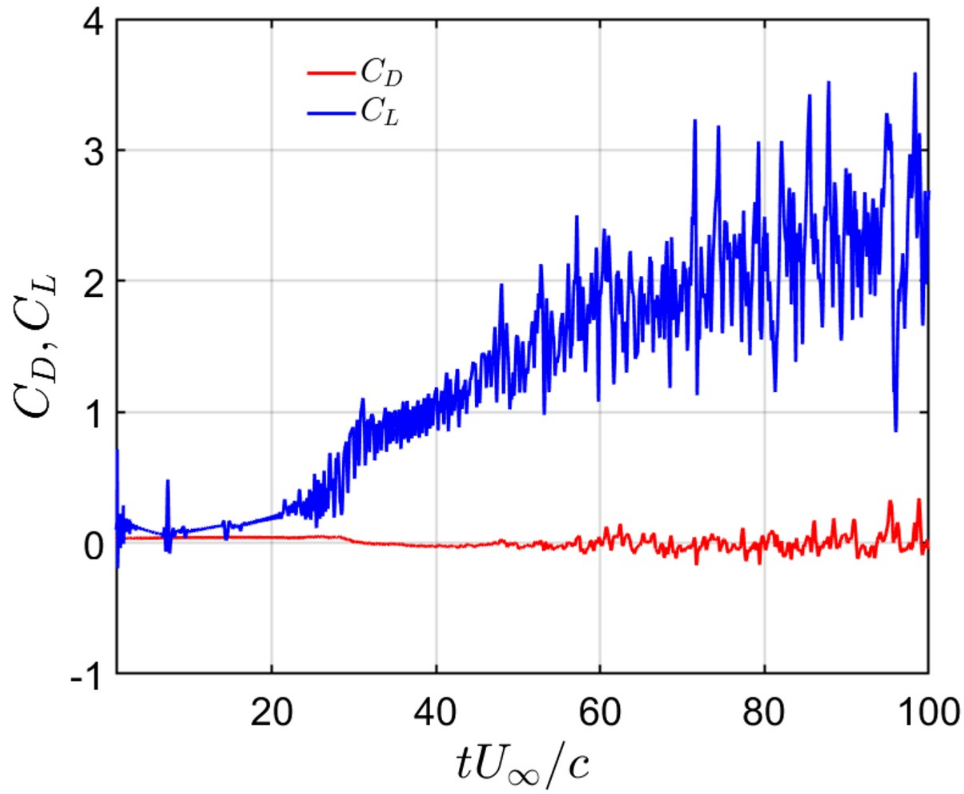

Figure 4.2: Histories of drag and lift coefficients for NACA0012 at Re = 12,000 and AoA = 0° with gust developing in the vertical direction.

After $t^* = 31$, these vortices formed on the upper surface and detached from the airfoil, forming vortex shedding as shown in Fig. 4.3(c) and (d). This effect occurred around the bend in lift observed around $t^* = 30$ in Fig. 4.2 and suggests the wing had entered a stalled state around this time. These shed vortices eventually formed near the leading edge and generated a transient low-pressure region on the upper surface of the airfoil, enhancing the lift. Once the gust was sufficiently developed, the airfoil experienced a highly unsteady leading edge vortex roll-up, somewhat similar to a dynamic stall event as shown in Fig. 4.3(e) and (f). It should be noted at this point the flow angle had changed significantly that much of the lift generated was caused by the pressure side of the airfoil, with unsteady events dominating the stalled state.

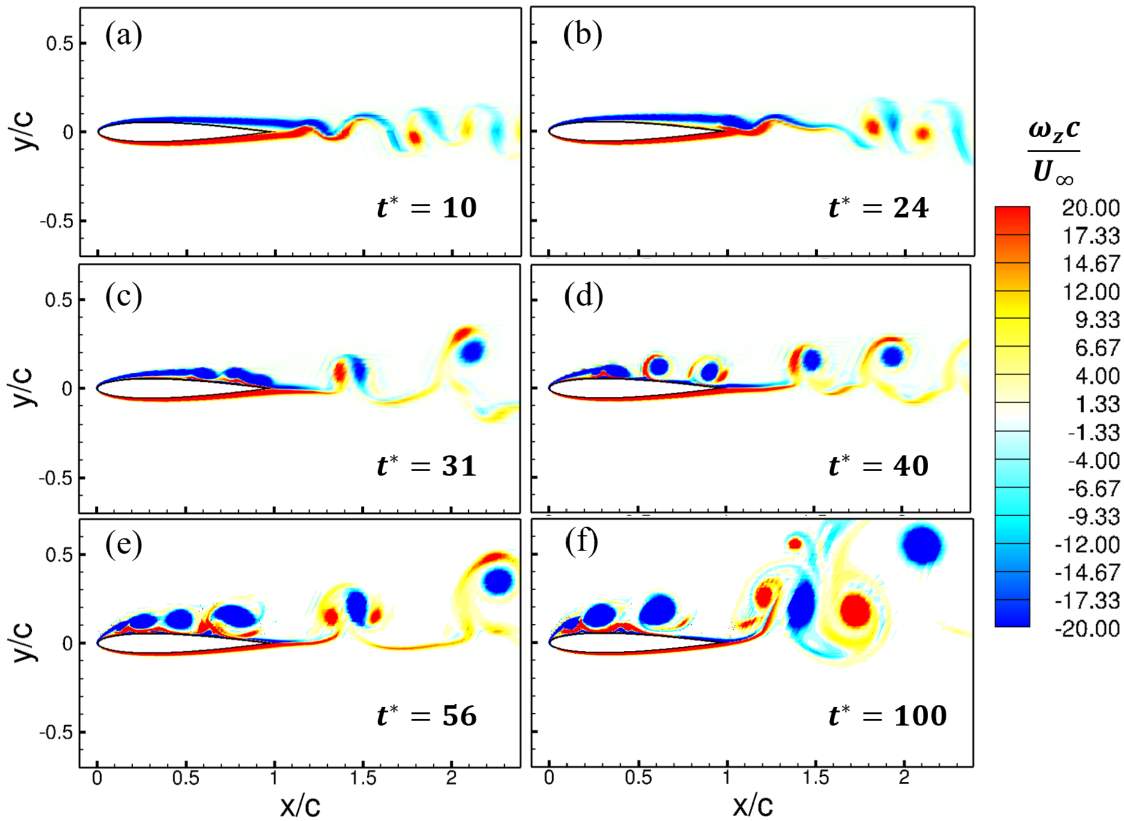

Figure 4.3: Instantaneous vorticity fields around the airfoil at (a) $t^* = 10$, (b) $t^* = 24$, (c) $t^* = 31$, (d) $t^* = 40$, (e) $t^* = 56$ and (f) $t^* = 100$ at $Re = 12,000$ during the gust development process.

4.2.2 Gust-Wing Interaction with a Pitch-Down Maneuver

The gust-stationary wing section showed a wing undergoing a highly unsteady stall event due to the change in the effective AoA caused by the gust. Recent studies on gust mitigation [103, 105, 124] suggest that the gust effects can be controlled by changing the effective AoA induced by the gust. In this study this control strategy was tested for a gust that developed over a longer time with a steady peak gust magnitude. The airfoil was pitched about the $c/4$ of the airfoil with a variety of response motions. These motions had a pre-set pitch down magnitude to mimic a controller with a pre-programmed gust response motion.The airfoil was pitched down to four different mean AoAs, namely, $\alpha_m = -12°$, $-18°$, $-22.8°$ and $-30°$, to change the effective AoAs induced by the gust after the non-dimensional time $t^* = 40$. These motions are shown in Eq. (4.3) and are based on pitching motions defined in Eldredge *et al.* [125] and Garmann *et al.* [126]. Note that this geometric AoA variation approach was used to avoid discontinuities in the pitching rate.

$$\alpha(t) = \frac{\alpha_m}{2a\Delta T} ln\Big(\frac{cosh(a(T-T_1))}{cosh(a(T-T_2))}\Big) + \frac{1}{2}\alpha_m, \tag{4.3}$$

where a is the smoothness shape function parameter which was 2.6 in the simulations, α_m is the maximum pitch down angle which was set to ramp from $\alpha_m = 0$ to $tan^{-1}(V/U_\infty)$, T is the non-dimensional time ($T = tU_\infty/c$), and $\Delta T = T_2 - T_1$, where T_1 and T_2 are the non-dimensional time at which the motion to pitch down maneuver would start and stop, respectively. The reduced pitch rate $K = \alpha_m c/\left(2U_\infty \Delta t\right)$ was varied to induce continuously changing AoAs. Note that an increase in a and decrease in ΔT can cause more abrupt motion.

The motion profiles of the AoA change are illustrated in Fig. 4.4(a). Figure 4.4(b) shows the corresponding lift coefficient histories for different pitch-down maneuver cases interacting with the growing vertical gust. When the pitch angle of the airfoil was larger than the effective AoA induced by the developing gust, the airfoil undergoes a negative lift overshoot with a large separation event on the lower surface of the airfoil; see Fig. 4.5. This overshoot stall was observed on all test cases except for the smallest motion. However, because the gust continued to grow during this time the lift coefficient rose to positive values over time. When the effective AoA of the gust grew after the pitch-down motion, the lift again started to fluctuate and the wing reentered a stall state, see Fig. 4.4(b).

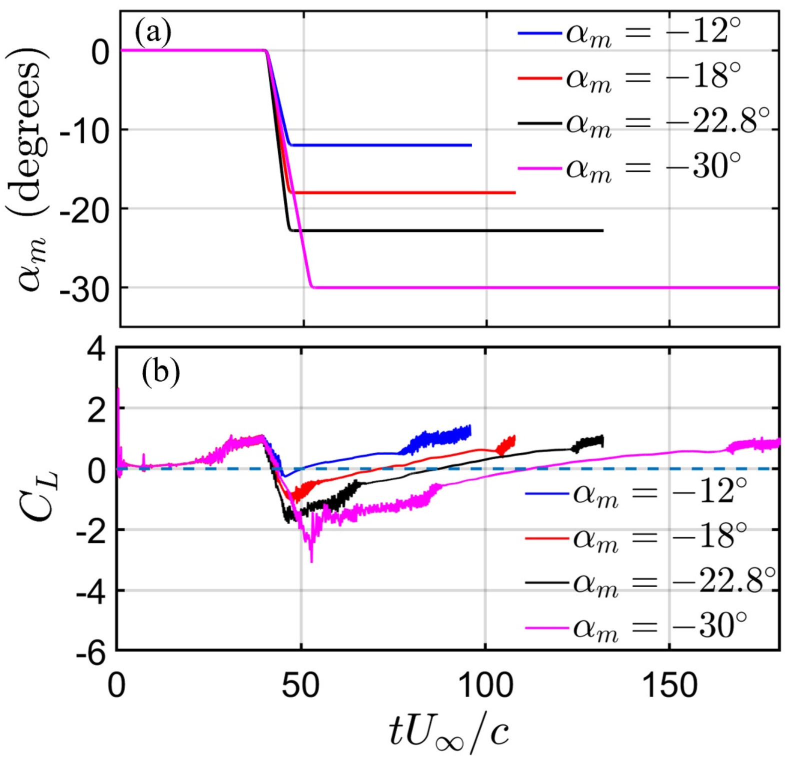

Figure 4.4: (a) Pitch-down motion for different AoAs; and (b) Lift coefficients histories for the pitch-down airfoil at different effective AoAs.

To avoid this overshoot stall while continuing to mitigate the gust effect, a step-wise pitch motion was tested. Figure 4.4(b) showed that the airfoil entered an unsteady stall state after non-dimensional time $t^* = 76$, following a pitch down of $\alpha_m = -12°$. Continuing this step-wise pitch-down behavior, the airfoil was further pitched down $\alpha_m = -6°$, resulting in a geometric AoA of $\alpha_m = -18°$ and attached

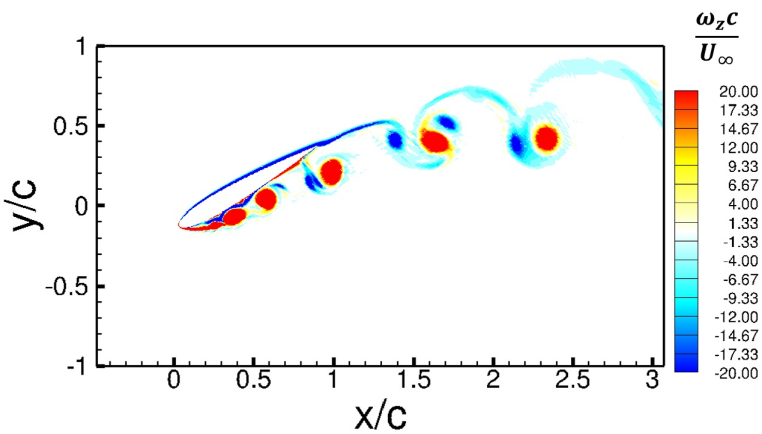

Figure 4.5: Instantaneous vorticity field for the pitch-down airfoil with $\alpha_m = -30°$ at $t^* = 60$.

flow on the airfoil. As the gust induced AoA continued growing, with a similar effect on lift, the lift again to fluctuate around $t^* = 110$. At this point the airfoil was again pitched down by $\alpha_m = -6°$. This process was repeated until the geometric AoA of $\alpha_m = -30°$ was reached; see Fig. 4.6. Eventually, even at this significant downward pitch angle, the growing AoA caused by the gust exceeded the stall angle of the airfoil and unsteady lift was again observed. When a step-wise pitch-down motion was used, the lift overshooting phenomenon was suppressed and the lift fluctuation associated with traditional stall was also effectively suppressed. While a step-wise motion is somewhat atypical of aircraft motions, a stall sensor with a pre-programmed pitch-down response is more likely to be implemented on MAV systems than a continuous closed-loop controller for gusts.

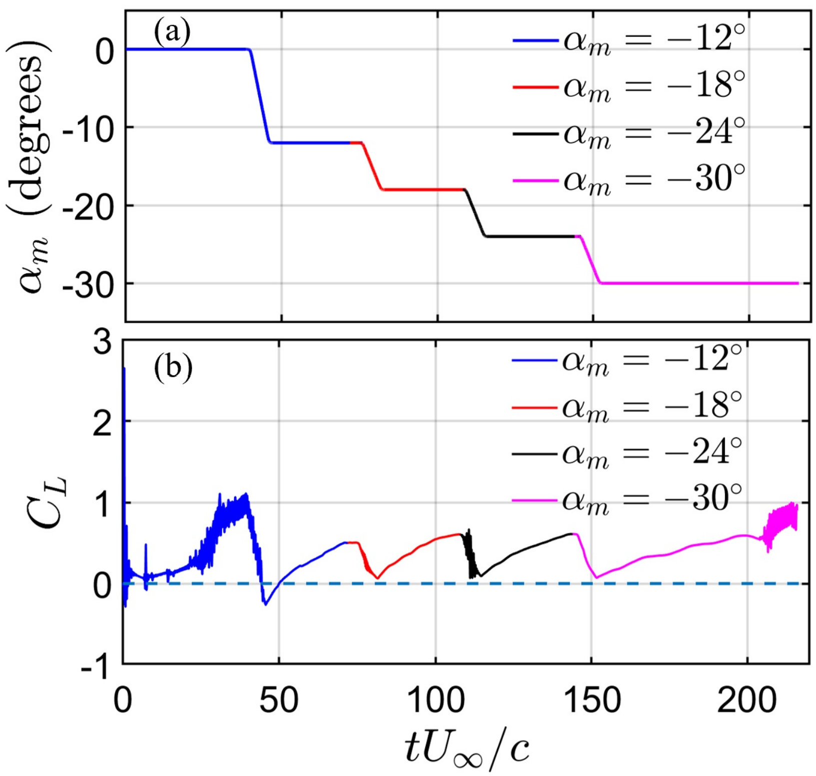

Figure 4.6: (a) Step-wise pitch-down motion from $\alpha_m = 0^\circ$ to $\alpha_m = -12^\circ$, $\alpha_m = -18^\circ$, $\alpha_m = -24^\circ$ and $\alpha_m = -30^\circ$, and (b) Lift coefficients histories for the pitch-down airfoil with the step-wise pitch-down motion from $\alpha_m = 0^\circ$ to $\alpha_m = -30^\circ$.

4.2.3 Gust-Wing Interaction over a Pitching Airfoil

4.2.3.1 Effect of Reduced Frequency

This section presents a novel method of vertical gust mitigation, which uses small amplitude airfoil oscillations to alter the flow and negate the effects of the gust. The effects of reduced frequency and Strouhal number are evaluated to determine the driving forces behind the interaction. A wide range of reduced frequencies were tested as documented in Table 4.1. Note that the pitching amplitude for all these cases was fixed at $\theta_o = 10°$, which will result in different Strouhal numbers. The Reynolds number and the gust ratio (V/U_∞) remained at 12,000 and 0.42, respectively, to match the stationary wing case. The airfoil pitch frequencies considered in Table 4.1 were determined based on local peak frequencies observed in the power spectral density (PSD) of the lift data recorded during interaction between the vertical gust and the stationary airfoil, as shown in Fig. 4.7(a). Figure 4.7(b) shows the PSD of the streamwise velocity recorded in the wake region at two locations (x/c,y/c) = (2,0) and (2, 0.2). Based on the PSD analysis of the velocity in the wake region, the vortex shedding frequency was observed around 0.91 Hz, which results in a reduced frequency of 2.86. This frequency appears as a local peak in both Fig. 4.7(a) and Fig. 4.7(b), and was selected as one of the oscillating frequencies for testing.

To simplify the analysis of the gust-wing interaction with the oscillating airfoil, the gust interaction was broken up into "early" and "later" stages. The early stage

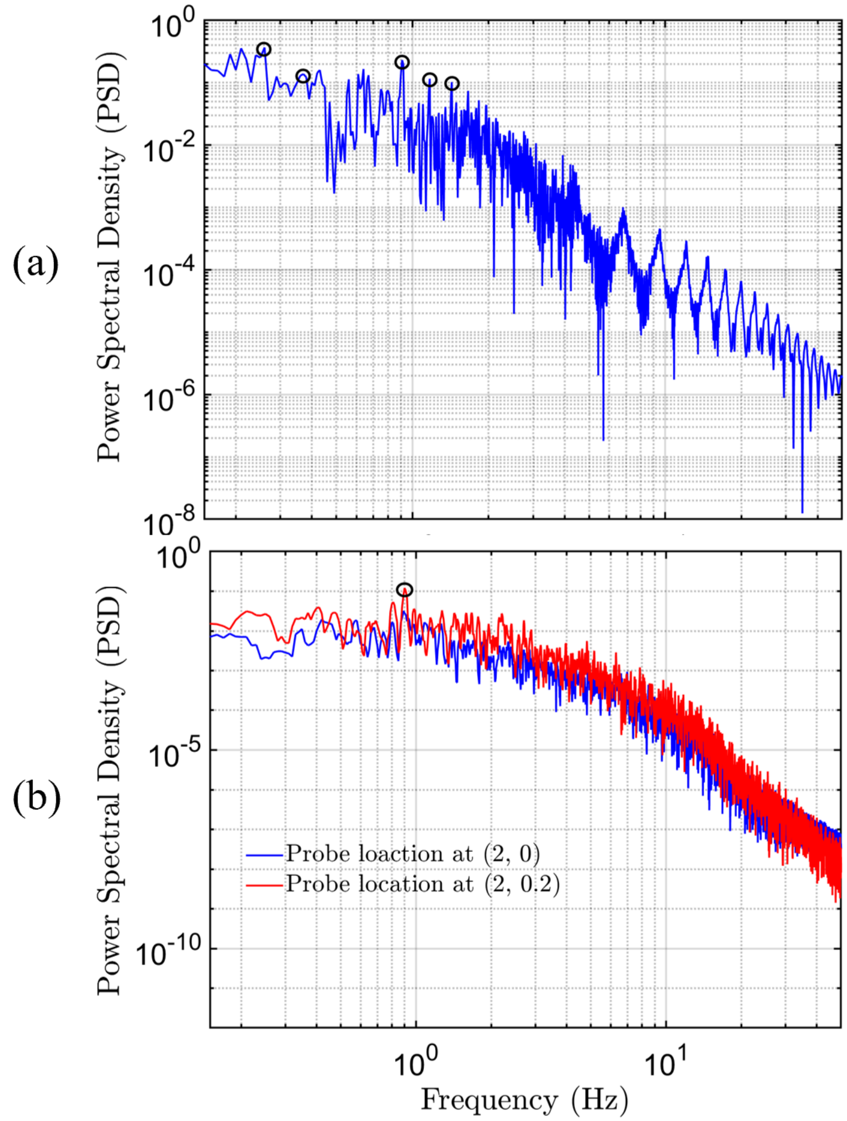

Figure 4.7: PSD of (a) the lift coefficient and (b) the streamwise velocity probed at (x/c, y/c) = (2, 0) and (2, 0.2) in the wake region for NACA0012 at Re = 12,000 and AoA = $0°$ with gust.

Table 4.1: Pitching airfoil cases with varying reduced frequencies with a fixed pitching amplitude $\theta_o = 10°$.

Cases	Reduced Frequencies	Strouhal Numbers
1	0.79	0.065
2	1.16	0.096
3	2.86	0.237
4	3.64	0.302
5	4.46	0.370

is defined as $t^* \leq 20$ and the later stage was $t^* \in [30, 40]$. Force coefficients presented for early and later stages were averaged over these time frames. Figures 4.8 and 4.9 show the drag and lift coefficient histories of the pitching airfoil at the different reduced frequencies tested. The drag and lift coefficient histories of the stationary airfoil are also presented in the two figures for comparison purposes. At lower reduced frequencies, such as $k = 0.79$, the force histories have high-frequency fluctuations similar to the stationary airfoil. When the reduced frequency reached $k = 2.86$, the force histories became periodic and were dominated by the pitching frequency of the airfoil. In this case, the gust had a limited effect on the mean lift during the early stage. Later as the gust grows in magnitude, the mean lift rose accordingly in the same fashion as that of the stationary airfoil; however, the force was still periodic with very small fluctuations. Similar phenomena were observed for the cases with higher reduced frequencies (not presented here). Higher reduced frequency cases appeared to completely mitigate the unsteadiness caused by the gust.

Figure 4.10 shows the time averages of the aerodynamic force coefficients of the airfoil for the stationary airfoil and the oscillating airfoils at different reduced frequencies during the early gust development stage (i.e. $t^* \leq 20$) and a later gust-wing interaction stage (i.e. $t^* \in [20, 40]$). The average for the early gust-wing interaction stage is carried out from $t^* = 10$ to 20, during which the gust had limited influence on the airfoil. At the later stage the average was calculated from $t^* = 30$ to 40. Note that for pitching airfoil cases, the average was calculated with the maximum number of pitching cycles that can be fit into the 10 non-dimensional time period to eliminate any pitching-cycle-related bias. Figure 4.10(a) shows that drag was gradually converted to thrust as the reduced frequency increased, which was expected for an oscillating airfoil. At the later stage the interaction between the gust and the airfoil further increased this thrust production. At the early gust-wing interaction stage, the gust slightly increased the average lift coefficients ($\overline{C_L}$) when compared to the static airfoil. $\overline{C_L}$ for the cases with higher reduced frequencies was significantly increased due to the intense gust-wing interaction at the later stage. The case with $k = 2.86$ produced the maximum $\overline{C_L}$, see Fig. 4.10(b).

Two statistics were used to quantitatively evaluate the effectiveness of gust mitigation: power consumption and the smoothness of the lift coefficient history. An effective pitching strategy would exhibit a desired level of smoothness, which reflects lift predictability, with minimum power consumption. The power $P(t)$ required to

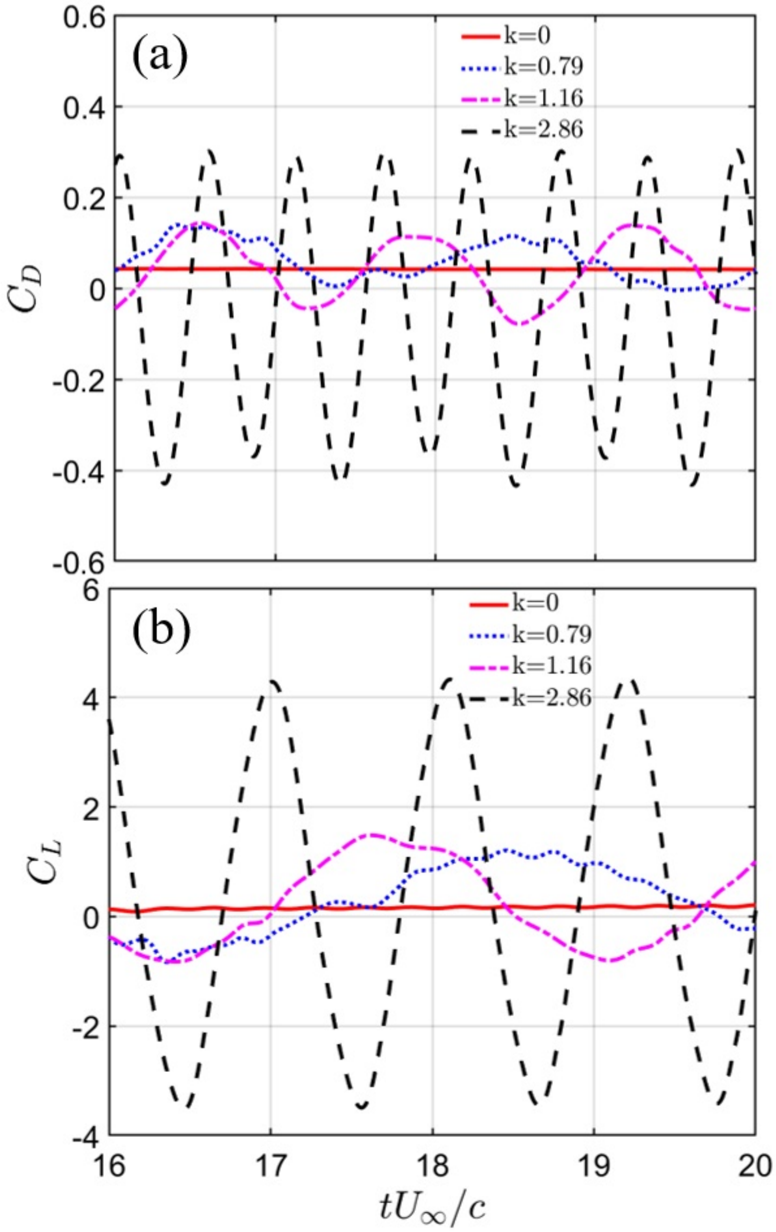

Figure 4.8: (a) Drag and (b) lift coefficient histories for the pitching airfoil at different reduced frequencies, compared with those for the stationary airfoil during the early stage of gust development.

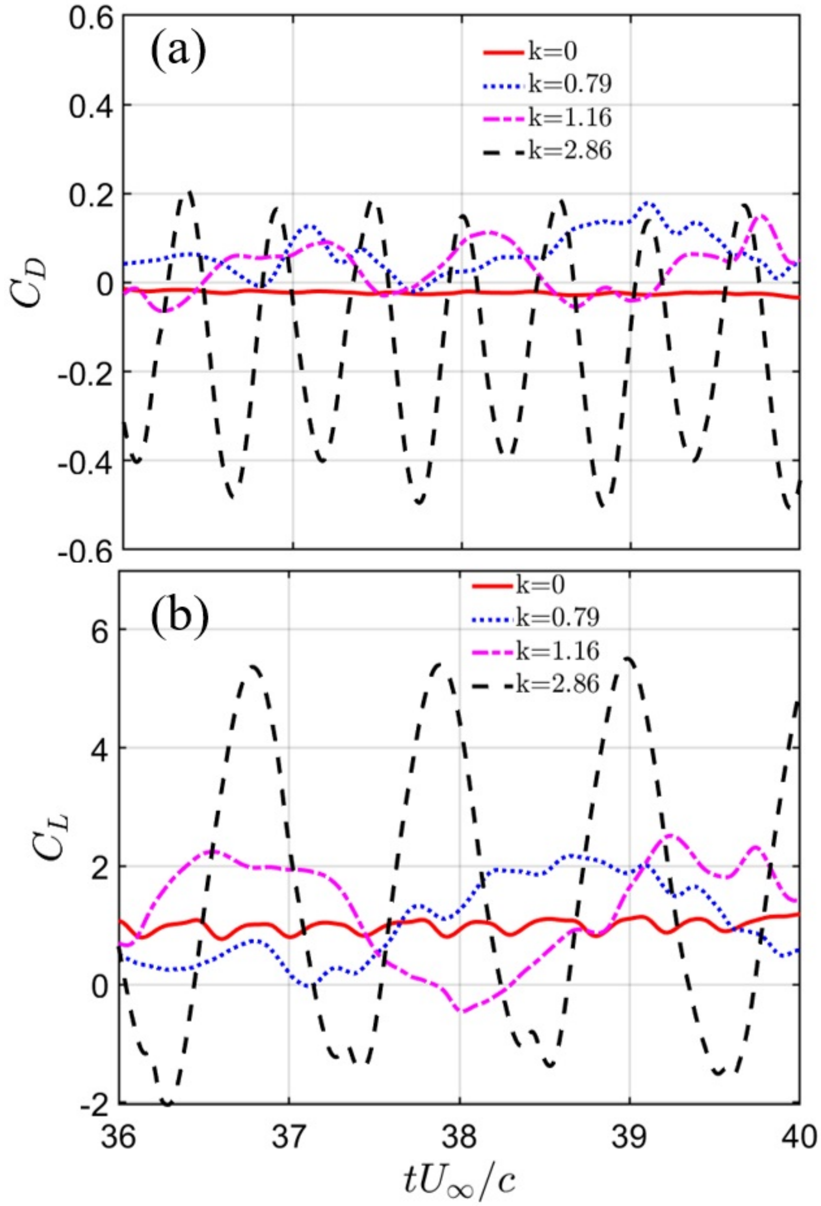

Figure 4.9: (a) Drag and (b) lift coefficient histories for the pitching airfoil at different reduced frequencies, compared with those for the stationary airfoil during the later stage of gust development.

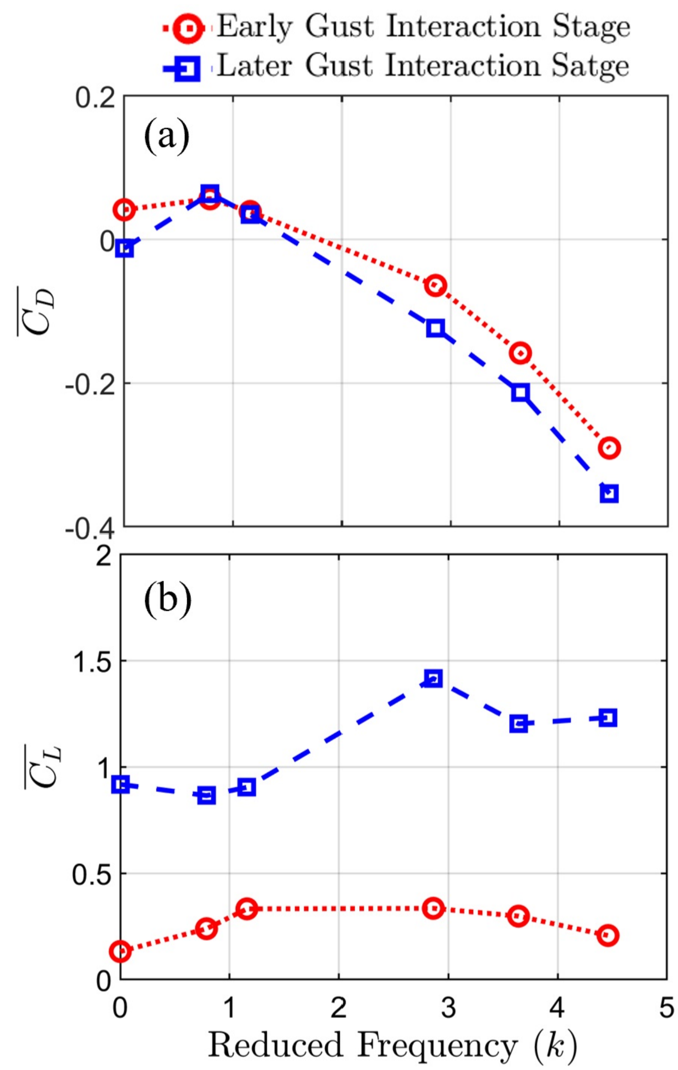

Figure 4.10: Time averaged aerodynamics forces before and after intensive gust-wing interaction. (a) Drag coefficient and (b) lift coefficient for the stationary and pitching airfoils at different reduced frequencies.

pitch the airfoil is calculated with the following formula

$$P(t) = -M(t)\frac{d\theta}{dt}, \tag{4.4}$$

where $M(t)$ is the pitching moment about the quarter chord length of the airfoil and $d\theta/dt$ is the angular velocity. Note that $M(t)$ can be estimated from the aerodynamic pitching moment as long as the inertia of the airfoil is very small. The dimensionless power coefficient is expressed as

$$C_p = \frac{P(t)}{0.5\rho c {U_\infty}^3} = -C_M(t)\frac{d\theta}{dt^*}, \tag{4.5}$$

where C_p and C_M are the power and moment coefficients, respectively. Figure 4.11 shows the average power coefficients of pitching airfoil at different reduced frequencies for early and late gust interaction. As expected the power coefficient of the oscillating airfoil increased with increasing reduced frequency. Interestingly the interaction with the gust lowered the power coefficient with a maximum benefit at $k = 2.86$, the same location where mean lift peaked.

The smoothness of the lift coefficient history was measured with a new parameter named "relative fluctuation". It is defined as the ratio between the L_2 norm (i.e., the square root of the "energy") of the fluctuation of any curve and that of the curve itself. The fluctuation was obtained by subtracting the smoothed curve after filtering from the original curve. In this test, a Guassian filter with a filtering window size of 1/6 pitching cycle was used to generate the smoothed curve. Two examples at $k = 0.79$ and 4.46 are used to explain this idea. As shown in Fig. 4.12, there are many small-scale fluctuations in the lift coefficient history when $k = 0.79$ and these fluctuations have been smoothed out after filtering. Since this case had

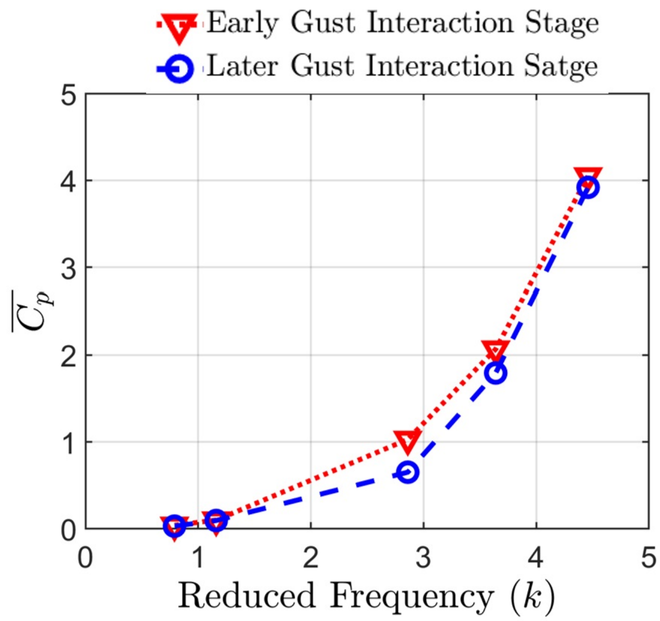

Figure 4.11: Time-averaged power coefficients of pitching airfoils at different reduced frequencies.

significant deviations from the smoothed curve, a large relative fluctuation of 0.0836 was observed (see Table 4.2). When $k = 4.46$, only the peak values are smoothed out which generated a small relative fluctuation about 0.0212. By calculating the relative fluctuations of sinusoidal curves with angular frequencies ranging from 1 to 100 (note that the angular frequency of the $k = 0.79$ case is 1.58 rad/s in this study) the mean value of the relative fluctuation was observed to be around 0.02 when the Gaussian filter with a filtering window size of 1/6 oscillation cycle was used. This indicates that when the relative fluctuation is close to 0.02, the curve is similar to a sinusoidal one, which is infinitely smooth.

The relative fluctuations of the lift coefficients for all cases with different reduced frequencies are summarized in Table 4.2. At lower reduced frequencies, the relative fluctuation was larger when compared to those at higher reduced frequencies, suggesting less effective mitigation of the gust at low reduced frequencies. The relative fluctuations for cases with higher reduced frequency ($k \geq 2.86$) are very similar to each other. Based on the cases tested in the current study a reduced frequency of $k = 2.86$ was found to be the optimal reduced frequency for gust mitigation. The corresponding oscillating frequency for the optimal reduced frequency ($k = 2.86$) was the same as the dominant vortex shedding frequency found from the PSD analysis of the velocity in the wake region of the stationary airfoil interacting with the gust as shown in Fig. 4.7(b). An increase in reduced frequency beyond this point did not have a significant impact on vertical gust mitigation. As reported by Fisher *et al.* [47], compared to a stationary wing, the flapping wing is less sensitive to turbulent environment and the flapping motion dominates the creation of major flow features when the reduced frequency is increased. In this study, the same phenomenon has been observed in the context of gust-pitching airfoil interaction.

Table 4.2: Relative fluctuation for pitching airfoil cases with varying reduced frequencies with the fixed pitching amplitude $\theta_o = 10°$.

Cases	Reduced Frequencies	Relative fluctuation
1	0.79	8.36×10^{-2}
2	1.16	4.53×10^{-2}
3	2.86	2.16×10^{-2}
4	3.64	2.11×10^{-2}
5	4.46	2.12×10^{-2}

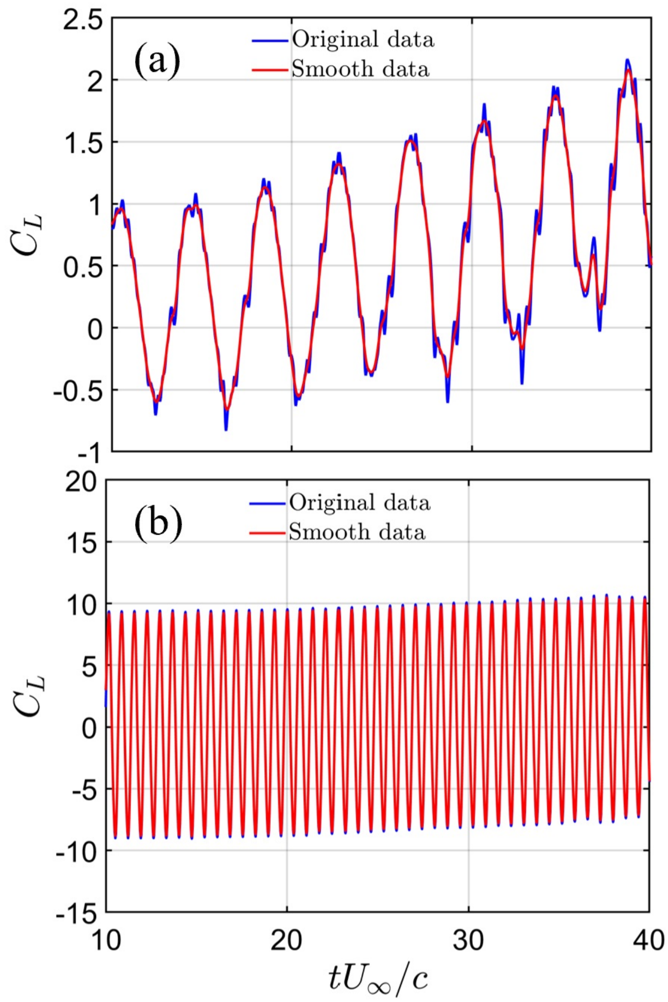

Figure 4.12: Smoothed C_L compared to the original C_L of pitching airfoils at (a) $k = 0.79$ and (b) $k = 4.46$.

Analysis of the flow fields was done to correlate flow structures with the effects of reduced frequencies discussed above. Figure 4.13 depicts the instantaneous vorticity fields around pitching airfoils with three (i.e., low, medium and high) reduced frequencies during the early (left column of Fig. 4.13) and later (right column) stages of the gust-wing interaction. At the early stage of the gust development, the vortex shedding pattern from the airfoil was similar to that of an airfoil pitching at the same reduced frequency under a uniform flow condition. Smaller shed vortices were formed on the upper side of the rapidly pitching airfoil compared to the cases with lower reduced frequencies. At high reduced frequencies, such as $k = 2.86$ and 4.46, a reverse von Karman vortex street was formed, reflective of the thrust generation behavior observed in the data. In general, wake structures were unaffected by the gust during the early gust development stage.

Compared to the early gust-wing interaction stage, during the later interaction stage larger vortices appeared on the top of the pitching airfoil, especially for the low reduced frequency case ($k = 0.79$), see Fig. 4.13(b). When the airfoil was pitched at a reduced frequency higher than $k = 2.86$, as shown in Fig. 4.13(d) and (f), the vortices near the top surface were much smaller than those at lower reduced frequencies at the same stage of gust development. These vortices also evolved more slowly and remain closer to the airfoil at higher reduced frequencies when compared with the lower reduced frequency cases. This suggests that at higher pitching frequencies the flow features were dominated by the pitch motion, which in turn substantially suppressed the effects of the gust. The effect of reduced frequency was similar when tested for a lower gust ratio case (GR $= 0.21$). Unlike the pitch-down control strategy presented in Section 4.2.2, the gust-wing interaction was always dominated by the pitch motion when the reduced frequency was sufficiently high. As a result, the highly unsteady lift fluctuation induced by the gust can always be fully mitigated by the pitching airfoil during long-duration gust-wing interaction. When the gust was fully developed, the only impact of the gust on the pitching airfoil was to increase its average lift coefficient, as demonstrated in Fig. 4.10. Based on this result, it is apparent that an oscillating airfoil motion could be used to mitigate a gust during the gust development, with potential to return to steady attached flow once the unsteady gust has stabilized.

4.2.3.2 Effect of Pitching Amplitude

The results in the previous section demonstrated that increasing reduced frequency with a constant pitching amplitude of $\theta_o = 10°$ can mitigate the vertical gust effects. A reduced frequency of $k = 2.86$ was the most effective one tested in mitigating the gust effects. This section aims to gain insight into the effects of pitching amplitudes (i.e. Strouhal numbers when the reduced frequency is fixed) on gust mitigation by varying the pitch amplitude at the optimal reduced frequency $k = 2.86$. The cases tested are summarized in Table 4.3.

Figures 4.14 and 4.15 show the instantaneous forces histories for pitching airfoils with different pitching amplitudes at the optimal reduced frequency $k = 2.86$ during the early and later gust-wing interaction stages, respectively. Although the vertical gust during the later gust-wing interaction stage was much stronger

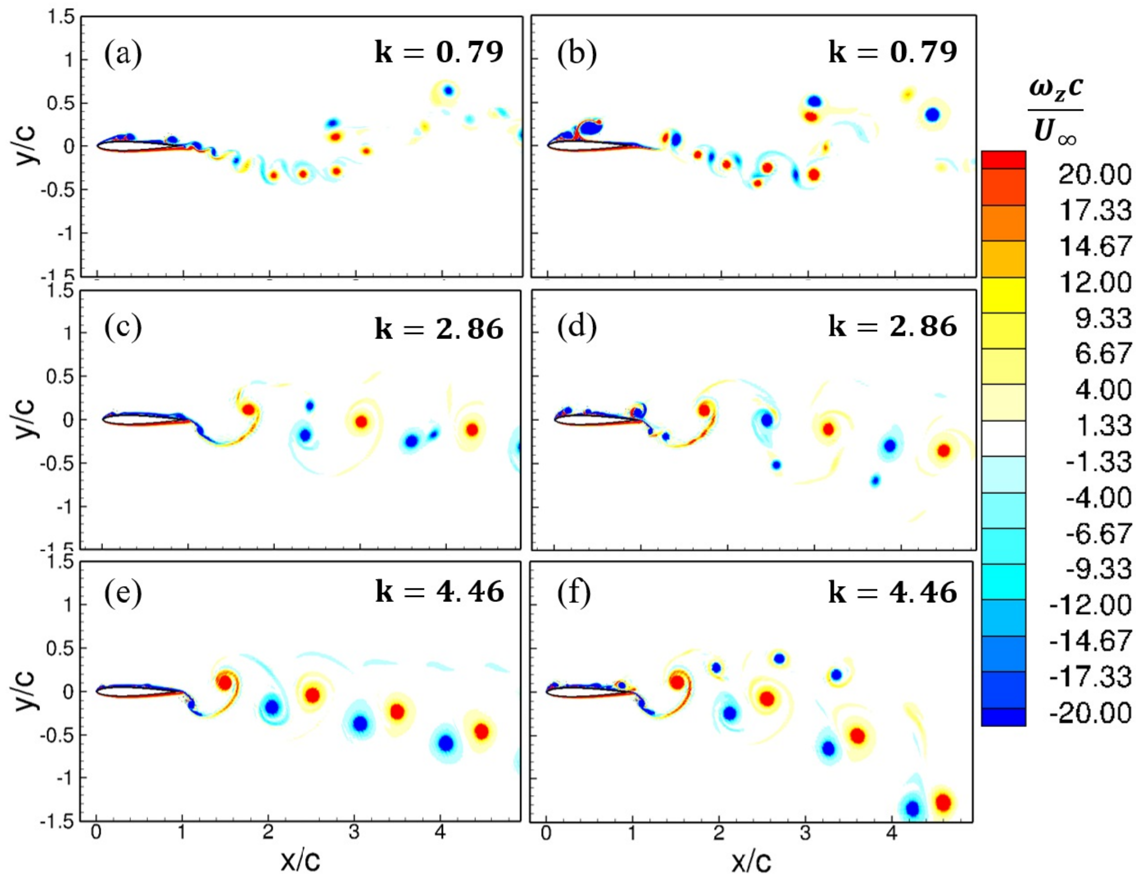

Figure 4.13: Instantaneous vorticity fields of pitching airfoils at different reduced frequencies during the early (left) and later (right) gust-wing interaction stages. (a) and (b): the reduced frequency $k = 0.79$; (c) and (d): the reduced frequency $k = 2.86$; and (e) and (f): the reduced frequency $k = 4.46$.

Table 4.3: Pitching airfoil cases at the optimal reduced frequency with varying the pitching amplitude.

Cases	Pitching Amplitude (θ_o)	Strouhal Numbers
1	$2°$	0.06
2	$4°$	0.12
3	$8°$	0.24
4	$16°$	0.48

compared to that during the early stage, the force variation patterns for all cases were very similar during the two stages. The drag coefficient was slightly shifted towards the negative, thus enhancing thrust generation, and the lift coefficient was shifted to a more positive value, increasing the time-averaged lift. These results suggest that the pitching amplitude (correspondingly, the Strouhal number) is not a dominant factor for gust mitigation; instead, the reduced frequency is the dominant one.

Figures 4.16 and 4.17 present the time-averaged aerodynamic forces and power consumption of the pitching airfoil with different pitching amplitudes at the optimal reduced frequency $k = 2.86$ during the early and later gust-wing interaction stages. For lower pitching amplitudes (i.e. $\theta_0 = 2°$ and $4°$), drag was produced during the early gust-wing interaction stage while thrust is produced in the later gust-wing interaction stage; see Fig. 4.16(a). For larger pitching amplitudes thrust was always produced during both the early and later gust-wing interaction stages; see

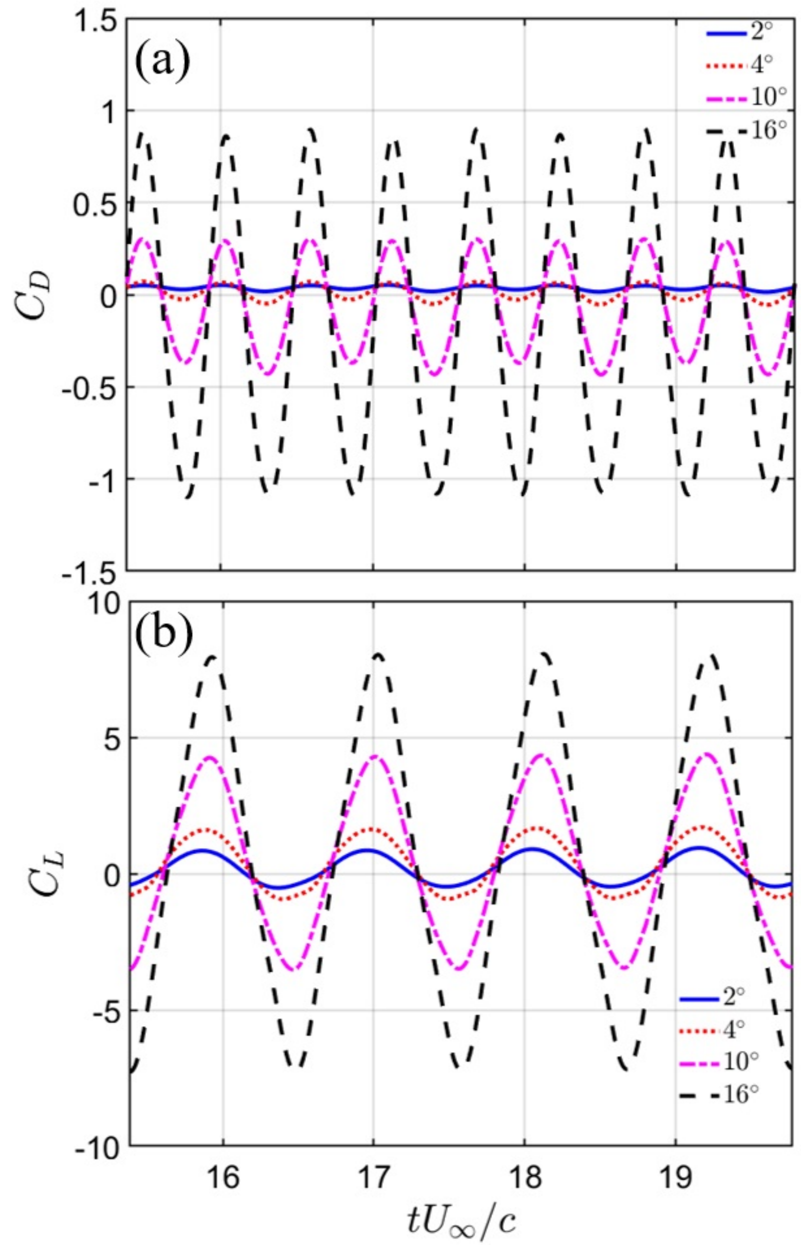

Figure 4.14: (a) Drag and (b) lift coefficient histories for the pitching airfoil with different pitching amplitudes during the early stage of gust development at $k = 2.86$.

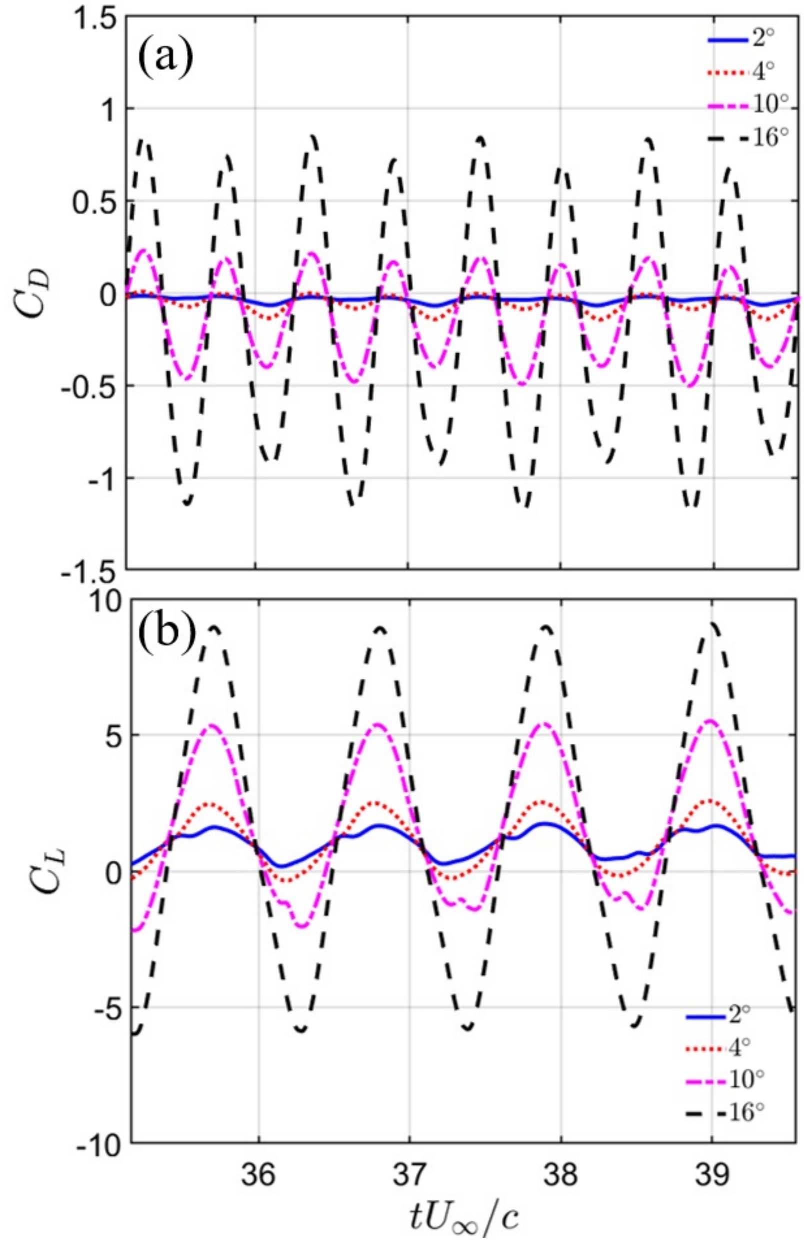

Figure 4.15: (a) Drag and (b) lift coefficient histories for the pitching airfoil with different pitching amplitudes during the later stage of gust development at $k = 2.86$.

Fig. 4.16(b). The time-averaged thrust increased with the pitching amplitude. The time-averaged lift coefficients seem not to be significantly affected by the pitching amplitude during the early gust-wing interaction stage. However, high pitching amplitudes can increase the time-averaged lift coefficients during the later gust-wing interaction stage, and lift is maximized when the pitching magnitude is $10°$. As expected the power consumption increased when the pitching amplitude increased, as shown in Fig. 4.17. One interesting observation is that the power consumption of the pitching airfoil during the later gust-wing interaction stage was smaller than that during the early stage, especially when the pitching amplitude was large.

To measure the gust mitigation effectiveness the relative fluctuation approach used in Section 4.2.3.1 is used for varied pitching amplitudes. Table 4.4 documents the relative fluctuations for the pitching airfoils with different pitching amplitudes at the optimal reduced frequency $k = 2.86$. These results showed that the relative fluctuations for different pitching amplitudes all have similar values. It is clear that the effects of the gust can be mitigated even with the lowest pitching amplitude at the optimal reduced frequency. This again confirms that the reduced frequency is the dominant factor for mitigating the effects of vertical gusts.

The flow fields around the pitching airfoil with different pitching amplitudes at the optimal reduced frequency $k = 2.86$ are shown in Fig. 4.18, which depicts the instantaneous vorticity fields during the early (left column) and later (right column) gust-wing interaction stages. During the early gust-wing interaction stage, vortices were not formed near the leading edge for lower pitching amplitudes (i.e. $\theta_0 = 2°$ and $4°$); see Fig. 4.18(a) and (c). However, for the case with $\theta_0 = 16°$, these vortices

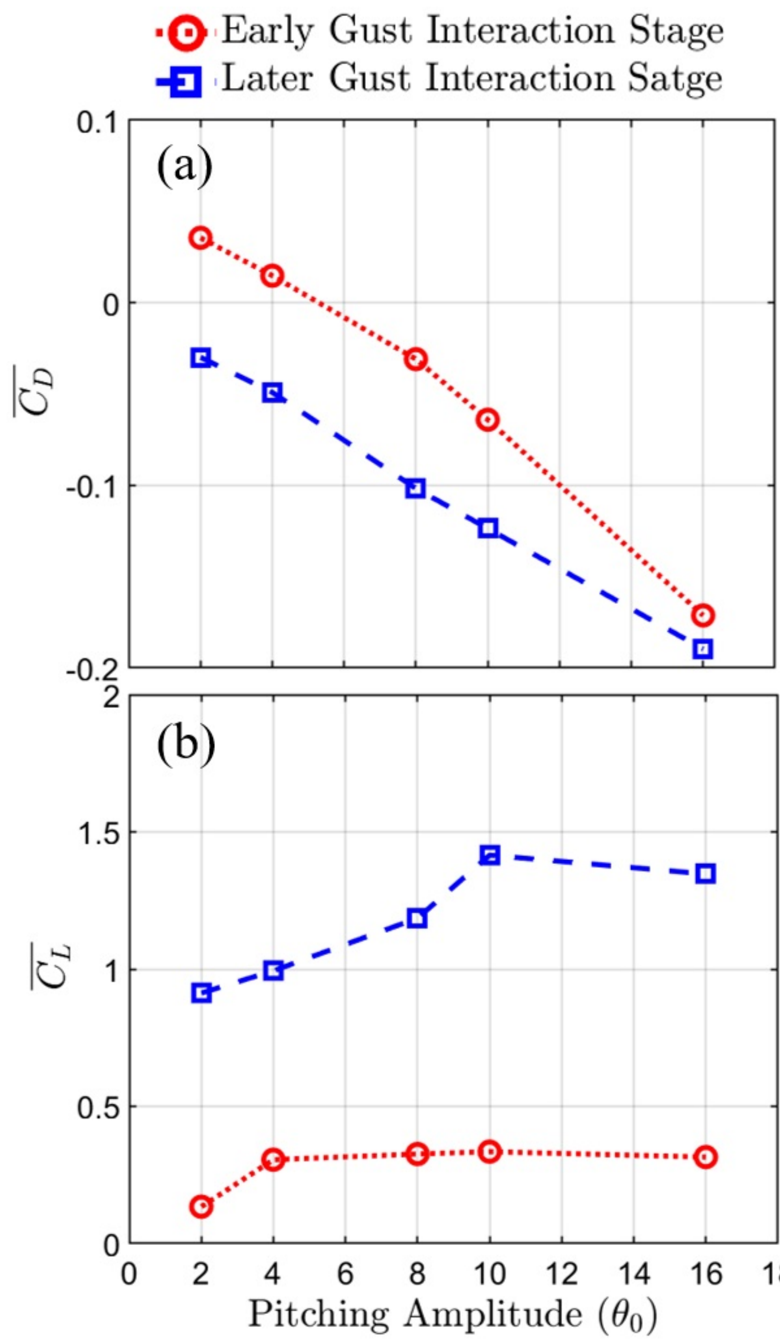

Figure 4.16: Time-averaged aerodynamic forces before and after intensive gust-wing interaction. (a) Drag coefficient and (b) lift coefficient for the stationary and pitching airfoils with different pitching amplitudes at $k = 2.86$.

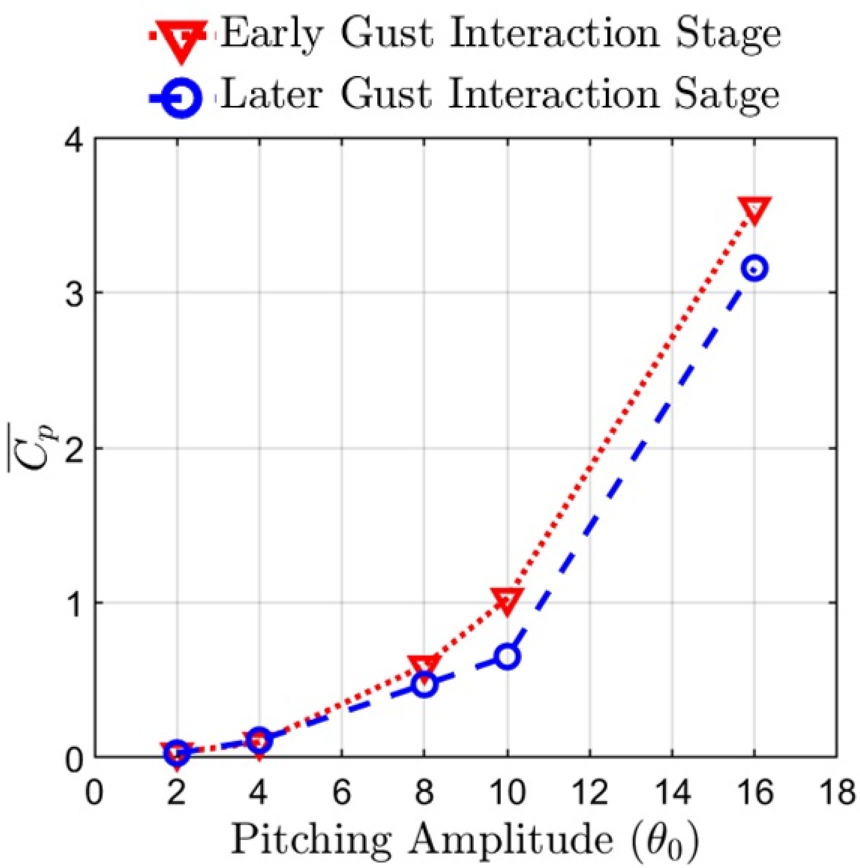

Figure 4.17: Time-averaged power coefficients of pitching airfoils with different pitching amplitudes at $k = 2.86$.

Table 4.4: Relative fluctuation for pitching airfoil cases with varying pitching amplitudes θ_o at the optimal reduced frequency $k = 2.86$.

Cases	Pitch Amplitude	Relative fluctuation
1	$2°$	1.89×10^{-2}
2	$4°$	1.99×10^{-2}
3	$8°$	2.12×10^{-2}
4	$10°$	2.16×10^{-2}
5	$16°$	2.28×10^{-2}

were formed. During the later gust-wing interaction stage, LEVs were present in all cases. The size of these vortices was smaller when the airfoil was pitched with lower pitching amplitude due to the smaller AoA of the pitching motion. In addition, Fig. 4.18(e) and (f) reveal that the airfoil pitching at larger pitching amplitudes results in stronger and more organized reverse von Karman vortex street in the wake region, which results in the significant increase in the thrust production observed earlier.

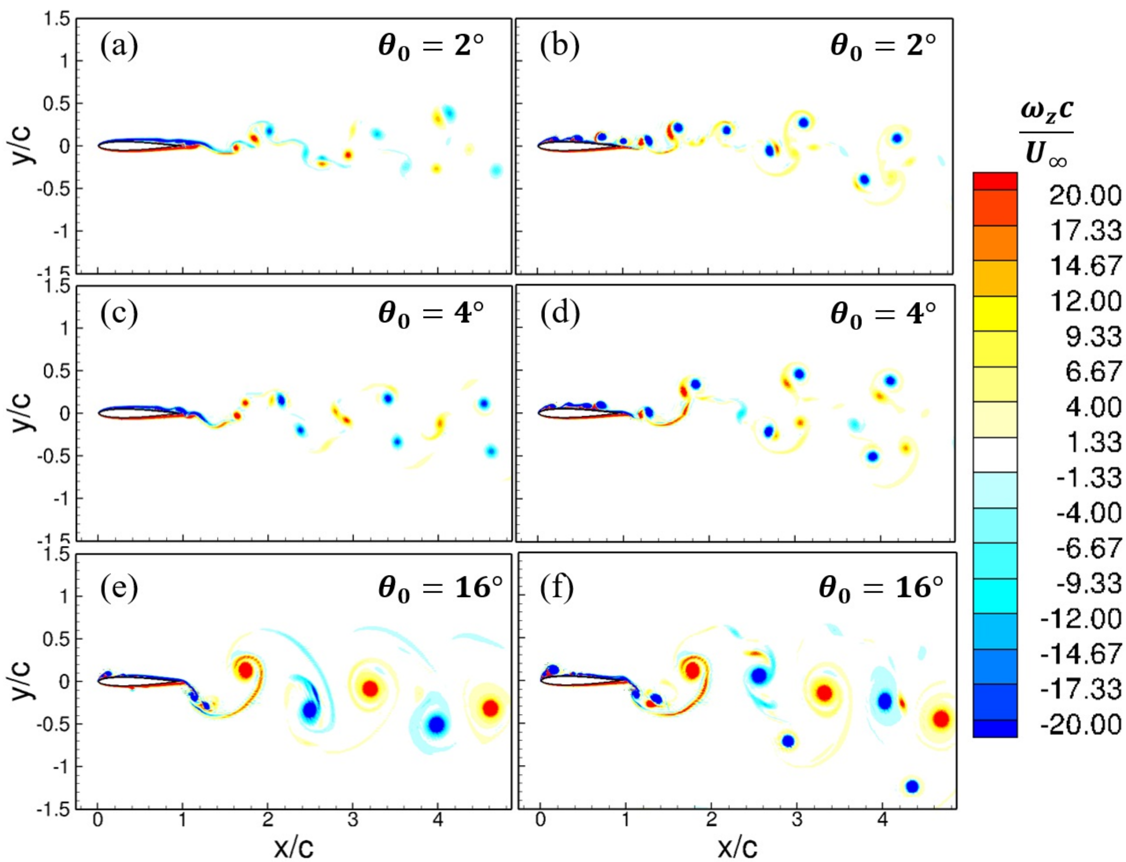

Figure 4.18: Instantaneous vorticity fields of pitching airfoils at different pitching amplitude at $k = 2.86$ during the early (left) and later (right) gust interaction stages. (a) and (b): the pitching amplitude $\theta_0 = 2°$; (c) and (d): the pitching amplitude $\theta_0 = 4°$; and (e) and (f): the pitching amplitude $\theta_0 = 16°$.

4.3 Summary of Major Findings

This chapter detailed the numerical investigation of gust-wing interaction at low Reynolds numbers. Two gust mitigation strategies have been demonstrated in this study. The following are the key findings from the results presented in this chapter.

- For a stationary airfoil the gust caused an increase in lift followed by a highly unsteady stall process.

- Large pitch down gust responses were observed to cause a negative lift with a high potential to overshoot into a negative angle stall state.

- A step-wise pitch-down approach was demonstrated as an effective method for maintaining steady lift even when the AoA generated by the gust continued to grow.

- Oscillating the airfoil at high reduced frequencies overcomes the flow disturbances caused by the vertical gust. However, the gust significantly increased both the lift and thrust generated by the oscillatory motion, with the average lift shifting above the static stall lift.

- At the optimal reduced frequency the Strouhal number, which was varied by controlling oscillating amplitude, had little effect on the relative fluctuation. This result suggests that even small amplitude oscillations can be used to mitigate gusts.

Chapter 5: Numerical Study of Flapping-Wing Flow Physics in Nonuniform Freestream

In this chapter, a numerical study is conducted to understand the impact of nonuniform freestream on the aerodynamic performance of an oscillating airfoil. In this part of the current study, “nonuniform” and “unsteady” are used to describe the flow as the 2D simulations conducted have been shown not to produce true turbulent behaviors. However, the nonuniform flow environment is still reflective of unsteady environments observed in nature. In this case, the nonuniform flow field was generated by array of inline circular cylinders upstream of the airfoil. A NACA0012 airfoil was placed at the location $7c$ downstream of the array of cylinders and oscillated in the nonuniform freestream. The goal of this chapter is to provide the reader with an understanding of how an oscillating airfoil generates more thrust in highly unsteady environments. The underlying flow physics driving this increased thrust generation is also analyzed.

5.1 Computational Setup

This study used an array of cylinders to generate an unsteady flow environment for a pitching airfoil as shown in Fig. 5.1. The dimensions of the computational domain are loosely based on ongoing wind tunnel tests at the U.S. Army Research Lab (DEVCOM ARL). Figure 5.1 also shows the boundary conditions used in the numerical simulation. For these simulations a fixed inlet and a typical outlet boundary were used. For the top and bottom walls of the domain, inviscid wall boundary conditions were used to save computational cost while mimicking the wind tunnel wall effect. To allow the disturbances generated by the cylinders to evolve, the distance between the cylinder array and the NACA 0012 airfoil was set to $7c$, where c is the chord length of the airfoil. The array of cylinders was placed $50c$ downstream of the inlet. The ratio of distance between cylinders (L) to the cylinder diameter (d), i.e. $\frac{L}{d}$ was 3. The freestream Mach number was fixed at 0.1 for all cases.

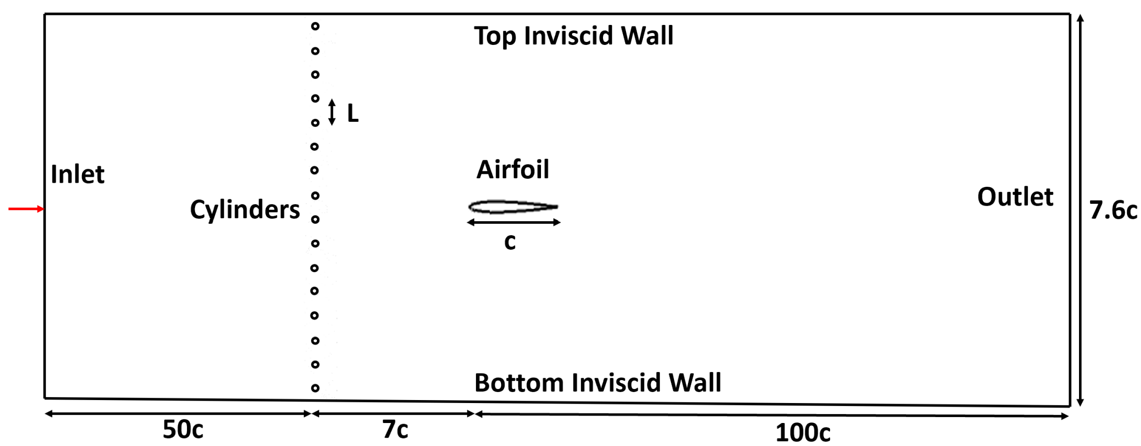

Figure 5.1: Computational domain of the inline configuration of cylinders with airfoil.

5.1.1 Characterization of unsteadiness

To evaluate the unsteadiness generated by the cylinder array, the flow field downstream of the array was first characterized without the airfoil. As illustrated in Fig. 5.2(a), the vortices produced by the cylinder array interacted with each other and decreased in intensity as they convected downstream. Weaker and less-coherent vortices were observed near the location where the wing would be placed in later studies, shown in Fig. 5.2(a), as compared to those near the cylinders. Note that for this study the quarter chord location of the airfoil was positioned at $(x, y) = (0, 0)$. A numerical probe, equivalent to a hot-wire probe in experiments but in a non-intrusive sense, was placed at $(0, 0)$ with no airfoil present. Fig. 5.2(b) depicts the velocity power spectrum for this probe measured over 100 convective times. The power spectral density (PSD) of the velocity shows that the slope in the energy decay region is approximately -3. Typically vortices break down into smaller scales due to 3D vortex stretching, resulting in an energy decay region of $-\frac{5}{3}$. This indicates that compared to 3D turbulence, 2D unsteady flow environments create larger while weaker vortex structures to interact with the oscillating airfoil. However, no matter in 2D or 3D, the inherent randomness nature of the unstructured flow environment is comparable to each other (see a recent relevant work in [127]). Therefore, conclusions from 2D simulations based on time- and space-averaged phenomena can be readily extended to 3D; see, for example, a work by Visbal [107].

Several Reynolds numbers, based on the chord length of the airfoil, were examined in this study. These chord based Reynolds number varied from $Re = 500 - 10,000$. This causes the Reynolds number, based on the diameter of the cylinders, to vary since the ratio of the airfoil chord length to the diameter of the cylinder is approximately 3.8. The turbulence intensity, defined as the ratio between the standard deviation of the total velocity fluctuation to the mean velocity, at the probe location for different Reynolds numbers tested is presented in Table 5.1. Note that the Reynolds numbers in Table 5.1 are based on the chord length of the airfoil. As shown in Table 5.1, the turbulence intensity increases as the Reynolds number (Re_c) increased, which was caused by the method of generating unsteadiness in this study. The result in Table 5.1 are in line with Watkins *et al.* [10], which documented that turbulence intensity could regularly exceed 25% at low Reynolds numbers in the atmospheric boundary layer.

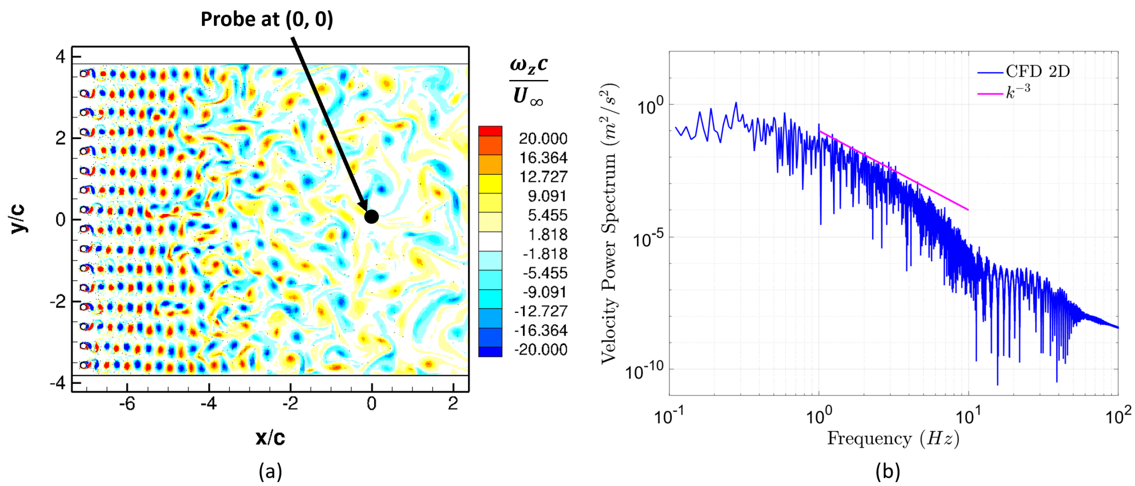

Figure 5.2: (a) 2D flow field in the downstream of an array of cylinders and (b) Velocity Power Spectrum plot at the probe location $(0, 0)$.

5.1.2 Boundary Conditions

When studying oscillating airfoils, especially at higher Strouhal numbers, boundary conditions must be selected with sufficient care. In this study the computational domain was originally selected to align with common wind tunnel dimensions for experimental validation [127]. This results in an inviscid wall boundary condition about 3.8 chord length away from the pitching airfoil, as shown in Fig. 5.1. To

Table 5.1: Turbulence Intensity at different Reynolds Numbers

Reynolds Numbers (Re_c)	Turbulence Intensity (TI%)
500	15.83
2000	27.65
4000	36.68
7000	38.43
10,000	42.09

evaluate the effect of this boundary condition the distance from the airfoil to the inviscid walls was varied from $3.8c$ to $50c$, where c is the airfoil chord length.

Figure 5.3 shows the drag coefficient history for the pitching airfoil at $Re = 10,000$ for $St = 0.2$ and $St = 0.4$. For lower Strouhal numbers (i.e., 0.2 in this test), the inviscid wall boundary conditions enforced on the small domain had little impact on the drag compared to those on the large domain; see Fig. 5.3 (a). The smaller domain merely resulted in a slight variation in the peaks and troughs of the drag coefficients. However, at the higher Strouhal number, $St = 0.4$, the force history for the small computational domain became notably aperiodic from cycle to cycle, with large over-predictions of the force compared to the larger domain; see Fig. 5.3 (b). Interestingly, despite this apparent instantaneous force difference, the airfoil's time-averaged drag coefficients, calculated over the last 20 periods of both numerical simulations, were -0.3229 and -0.3391 for the small and large domains, respectively. The same phenomenon was observed at different Reynolds numbers.

The source of the wall effects at higher Strouhal numbers is illustrated in Fig. 5.4, which depicts the instantaneous pressure coefficient field over a pitching airfoil at $St = 0.2$ and $St = 0.4$ for $Re = 10,000$ in the smaller computational domain. The pressure wave reflection from the inviscid wall was mild for the lower Strouhal number, as shown in Fig. 5.4 (a). For $St = 0.4$ pressure waves were reflected back to the airfoil from the top and bottom walls, interacting with the airfoil (Fig. 5.4b). This indicates that for higher Strouhal numbers, even though the average forces from a small computational domain may be close to those from a large domain, the flow behavior can be highly effected by the inviscid walls in the computational domain. In the current study, the Strouhal number was kept below $St = 0.3$ to minimize the near-wall effects.

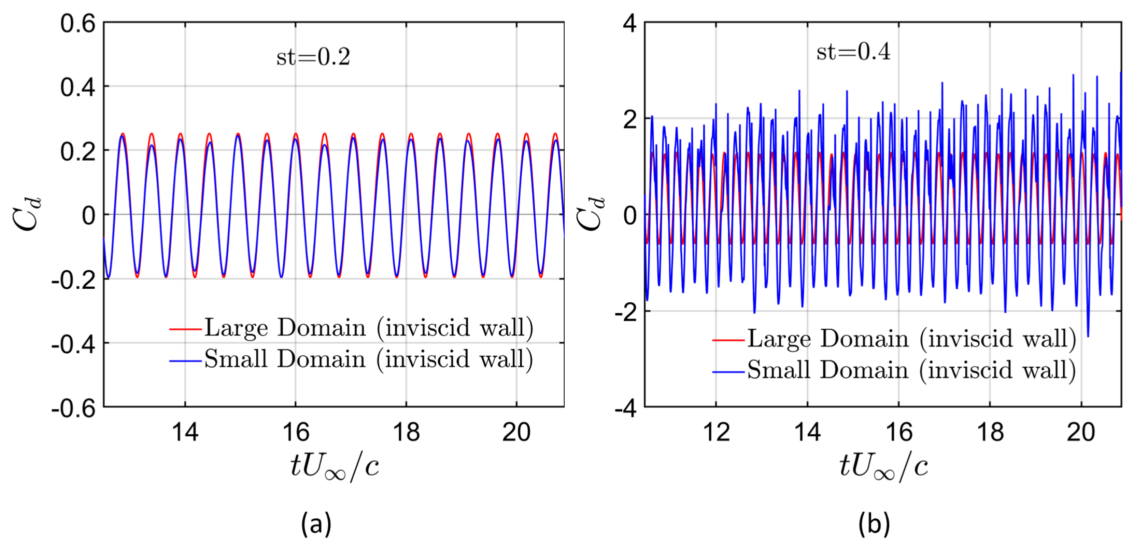

Figure 5.3: Drag coefficient under uniform flow condition at (a) $St = 0.2$ and (b)$St = 0.4$ for $Re = 10,000$ for large and small computational domains.

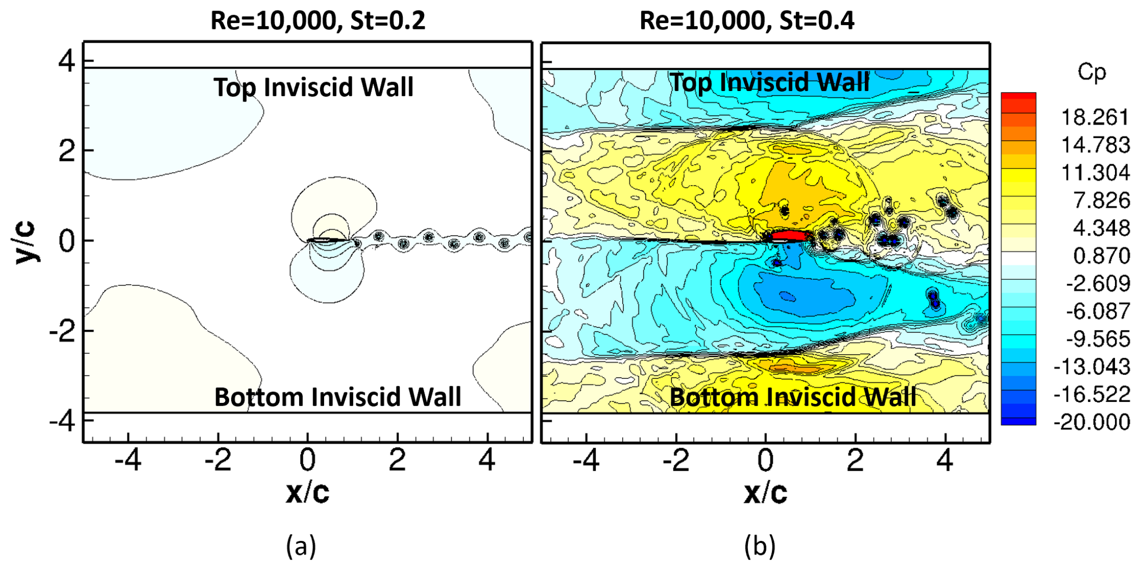

Figure 5.4: Instantaneous pressure coefficient fields at (a) $St = 0.2$ and (b)$St = 0.4$ for $Re = 10,000$ in small computational domains similar to that in wind tunnel tests.

5.2 Results and Discussion

5.2.1 Uniform Flow Baseline

First the baseline behavior of a pitching airfoil with a fixed pitching amplitude $\theta_0 = 8°$ in uniform flow conditions was calculated for comparison with those in unsteady flow environments discussed later. For this baseline the Strouhal number was varied from 0.1 to 0.3 at different Reynolds numbers based on the airfoil chord length, namely, 500, 2,000, 4,000, 7,000, 10,000, and 30,000.

These results were compared with results from Sentruk and Smits [123], shown in Fig. 5.5 (a), in which thrust production of oscillating airfoils were numerically analyzed. Fig. 5.5 (a) presents the average thrust coefficients for different Reynolds numbers over a range of Strouhal numbers, and Fig. 5.5 (b) depicts the same information but plotted against Reynolds number for later comparisons. The results of the current study agreed well with those from Sentruk and Smits [123]. A key observation is that increasing Reynolds number acts to increase mean thrust generation at a fixed Strouhal number. These results also make clear that the airfoil generates drag at low Reynolds and Strouhal numbers in uniform flow conditions.

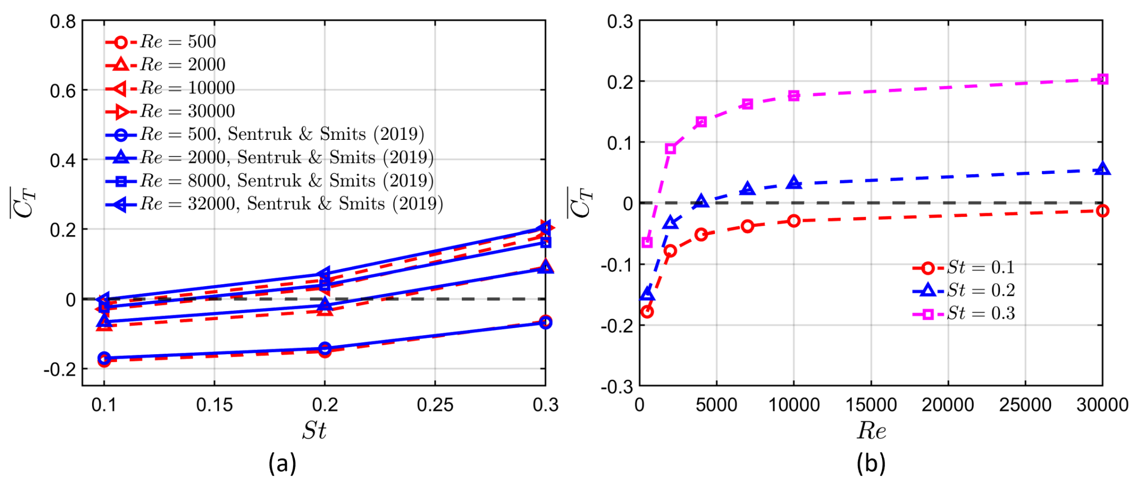

Figure 5.5: Time-averaged thrust coefficients over airfoil under uniform flow condition (a) as a function of St for different Reynolds numbers and comparison with Sentruk & Smits [123] and (b) as a function of Re for different Strouhal numbers.

An analysis of the flow fields was also carried out to identify key flow features at different Reynolds and Strouhal numbers. Figure 5.6 and 5.8 shows the normalized vorticity fields around the oscillating airfoils at Strouhal numbers of $St = 0.1$ and 0.3, respectively. For the flow fields at $St = 0.1$ and lower Reynolds numbers (i.e., 500 and 2,000 here) showed typical von Kármán vortex street features, a typical drag production wake type. The vorticity fields at St = 0.1 and higher Reynolds numbers (i.e., 10,00 and 30,000 here) showed a neutral wake type, which does not create net drag or thrust. At $St = 0.3$, reverse von Kármán vortex streets were observed at all Reynolds numbers. Although the presence of a reverse von Kármán vortex street indicates that there exists a jet in the wake of the airfoil, it does not necessarily create thrust on the airfoil at low Reynolds numbers, such as the $Re = 500$ case presented here. At larger Reynolds numbers where the inviscid flow interaction dominates, the reverse von Kármán vortex street is an indication of thrust production over the upstream airfoil; see the correspondence between Fig. 5.5 and Fig. 5.8 for the high Reynolds number cases, e.g., $Re = 2,000, 10,000$ and $30,000$.

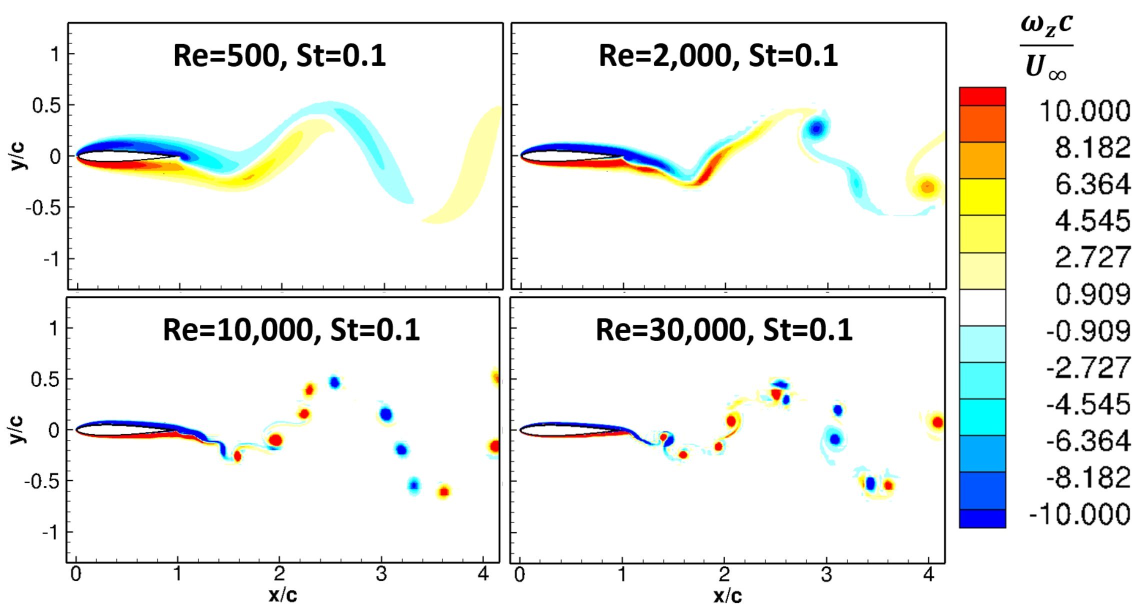

Figure 5.6: Instantaneous vorticity fields over a pitching airfoil under uniform flow condition at $St = 0.1$.

5.2.2 Pitching Airfoils in Non-uniform Upstream Flows

This section investigates the effect of non-uniform flow environments created by an upstream array of cylinders on the propulsive performance of a pitching airfoil.

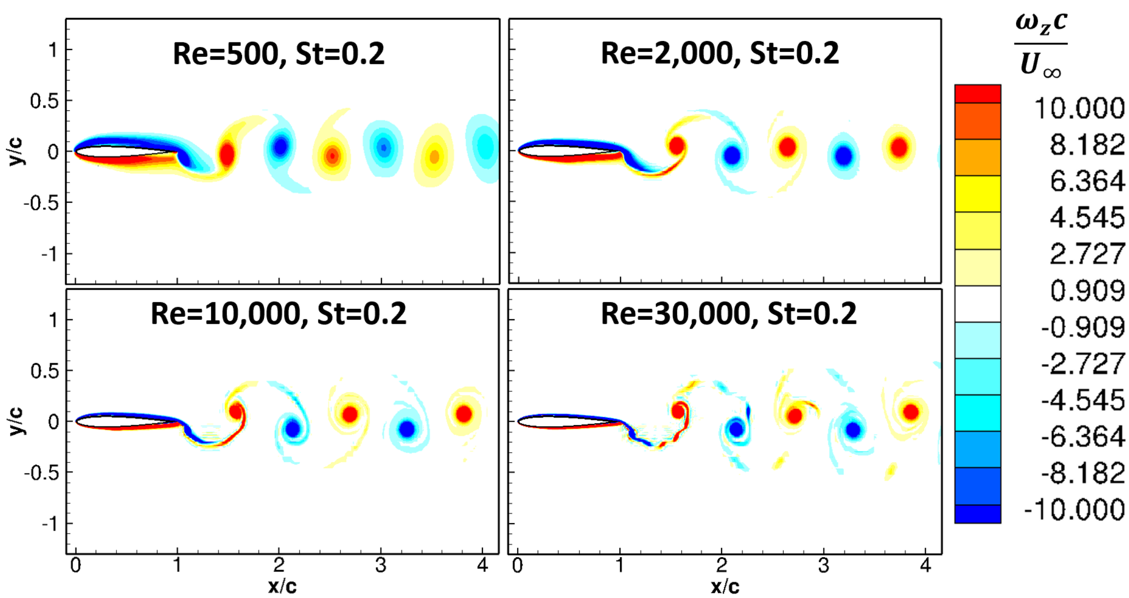

Figure 5.7: Instantaneous vorticity field over airfoil under uniform flow condition at $st = 0.2$.

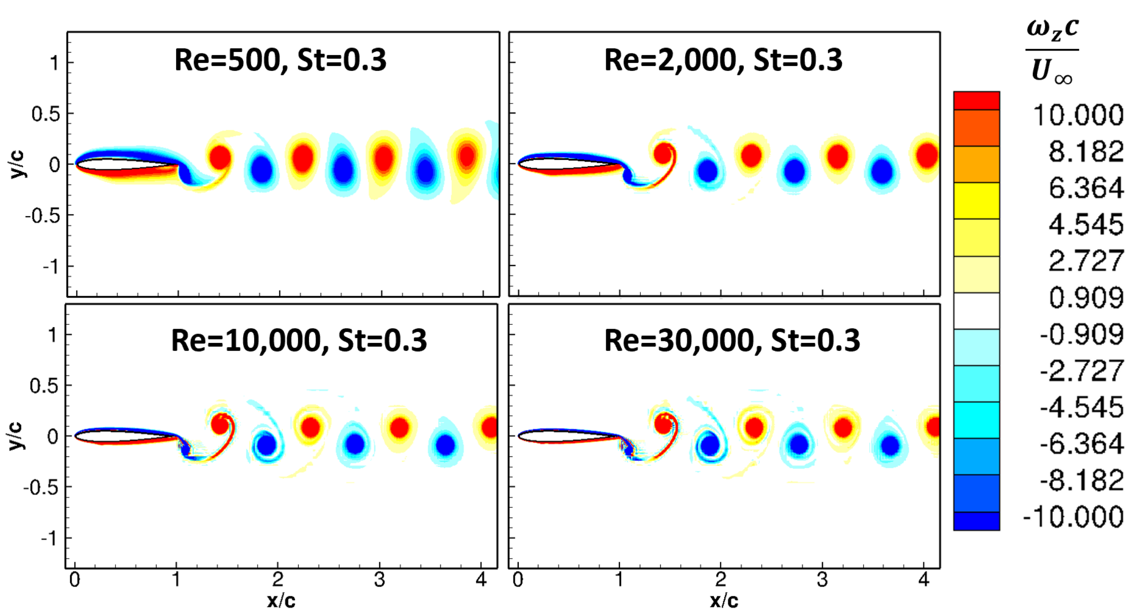

Figure 5.8: Instantaneous vorticity fields over a pitching airfoil under uniform flow condition at $St = 0.3$.

The Reynolds numbers based on the airfoil chord length were varied from 500 to 10,000 in this section, while all other variables were kept the same as those under uniform flow conditions.

5.2.2.1 Visualization of instantaneous flow fields and aerodynamic forces

Figure 5.9 shows the time history of thrust coefficient at different Strouhal numbers for different Reynolds numbers. In general the thrust coefficients show irregular fluctuations due to unsteadiness in the ambient flow environment. At $St = 0.1$, except for $Re = 500$, the thrust coefficient histories at different Reynolds numbers have more intense fluctuations compared to those at higher Strouhal numbers. Similar to the observations from [128] where the interaction between gusts and an oscillating airfoil is investigated, energetic pitching motions can suppress the unsteady effect from ambient flows. Moreover, as will be presented in the next subsection, the pitching motion can also take advantage of the energy-containing unsteady ambient flows to boost thrust production.

Fig. 5.10 depicts the instantaneous vorticity fields for Reynolds number 500 at $St = 0.2$ and $St = 0.3$ under non-uniform flow conditions. The vortices in the ambient flow were observed to have a limited effect on the airfoil's boundary layer due to their lower strength, when compared with the vortices created by the pitching airfoil. The reverse von Kármán vortex street was slightly deflected, Fig. 5.10(b), when compared to the horizontal wake shown in Fig. 5.8) by the ambient flow unsteadiness. This was especially true at higher Strouhal numbers and is similar to the observations from the interaction between an oscillating airfoil and a weak shear

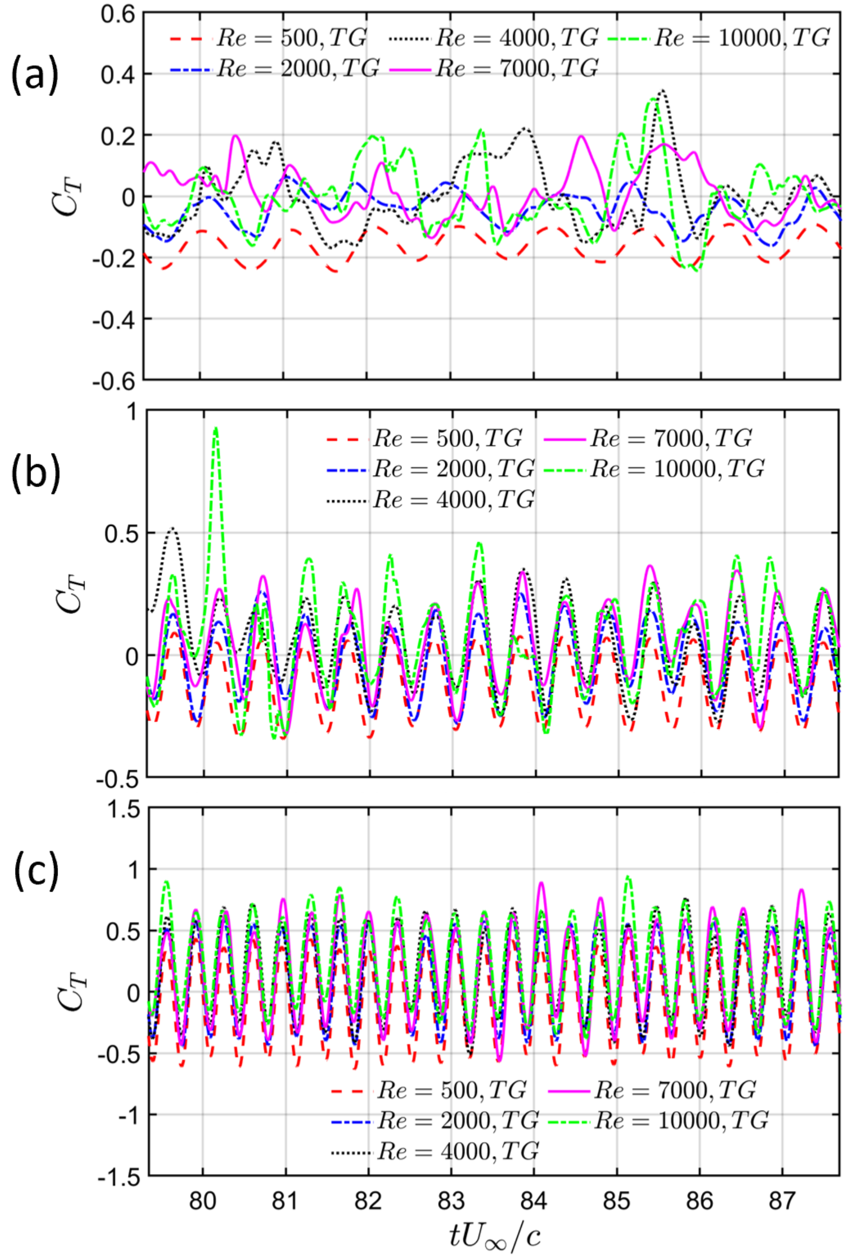

Figure 5.9: Instantaneous thrust coefficient histories for the pitching airfoil under non-uniform flow conditions at different (a) $st = 0.1$, (b) $st = 0.2$ and (c) $st = 0.3$ for different Re.

layer as reported in [129].

The wakes become more chaotic as the Reynolds numbers increase due to the intense interactions between the upstream vortices and oscillating airfoil wakes; see

Fig. 5.11 (a) and (b). This unsteady interaction is the driving factor behind the intense thrust fluctuations observed in Fig. 5.9, especially at small Strouhal numbers. One notable feature is here are the large increases in magnitude of thrust and drag in some cycles. One unusual thrust boost was observed at non-dimensional time ($t^* = tU_\infty/c$) around $t^* \approx 80.15$ for the $St = 0.2$ and $Re = 10,000$ case, and an unusual drag increase occurred at $t^* \approx 86$ for the $St = 0.1$ and $Re = 10,000$ case.

The instantaneous vorticity and pressure fields for the excess thrust case noted above are shown in Fig. 5.11. Just prior to the increased thrust generation, a pair of clockwise and counterclockwise vortices labeled 'A' (see Fig. 5.11 (a)) from the upstream unsteady flow environment are close to the leading edge of the airfoil's lower surface. At the same time, the leading edge of the airfoil is pitching up and creating the leading edge vortex (LEV) '1' on the lower surface of the airfoil. Fig. 5.11 (c) shows the negative pressure regions generated at this time for the vortices. As the airfoil continued pitching upward it started to interact with impinging vortex 'B', as shown in Fig. 5.11 (b). The combined effects of these vortices acted to create a low pressure region over the entire lower surface of the airfoil, thus producing a higher-than-usual thrust force as a favorable condition for thrust enhancement.

A different vortex interaction occurred which generated the significant drop in thrust coefficient at $St = 0.1$ for $Re = 10,000$ around $t^* = 86$ in Fig. 5.9 (a). The flow fields around that time are shown in Fig. 5.12 with instantaneous vorticity and pressure fields. In this case a pair of vortices 'A' and another pair of vortices 'B' were located near the upper and lower surfaces of the airfoil, respectively, as shown in Fig. 5.12 (a). At this instance, the leading edge of the airfoil Was pitching

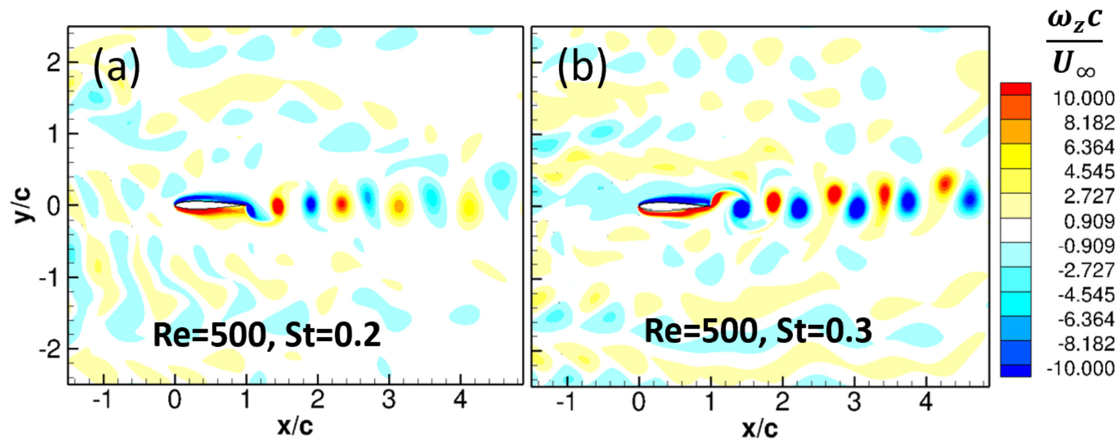

Figure 5.10: Instantaneous vorticity field over airfoil under non-uniform flow conditions at (a) $St = 0.2$ and (b) $St = 0.3$ at $Re = 500$.

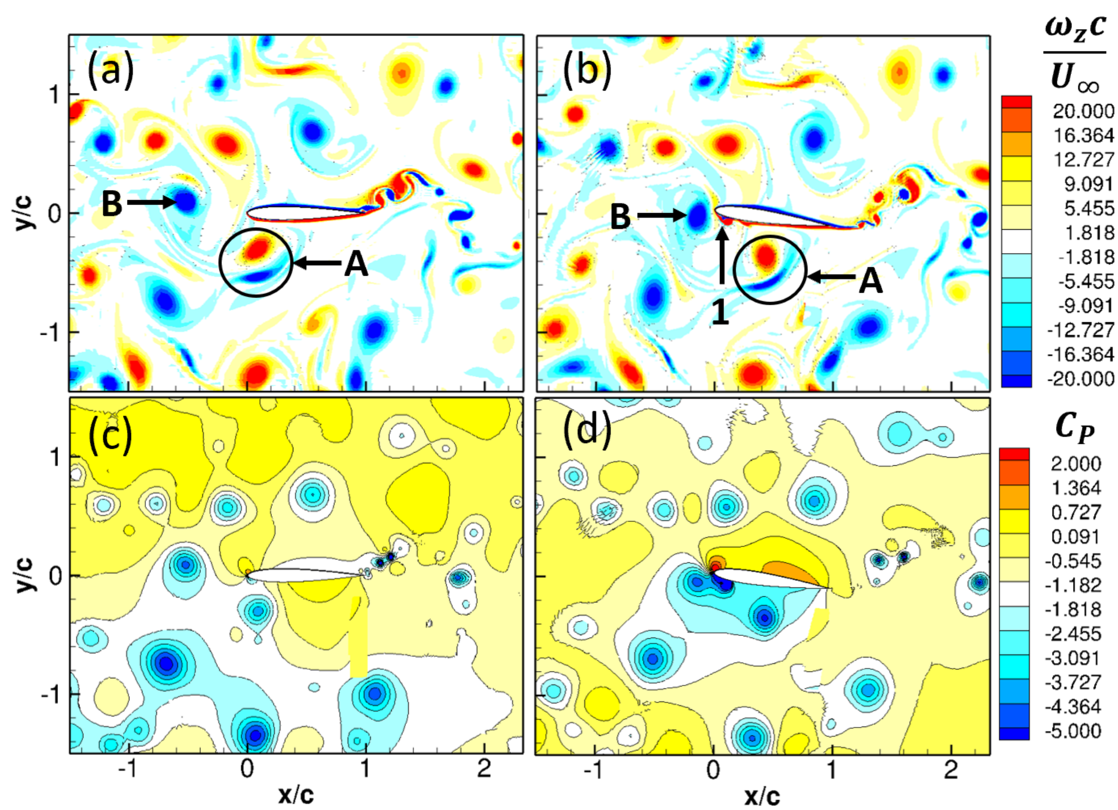

Figure 5.11: Instantaneous vorticity and pressure fields over airfoil (a), (c) at $t^* = 79.84$ and (b), (d) at $t^* = 80.1$, under non-uniform flow conditions at $St = 0.2$ and $Re = 10,000$.

down, which would be expected to create a high pressure region near the leading edge on the bottom surface of the airfoil, and a low pressure region on the top surface. However, due to the unfavorable vortex-airfoil interaction the vortex pair 'A' suppressed the creation of a LEV, which is typically created on the top surface of the airfoil. Meanwhile, the positive vortex in 'B' induced a low pressure region on the bottom surface of the airfoil (see the pressure evolution process in Fig. 5.12 (c) and (d)). This type of surface pressure distribution can induce large drag over the airfoil. Further, as observed from Fig. 5.12 (d), the positive vortex in 'A' and the negative one in 'B' both interact with the trailing edge vortex shed from the pitching airfoil, inducing a strong low pressure region near the airfoil's trailing edge, especially over the lower surface further contributing to the drag peak.

5.2.2.2 Aerodynamic force statistics analysis

This section examines the thrust and lift statistics for the pitching airfoil in unsteady flow environments compared to those in uniform upstream flows. Fig. 5.13 depicts the time-averaged thrust coefficients for the oscillating airfoil at various Strouhal numbers for nominal and effective Reynolds numbers, as well as their comparison with those under uniform flow conditions. The definition of the effective Reynolds number will be introduced in this section when discussing the flow unsteadiness effects. From Fig. 5.13, the average thrust coefficients unsteady flow cases were found to be consistently greater than those for uniform upstream flow cases, except for the case with $St = 0.3$ at $Re = 500$. As mentioned in the previous

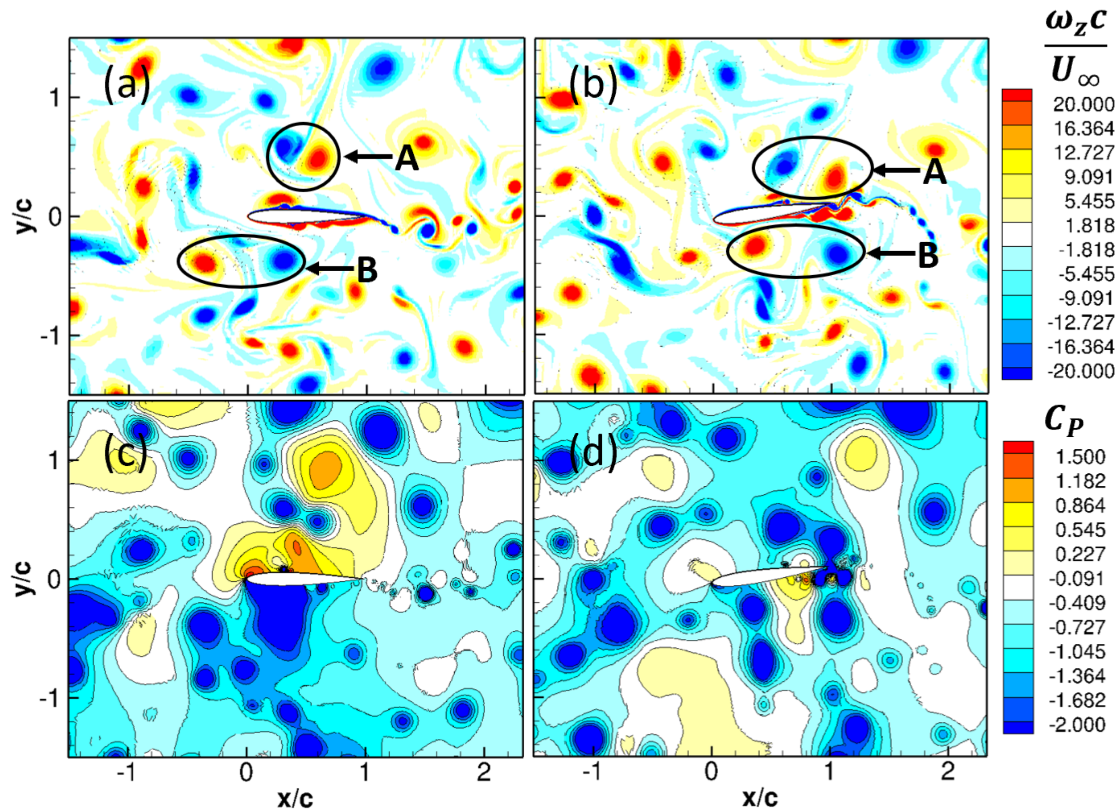

Figure 5.12: Instantaneous vorticity and pressure fields over airfoil (a), (c) at $t^* = 86.6$ and (b), (d) at $t^* = 86.1$ under non-uniform flow conditions at $St = 0.1$ and $Re = 10,000$.

subsection, the background vorticity at $Re = 500$ functions more like a weak shear layer than discrete vortex structures. It has been shown by Yu *et al.* [129] that the impact of a shear layer on thrust production of an oscillating airfoil is trivial, and can either slightly enhance or reduce thrust. The observation at $Re = 500$ here agrees with that observation.

The time averaged thrust coefficient is a function of the Reynolds and Strouhal numbers, i.e, $\overline{C_T} = f(Re, St)$. As shown in Fig. 5.13 (a), the time-averaged thrust coefficients for a fixed St appear to follow the same trend as those under uniform flow conditions but cases with unsteady incoming flow consistently produced greater thrust with increased Reynolds numbers. This suggests that the unsteadiness caused by the upstream array of cylinders has a similar effect as increasing the velocity experienced by the airfoil.

An analysis was performed to approximate the effective Reynolds number in order to demonstrate how Reynolds number is changed due to unsteadiness. A simple fitting method was applied to the baseline cases, where best fit polynomials of C_T vs Reynolds number were developed at each Strouhal number. An iterative method was then used to estimate the effective Reynolds number of the unsteady flow cases, the results of which are shown in Fig. 5.13 (b). This process had little effect when converting lower Reynolds number cases, but significantly changed higher Reynolds number unsteady flow cases. For example, the effective Reynolds number shift for the unsteady flow case with a Reynolds number of 500 is was small. However, for the unsteady flow case with a Reynolds number of 7,000 the effective Reynolds number exceeds 30,000.

The correlation between the time-averaged thrust coefficient and the effective Reynolds number suggests that the effective velocity, U_e which is a nonlinear function of the nominal Reynolds number and Strouhal number, is larger than U_∞. This indicates that the extra kinetic energy in non-uniform flows can enhance thrust production. The time-averaged lift coefficient was observed to be somewhat random due to flow unsteadiness, but was approximately zero at all Reynolds numbers.

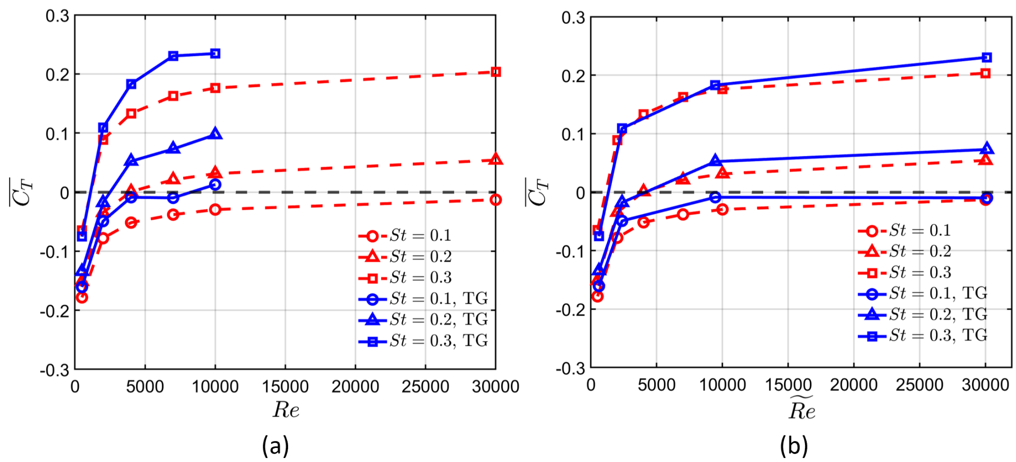

Figure 5.13: Time-averaged thrust coefficients over airfoil under non-uniform flow conditions at different St for different Reynolds numbers and comparison with the uniform flow conditions (a) function of Re and (b) function of effective Re.

5.2.2.3 Scaling laws

Senturk and Smits [123] derived a simple scaling law for a pitching airfoil following the work of Floryan *et al.* [130] under uniform flow conditions. The equation for the thrust coefficient derived by these studies is:

$$\overline{C_T} = \beta St^2 - C_D, \tag{5.1}$$

where β is an empirically derived coefficient, St is Strouhal number, and C_D is the offset drag term introduced previously by Floryan *et al.* [130]. It should be noted that Reynolds number effects were not considered in [130]. This offset drag term was considered as the equivalent fixed body drag of the pitching airfoil's projected frontal area. Later, Sentruk and Smits [123] validated the proposed definition of offset drag further by comparing the drag of a fixed NACA0012 airfoil at zero angle of attack to the offset drag of a pitching airfoil with $\theta_o = 8°$. They determined that both the static drag and the offset drag of the NACA0012 airfoil decrease with increasing Reynolds number. However, the static drag of NACA0012 is significantly less than the offset drag at any Reynolds number.

The values of C_D and β were calculated at each Reynolds number and Strouhal number combination for the uniform flow cases and plotted in Fig. 5.14. Figure 5.14 (a) shows that the time averaged thrust coefficients align linearly to the scaling parameters, further validating the work of [123]. Figure 5.14 (b) shows that the offset drag and β change as the Reynolds number increases. The dashed lines in Fig. 5.14 (b) were plotted using the equations for C_D (black dashed line) and β (blue dashed line) from [123]. Overall, the baseline uniform flow results aligned well with prior studies.

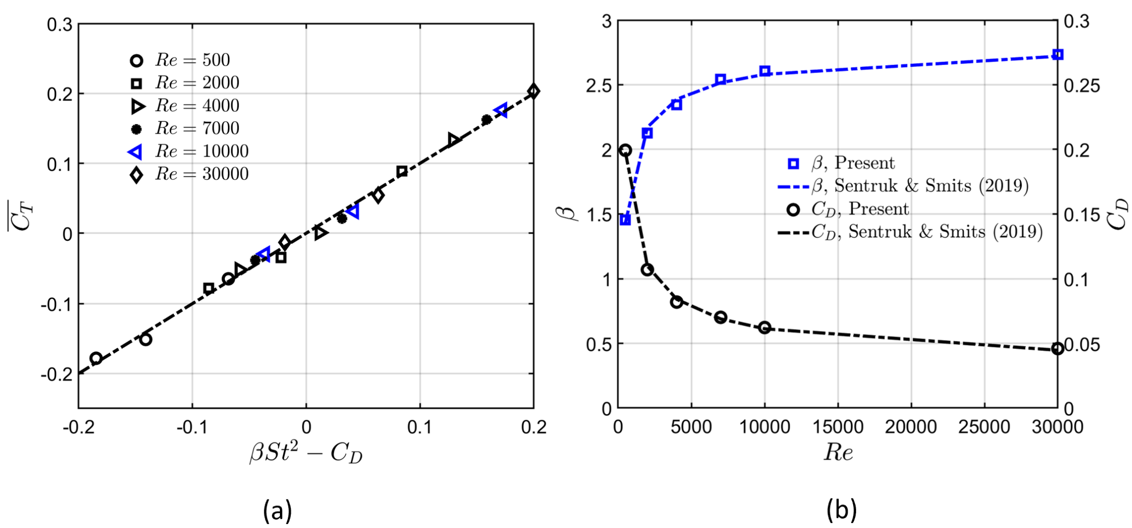

Figure 5.14: (a) Comparison with the scaling law at different St for different Reynolds numbers and (b) β and C_D as a function of Re under uniform flow conditions.

Extending this scaling law directly to the unsteady flow cases results results in an expected increase in the thrust coefficient. Figure 5.15 (a) shows the unsteady flow thrust coefficients in blue, with the blue dashed line representing the best-fit version of the scaling law developed by [123], which is plotted as a black dashed line. A clear shift between the scaling laws is present with the most obvious being a shift in ΔC_D. However, it should be noted that when β and C_D are evaluated using the effective Reynolds number, introduced in previous subsections, the thrust coefficient satisfies the original scaling law Eq. 5.1. However, the effective Reynolds number developed here cannot be used to predict thrust as it was calculated from the measured thrust coefficient (see Section 5.2.2.2). Thus, for predictive purposes, the scaling law should be built from easy-to-measure non-dimensional quantities, such as the Strouhal and Reynolds numbers in its original version.

To align the new unsteady flow data with the steady flow scaling law the offset drag C_D needs to be decreased. To accomplish this corrected C_D values at each Reynolds number were determined for unsteady flow conditions while holding β constant. Since Fig. 5.14 showed that C_D is a function of Reynolds number it therefor becomes logical to include the turbulence intensity (TI) was in the new definition of C_D for non-uniform flow conditions. Figure 5.15 (b) shows that C_D is also an approximately linear function of the turbulence intensity, which results in the new equation for the offset drag as:

$$C_D = -0.2725\ TI + 3.3198\ Re^{-0.5} + 0.0856 \tag{5.2}$$

Figure 5.16 (a) shows the implementation of Eq. 5.2 into the scaling law with both steady and unsteady flow conditions plotted. When applying the new

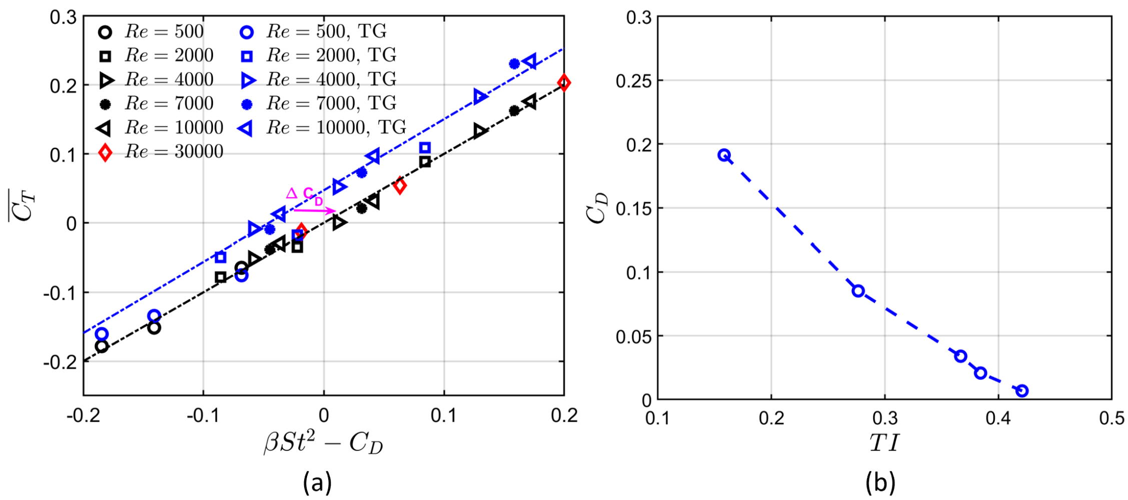

Figure 5.15: (a) Comparison with the scaling law under non-uniform flow conditions at different St for different Reynolds numbers and comparison with the uniform flow conditions and (b) C_D as the function of Turbulence Intensity.

formulation of C_D the data correlate well with data for uniform flow conditions and align well with the original model of Senturk and Smits' [123]. Figure 5.16 (b) shows the different β and C_D values as a function with Reynolds numbers. Note here that the offset drag terms vary significantly between the unsteady and baseline conditions. For uniform flow conditions the values of C_D closely aligned with Senturk and Smits' results [123]. However, for non-uniform flow conditions, the C_D followed a similar trend but with smaller values compared to the baseline flow. This trend is similar to the shift in Reynolds number observed previously in this study, which suggests that unsteadiness and Reynolds number have similar effects on the flow.

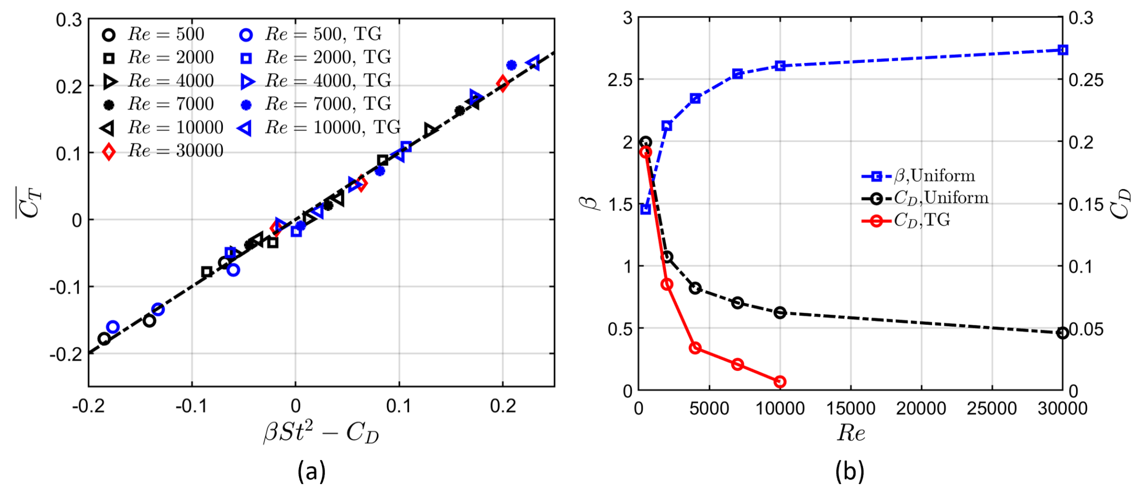

Figure 5.16: (a) Comparison with the scaling law under non-uniform flow conditions at different St for different Reynolds numbers with corrected C_D and (b) β and C_D as a function of Re and comparison with the uniform flow conditions.

5.3 Summary of Major Findings

This chapter investigated the effect of highly unsteady flow environments on an oscillating airfoil using an in-house high-order CFD solver. The key findings from the results presented in this chapter are as follows:

- The presence of an unsteady non-uniform incoming freestream flow enhanced the thrust production of an oscillating airfoil, when compared to steady freestream flow.

- The increase in average thrust coefficient was shown to be caused by constructive interaction of freestream vortex structures and the oscillating airfoil. Interactions that induce drag were also observed, but they were less common than events that increase thrust, resulting in a higher average thrust.

- Freestream unsteadiness altered the offset drag term (C_D) in the previously known scaling law, decreasing significantly in a way similar to increasing Reynolds number.

- A corrected C_D term was introduced into the scaling law, which includes Reynolds numbers, Strouhal numbers, and turbulence intensity for unsteady flow conditions. The results of this introduction aligned well with the uniform flow conditions.

Chapter 6: Effects of Unsteady Freestream on an Airfoil Performance at Low Reynolds Numbers

This chapter's primary objective is to compare two-dimensional (2D) and three-dimensional (3D) simulations of the stationary airfoil at low Reynolds numbers. The chapter will highlight key differences between 2D and 3D simulations, as well as the effect of small scale turbulence on the airfoil's performance in 3D. Computational studies of the response of a NACA0012 airfoil at varying angles of attack (α) to freestream turbulence at low Reynolds number (i.e., 12,000 based on the airfoil chord length) are conducted. Similar to the earlier study, the unsteady freestream is generated by placing an array of circular cylinders upstream of the airfoil. The presence of moderate freestream turbulence ($\sim 5\%$) affected the formation of laminar separation bubbles near the leading edge of the airfoil, which has significant impact on the aerodynamic performance. The study was able to recreate the maximum lift coefficient of the airfoil in unsteady freestream turbulence observed in experiments, which is higher than that for the airfoil in a uniform freestream. In general, the present numerical results agree reasonably well with those from experimental studies. This work also demonstrates that three-dimensional (3D) simulations with high-order accurate numerical methods predict the lift coefficient more accurately than lower dimension (i.e.,2D) or lower order 3D methods.

6.1 Computational Setup

Figure 6.1 shows the schematic of 2D computational domain used for the numerical study. The dimensions of the computational domain are loosely based on the wind tunnel test section of the experiment at the U.S. Army Research Lab (ARL). For these simulations a fixed inlet and outlet boundary were used. For the 2D simulations symmetry boundary conditions were used for the top and bottom. An array of cylinders was placed perpendicular to a uniform freestream to generate turbulence in a similar manner to the Medium Turbulence Generator (MTG) experiment. This is a simplified version of the grid turbulence used in separate experiment, which used a grid of cylinders. The ratio of distance between cylinders (L) to the cylinder diameter (d), i.e. L/d is 3. For the 3D simulation, the 2D grid was extruded to a distance $s/c = \pi d$ in the spanwise direction. The Reynolds number based on the diameter of cylinder is around 1,900 and the spanwise length equal to πd is sufficient to capture 3D effects [131]. The periodic boundary conditions on the top, bottom and spanwise direction were used in the 3D simulations. In order to investigate the effects of freestream turbulence on the performance of the NACA0012 airfoil a set of AoAs have been studied as shown in Table 6.1 for baseline and turbulence generator cases. 6.1 for baseline and turbulence generator cases.

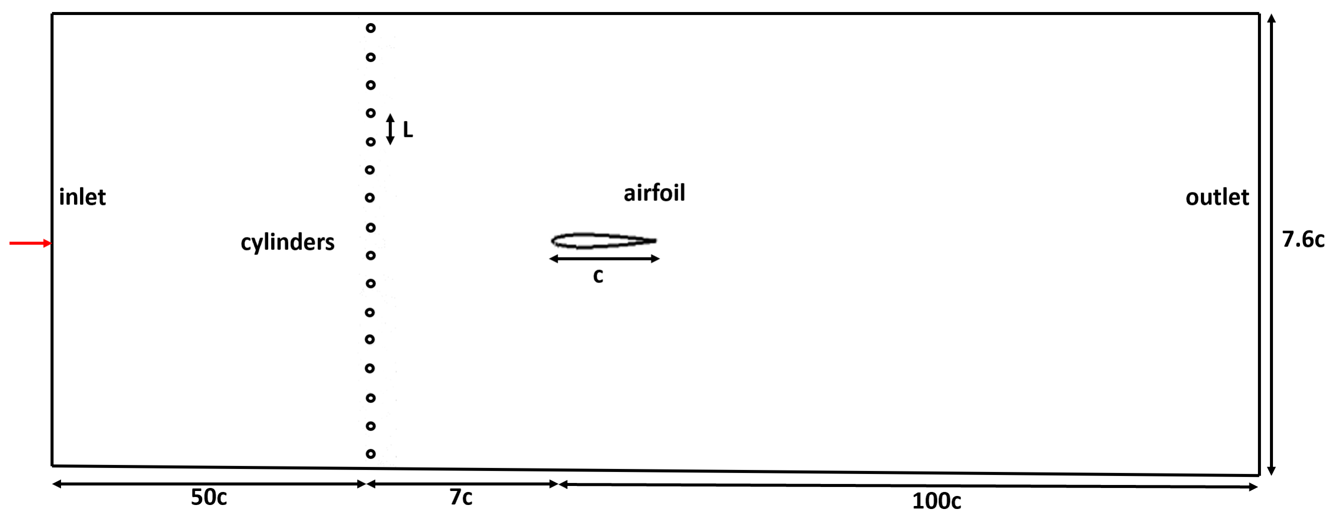

Figure 6.1: An illustration of the computational domain.

Baseline cases		Turbulence cases	
Cases	AoA	Cases	AoA
C1	8	C4	8
C2	10	C5	10
C3	12	C6	12

Table 6.1: Cases with baseline and turbulence generators with varying angle of attacks.

6.2 Results and Discussion

6.2.1 Characterization of Unsteadiness and Comparison with Experimental Results

First the flow field downstream of the cylinder array was characterized without the wing to evaluate the turbulence generated and compared with the experimental results. The vortices produced by the cylinders interact and mix with each other and, after a certain distance, a more homogenous field of turbulence is developed as shown in Figure 6.2 (a) and (b). In the 2D simulation, shown in Figure 6.2 (a), large scale vortices were observed near the wing location whereas in 3D simulation the vortices broke down into small eddies (see Figure 6.2 (b)). A numerical probe, equivalent to a hot-wire probe in experiments, was placed in the computational domain at the location where the wing was planned to be placed in later studies. The velocity power spectrum for 2D and 3D simulations were compared in Figure 6.2 (c). The power spectral density (PSD) of the velocity for 2D and 3D simulations show that the energy decay region of -3 and $-\frac{5}{3}$ respectively. The turbulence intensity at the probe location for 2D simulation was also found to be around 7 times larger than in the 3D simulation. The higher turbulence intensity in 2D simulation was due to larger vortex structures that could not break down as rapidly as they could in the 3D simulation. Figure 6.2 (d) shows the velocity power spectrum for 3D simulation compared with an experimental result obtained at ARL in the wind tunnel. The turbulence intensity for this case was around 5%, closely matching the experimental

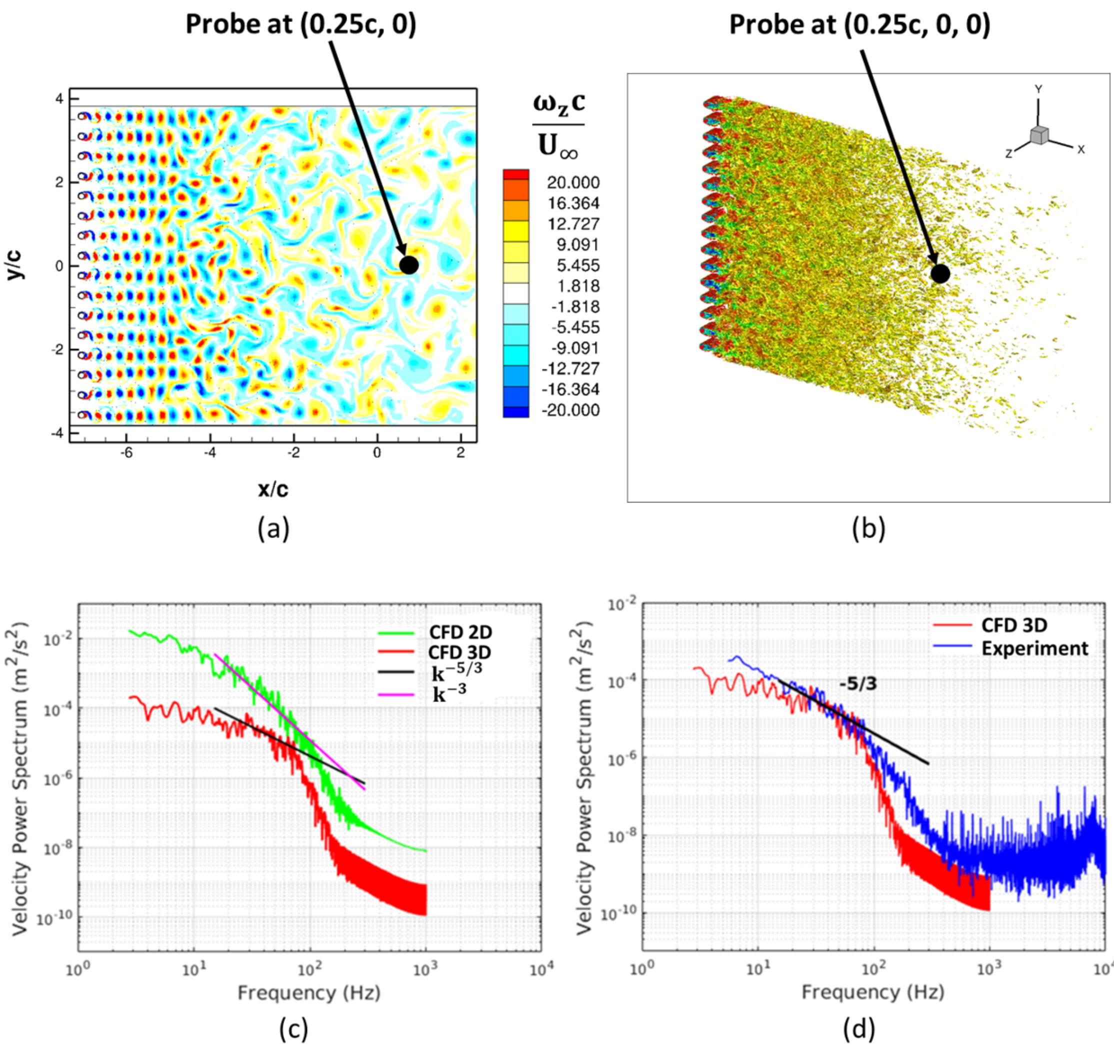

Figure 6.2: (a) 2D flow field in the downstream of an array of cylinders, (b) 3D flow field in the downstream of an array of cylinders, (c) Velocity Power Spectrum plot at the probe location for 2d and 3D results and (d) Velocity Power Spectrum plot at the probe location for 3D, and its comparison with the experimental results.

value of 4.8%. The power spectral density (PSD) analysis of the velocity shows the region of $-\frac{5}{3}$ energy decay for both computation and experiment, Figure 6.2 (d). The 2D and 3D characterization of the turbulence generator showed that the 3D simulation results closely matched with the experimental results. The results also showed that the 2D simulation produced a highly unsteady flow, but not one that reflects real-world turbulence.

6.2.2 Flow Field over a Stationary 2D Airfoil

After confirming that the parallel array of cylinders produced similar turbulence to that in experimental measurements, a NACA0012 airfoil was placed in the computational domain at seven chord lengths away from the turbulence generator. This was done to match the experimental configuration in the ARL wind tunnel. At first a 2D simulation was conducted with varying angles of attack (α) to observe the impacts of this level of turbulence on the airfoil. While it is known that 2D simulations do not generate true turbulence at a wide range of scales, this simulation allowed for the investigation of multiple factors not possible in experimental studies. First, it is unknown whether large or small scale structures are the cause of the performance changes observed experimentally. By using the 2D simulation only larger scale and more coherent structures would be generated. Secondly, if the 2D simulation was successful at modeling the aerodynamic performance it would allow for a fast method for calculating turbulence effects on airfoil performance. The vortices observed in the flow in the 2D simulations were, as expected, larger and the lack of breakdown into small structures was apparent, see Fig. 6.3. In this case it became apparent that the large-scale eddies were significantly impacting the airfoil and the 2D simulation was not likely to be successful at modeling turbulence effects.

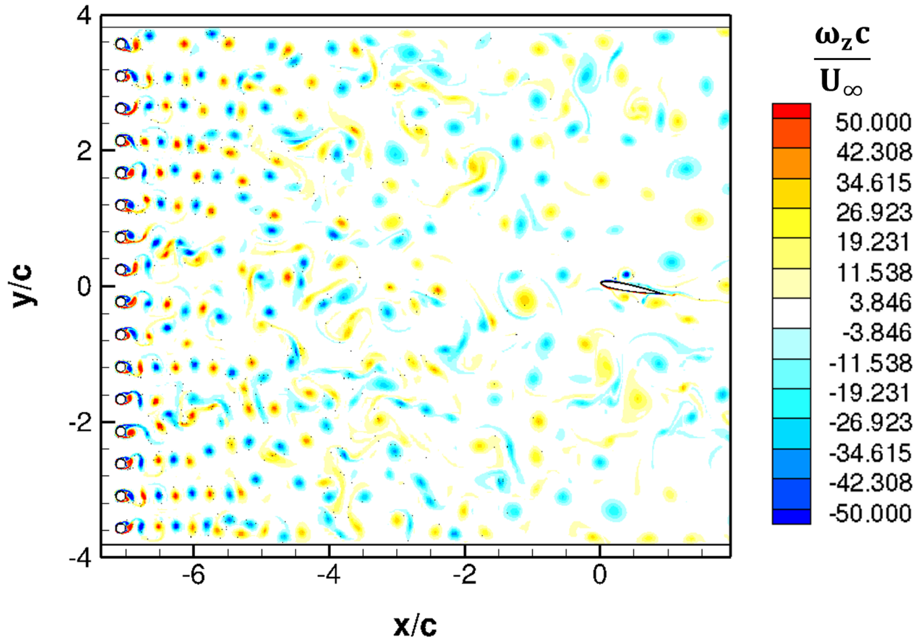

Figure 6.3: 2D Instantaneous Vorticity Field of a NACA0012 Airfoil at $\alpha = 10°$ and Re= 12,000 with the Turbulence Generator.

Figure 6.4 shows a close-up flow field around the NACA0012 airfoil at $\alpha = 10°$ with freestream turbulence present. The large vortex structures produced by the turbulence generator were observed randomly striking the airfoil, having a significant impact on the boundary layer and airfoil performance. Figures 6.4 (a-f) show the evolution of the flow over 30 non-dimensional times, during which many unsteady vortex-boundary layer interactions occurred. The formation of leading-edge vortices was random and dependent on the strength of the upstream vortices generated by the turbulence generator. This leading-edge vortex formation is somewhat similar to that observed on dynamic wings, but this effect is not observed in experimental studies, which had lower turbulence intensities.

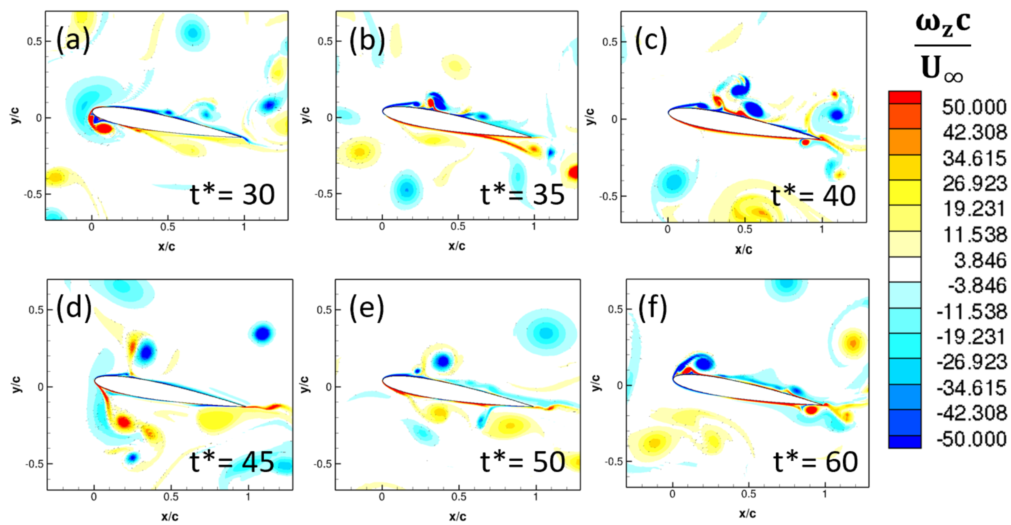

Figure 6.4: 2D Instantaneous Vorticity Fields on the NACA0012 at $\alpha = 10°$ and Re= 12,000 with the Turbulence Generator.

6.2.3 Flow Field over a Stationary 3D Wing

From the 2D simulation, the turbulence generator was not able to produce a uniform turbulence near the airfoil and boundary layer development was effectively random due to the strong vortex structures in the flow. These limitations of the 2D simulation suggested that a 3D simulation was needed to adequately model the airfoil performance. Partial 3D simulations, with a span of πd and periodic boundary conditions, produced a flow with nominally isotropic turbulence similar to that observed in experiment (see Figure 6.2). In order to study the impact of turbulence disturbance on the airfoil two cases were simulated with a 3D domain. A baseline NACA0012 in clean flow and with the Turbulence Generator (TG) were simulated to compare the effects of freestream turbulence on the stationary wing at the different angle of attack (α). The configuration of the TG was the same as for the 2D case, which is based off experiments at ARL and had a turbulence intensity of about 5%.

Figure 6.5 shows the flow field results of the 3D simulation for the airfoil at $\alpha = 10°$, with Fig. 6.5 (a) showing a 2D instantaneous vorticity and Fig. 6.5 (b) showing a 3D view of Q-Criterion. Results of the 3D simulation showed that vortices from the upstream turbulence generator were fundamentally different from those in the 2D simulations. The eddies in the region near the wing were generally more uniform in this case. The vortex stretching allowed by 3D simulations was shown to be necessary for the large vortices shed from the TG to break down into smaller scale turbulence. This effect more closely matched real-world turbulent breakdown as shown in Fig. 6.2 (c).

The boundary layer formation on the NACA0012 wing at $\alpha = 10°$ due to the turbulence generator was significantly different compared to the baseline case. Figure 6.6 shows a close up view of the flow around the airfoil with and without freestream turbulence. In Figure 6.6 (a, c) a 2D instantaneous vorticity is shown with the corresponding iso-surface of the Q-criterion in Fig. 6.6 (b, d). At $\alpha = 10°$ on the baseline airfoil there was a clear flow separation and the airfoil was stalled. Conversely, for the same airfoil in turbulence the flow remained generally attached. The boundary layer was also notably different for the airfoil in turbulence

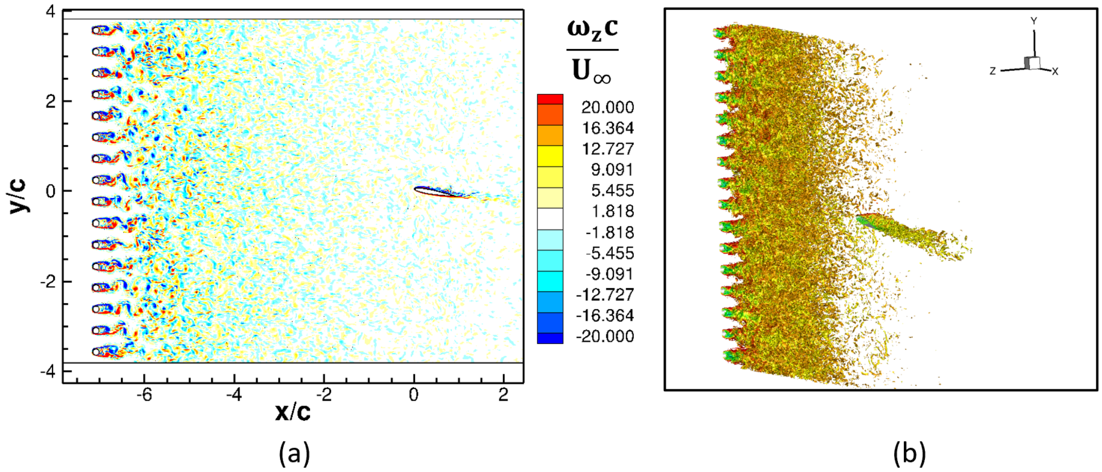

Figure 6.5: (a) A 2D view of the Instantaneous Vorticity Field and (b) the Iso-surface of Q colored by the streamwise velocity for the 3D simulation at $\alpha = 10°$ and Re= 12,000 with the Turbulence Generator.

when compared with the baseline. While the baseline airfoil at this angle was clearly stalled, the presence of turbulence reattached the flow and the airfoil was not in a stalled state. These results indicate that the stall angle of the airfoil was extended by turbulence, as previously reported by [94, 96–98]. The spanwise instantaneous vorticity fields on the surface of the NACA0012 airfoil are shown in Figures 6.7 (a) and (b) for the baseline and turbulence generator cases, respectively. The flow near the leading edge is two-dimensional in the baseline case at 8° AoA, with relatively insignificant spanwise variations (see Figure 6.7 (a)). However, due to the breakdown of the leading edge vortex in the turbulence case at 8°, there are spanwise instabilities near the leading edge of the airfoil (see Figure 6.7 (b)).

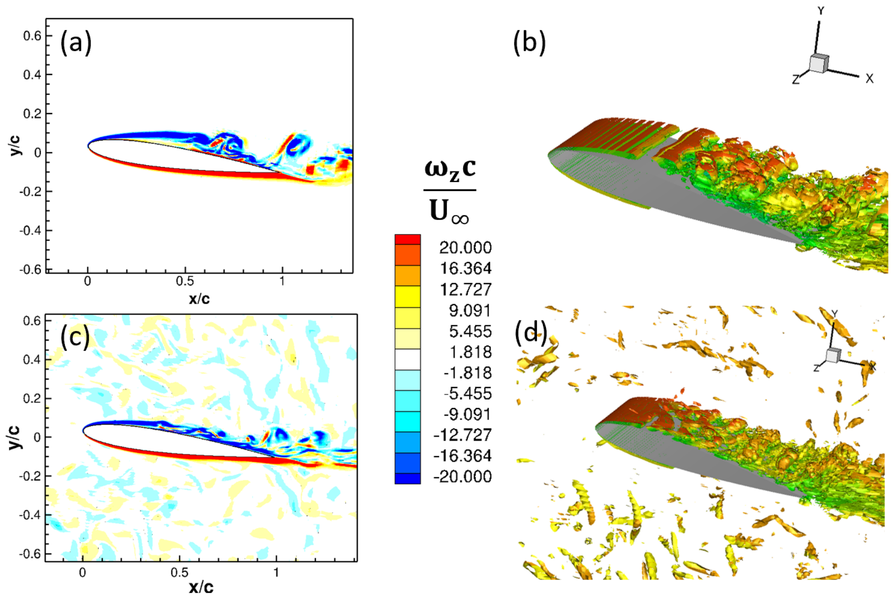

Figure 6.6: (a) A 2D view of $\alpha = 8°$ wing with no TG, and (b) the corresponding iso-surface of Q colored by the streamwise velocity for 3D simulation at $\alpha = 8°$ without TG. (c) A 2D view of $\alpha = 8°$ wing with a MTG, and (d) the corresponding iso-surface of Q colored by the streamwise velocity for 3D simulation at $\alpha = 8°$ with a MTG.

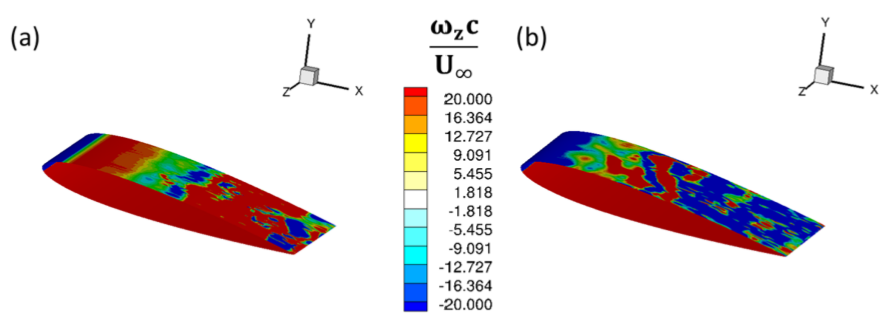

Figure 6.7: Instantaneous Vorticity Fields on the surface of NACA0012 at $\alpha = 8°$ and Re 12,000 (a) without Turbulence Generator and (b)with the Turbulence Generator.

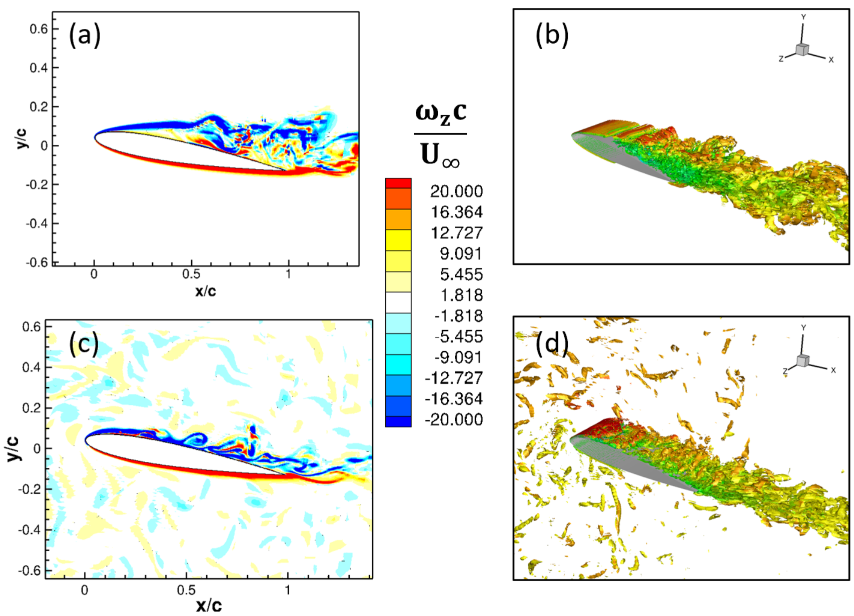

Figure 6.8: (a) A 2D view of $\alpha = 10^\circ$ wing with no TG, and (b) the corresponding iso-surface of Q colored by the streamwise velocity for 3D simulation at $\alpha = 10^\circ$ without TG. (c) A 2D view of $\alpha = 10^\circ$ wing with a MTG, and (d) the corresponding iso-surface of Q colored by the streamwise velocity for 3D simulation at $\alpha = 10^\circ$ with a MTG.

6.2.4 Time-Averaged Flows around a Stationary 3D Wing and Comparison with Experimental Results

In order to compare the 3D numerical simulation results with the experimental results from ARL's wind tunnel, a comparison of the time-average flow fields is done. For comparison purpose, the results for 8° and 12° AoAs, with and without the turbulence generator are presented. The time-averaged vorticity fields over the NACA0012 airfoil for 8° AoA are depicted in Figures 6.9 (a) and (b) for the baseline case without turbulence generator from CFD and experiment respectively. Figures 6.9 (c) and (d) illustrate the case with a turbulence generator for the NACA0012 airfoil at 8° AoA from CFD and experiment, respectively.

For both the baseline and turbulence generator cases, the CFD results closely matched the experimental results. The time-average flow fields shown in Figure 6.9 show that without turbulence, the airflow separated from the top surface of the airfoil. However, when turbulence was introduced the flow remained attached over the airfoil in the presence of turbulence.

Figure 6.10 illustrates the velocity profiles on the top surface of the airfoil at various chordwise locations, for both the baseline and turbulence cases at an angle of attack of 8°. The data shows that the flow remains attached near the leading edge for both freestream flow conditions. On the baseline airfoil the flow near the wing slows and eventually reverses direction, coinciding with flow separation and stall. However, the case with turbulence shows that flow reversal is inhibited. Instead, a typical turbulent boundary layer profile was observed.

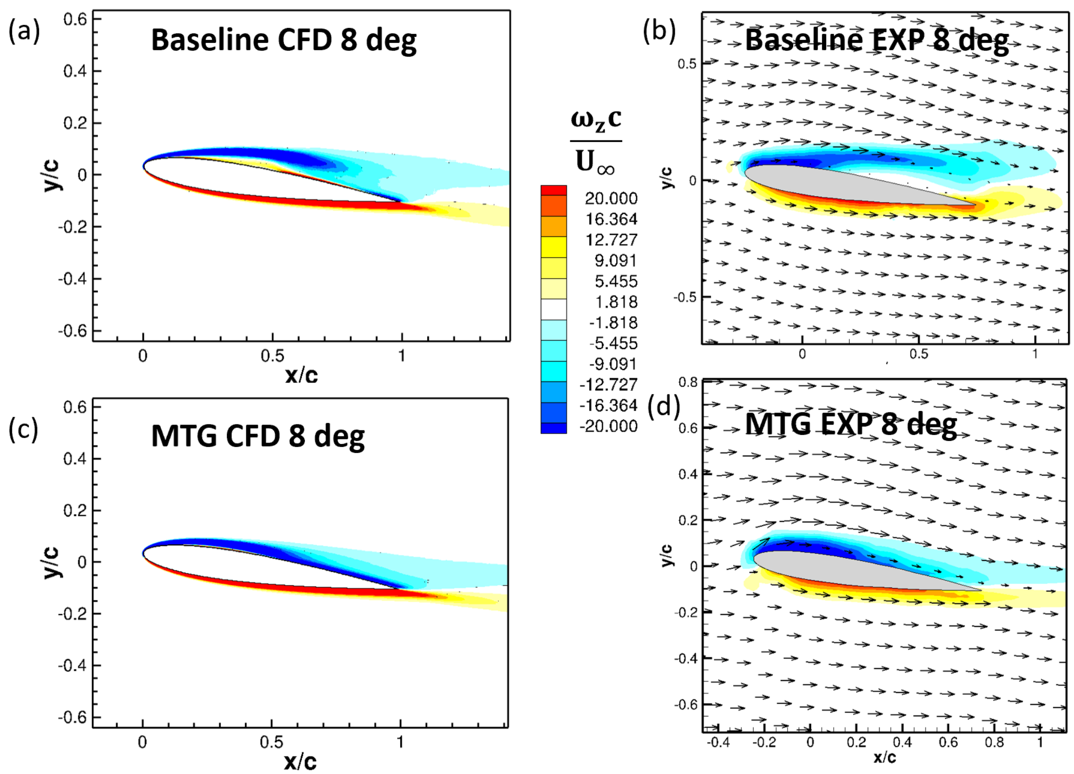

Figure 6.9: Time Average Flow Fields of NACA0012 airfoil at $\alpha = 8^{\circ}$ wing (a) Simulation Result with no TG, and (b) Experimental Result without TG. (c) Simulation Result with a MTG, and (d) Experimental Result with a MTG.

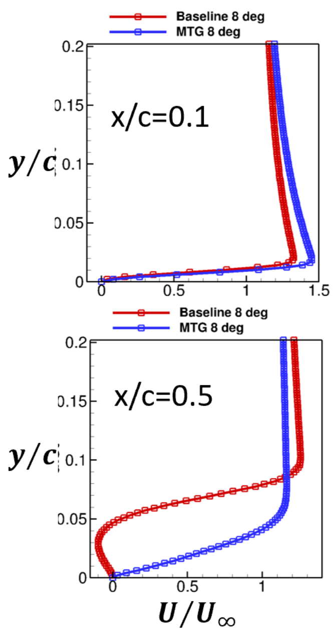

Figure 6.10: Velocity Profile of NACA0012 airfoil at $\alpha = 8°$.

A similar comparison was made in the post-stall region, where both the baseline and turbulence cases were stalled in the experiments. Figure 6.11 shows time-averaged vorticity flow fields for 12° AoA from the CFD and experiment. While the flow fields from the CFD and experiment appear to be similar in the baseline case (see Figure 6.11 (a) and (b)), the flow fields from the turbulence generator case do not match as well (see Figure 6.11 (c) and (d)). Both CFD and experimental results show a separated flow, the vorticity distribution near the leading edge was notably different and the CFD flow fields suggest that flow is attached near the training edge. In this case, the CFD model predicted that the wing was not stalled while it was in the experiments. The underlying physics of this are not well understood, but could be due to the slight differences in turbulence intensity, noise in experimental results, or even physical roughness in the experimental model not present in the

CFD simulation.

As before, Figure 6.12 shows the velocity profiles extracted from the CFD results on the top surface of the NACA0012 airfoil at selected chordwise locations. At $x/c = 0.1$ to $x/c = 0.3$, the velocity profiles for the turbulence generator case show reverse flow is present, but it was somewhat smaller than the baseline case. After $x/c = 0.4$, the flow reattaches when turbulence was present and the reverse velocity profile diminished. This indicates that flow is still attached near the trailing edge of the airfoil and stall had not yet occurred. These results confirm that the static stall angle was increased due to the presence of turbulence. However, the differences between the simulation and experiments suggest that other factors may limit the increase in static stall angle in the real world.

Further analysis of these differences was done by calculating the pressure coefficient and skin friction coefficient over the surface of the airfoil. These properties were calculated for the baseline and turbulence generator cases at 8° and 12° to evaluate the effect of background turbulence on these properties.

The surface pressure and skin friction coefficients are defined as:

$$C_P = \frac{P - P_\infty}{\frac{1}{2}\rho {U_\infty}^2} \tag{6.1}$$

$$C_f = \frac{\tau_w}{\frac{1}{2}\rho {U_\infty}^2} \tag{6.2}$$

where τ_w is the wall friction.

Figure 6.13 shows the resulting the time-averaged surface pressure coefficient over the airfoil. A typical lift-generating airfoil creates that lift by generating a high negative pressure near the leading edge. This type of profile is represented

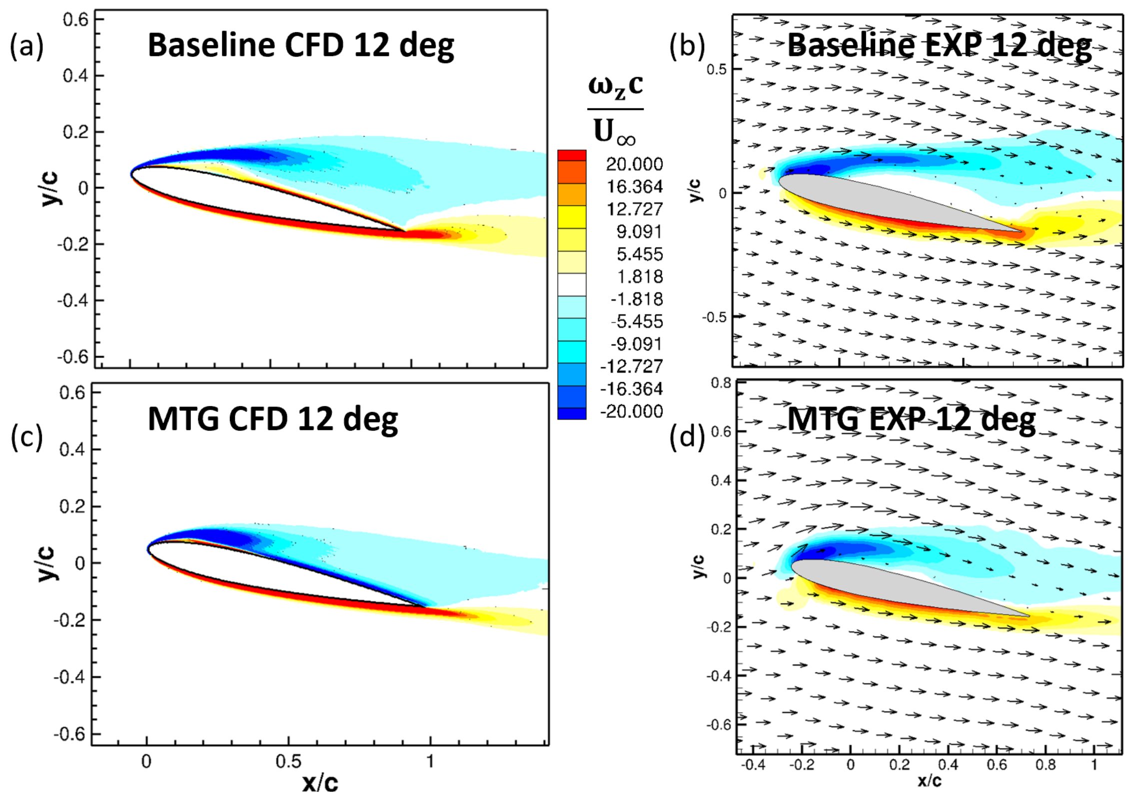

Figure 6.11: Time Average Flow Fields of NACA0012 airfoil at $\alpha = 12^\circ$ wing (a) Simulation Result with no TG, and (b) Experimental Result without TG. (c) Simulation Result with a MTG, and (d) Experimental Result with a MTG.

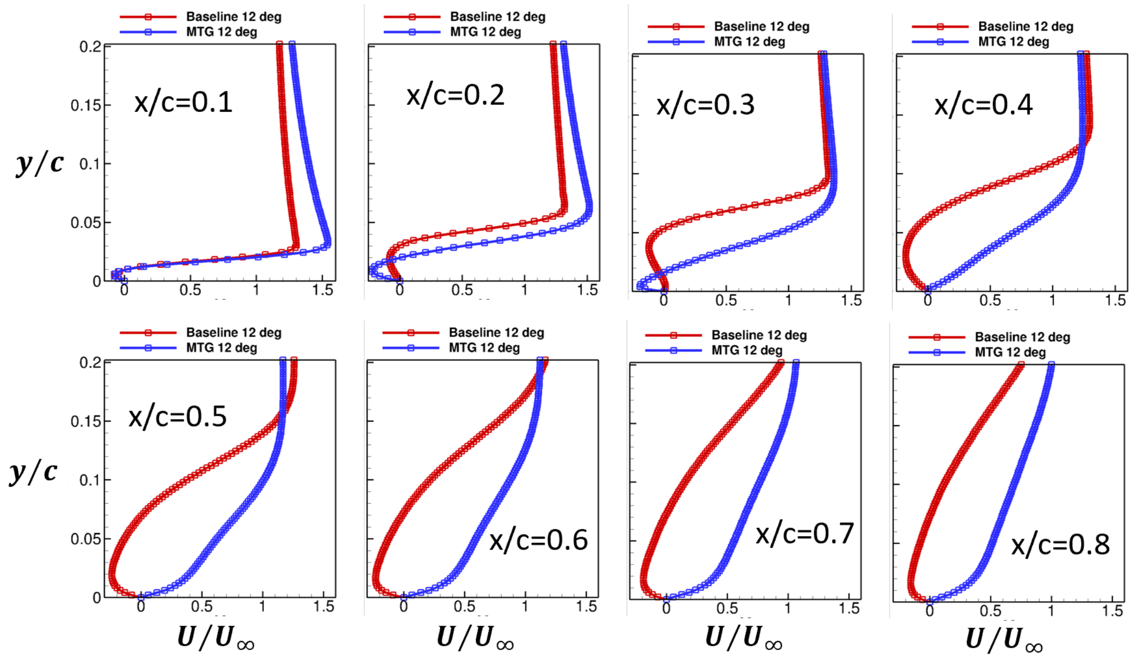

Figure 6.12: Velocity Profile of NACA0012 airfoil at $\alpha = 12°$.

best by the 8 ° case with turbulence (Fig. 6.13 blue). Conversely, for the baseline cases at 8° and 12°, flow separation had occurred which significantly decreased the negative pressure peak. When turbulence was added to the airfoil at 12° there was an additional plateau in pressure coefficient near x/c = 0.2. This type of plateau is indicative of a laminar separation bubble forming on the airfoil, despite the presence of turbulence. This is the likely source of the discrepancy between the experiments and CFD results, but the exact driver of this difference is still not well understood.

Analysis of the skin friction coefficient was done to further investigate the underlying reasons for the differences between the CFD results and experimental data. Figure 6.14(a) and (b) show the skin friction coefficients for baseline and turbulence cases at 8° and 12° angles of attack, respectively. Background turbulence has an effect on skin friction coefficients in both cases $\alpha = 8°$ and $\alpha = 12°$ due to the interaction of background turbulence with the airfoil's boundary layer. The laminar separation bubble observed in the pressure coefficient is also observed here at the higher angle, Fig. 6.14(b), where an change in surface skin friction was observed for x/c = 0.2-0.4. As stated in [132], increased Reynolds numbers result in earlier transition and reattachment, which contributes to an overall decrease in separation bubble length. Similar effects were observed in this study when background turbulence was present. This result strongly suggests that the presence of turbulence acts similarly to increasing Reynolds number.

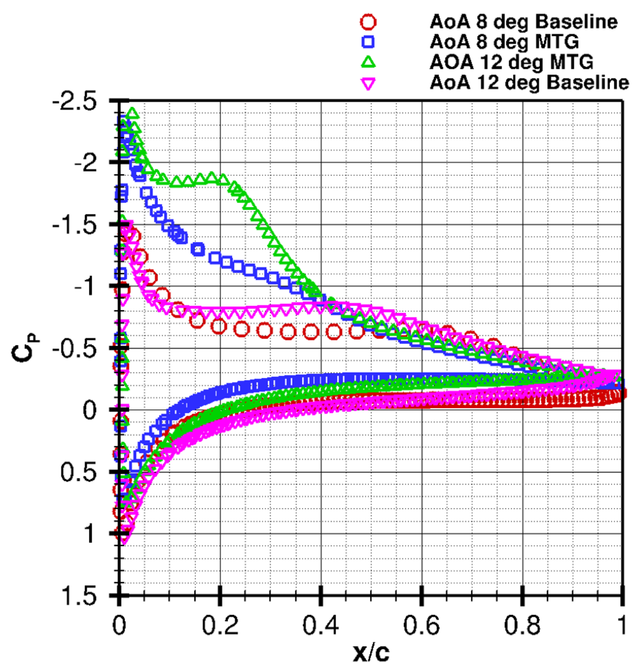

Figure 6.13: Time average surface pressure coefficients over NACA0012 airfoil at $\alpha = 8°$ and $\alpha = 12°$ wing with no TG and comparison with a MTG cases.

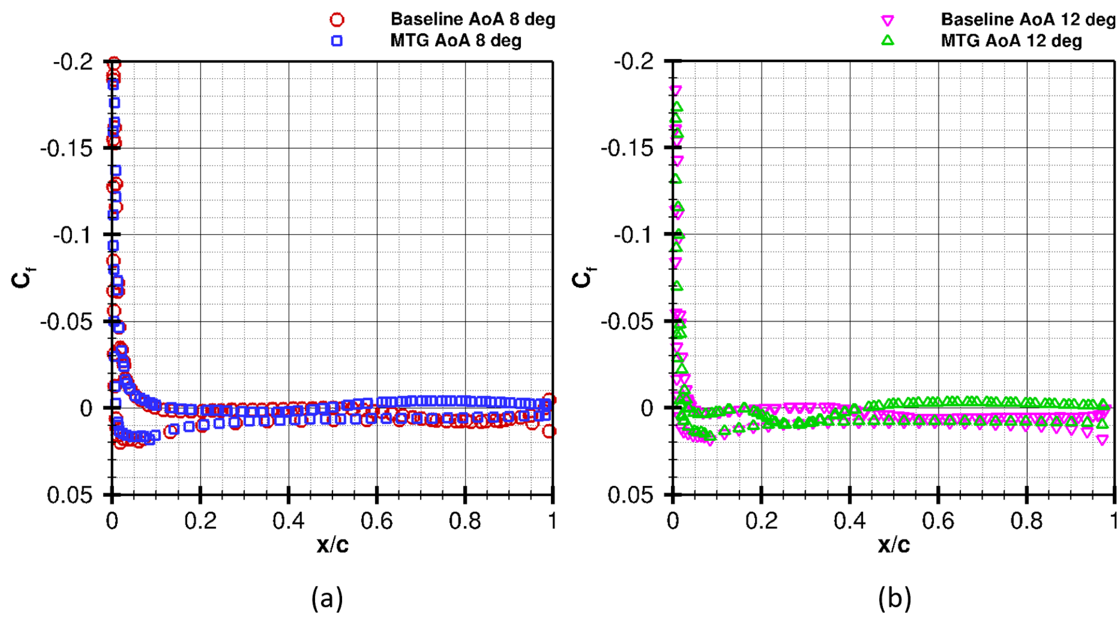

Figure 6.14: Time-average surface skin friction coefficients over NACA0012 airfoil at (a) $\alpha = 8°$ and (b) $\alpha = 12°$ wing with no TG and comparison with a MTG cases.

6.2.5 Aerodynamic Force Analysis of Stationary 2D and 3D Airfoils

To further compare the effectiveness of 2D and 3D simulations for the modeling to airfoil performance in turbulence, a comparison of the lift performance was also done. Figure 6.15 shows the lift coefficient histories over the time for 2D and 3D simulations with turbulence present. In the 2D simulation large fluctuations in the force history was observed. The obvious reason for these large spikes in the lift in the 2D simulation was due to the interaction between large-scale vortices and the airfoil. However, because the 3D simulation allowed for large shed vortices to break down into small-scale eddies fluctuation of the lift was far less severe. These small scale vortices did however have a significant impact on the flow separation as seen in Fig. 6.6, which in turn had a large impact on the lift coefficient and stall angle. Interestingly, the time-averaged lift coefficients for the two cases were strikingly similar to each other, with the 2D simulation resulting in $C_L = 0.72$ and the 3D simulation resulting in $C_L = 0.77$. This result suggests that great care must be taken when modeling turbulent flows at low Reynolds numbers, as mean values may be similar but with strikingly different flow fields.

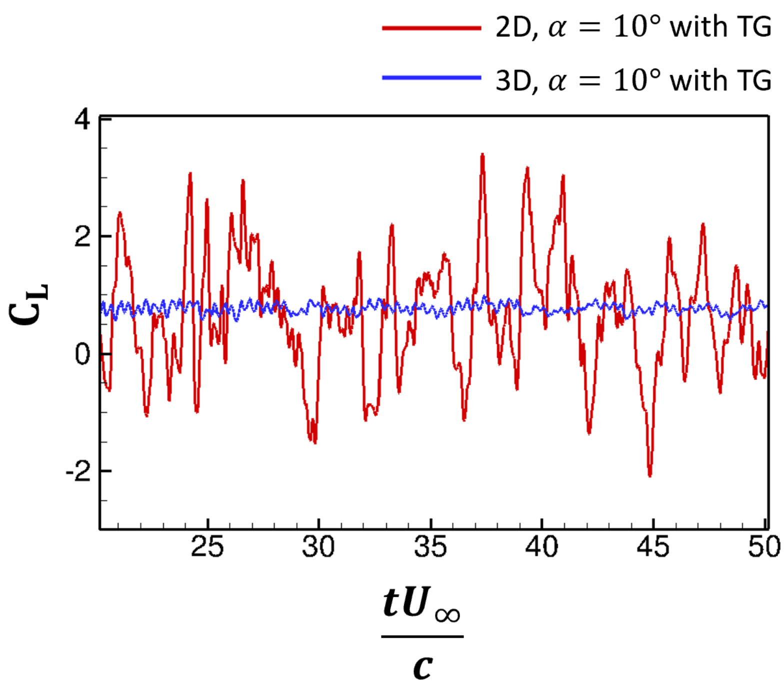

Figure 6.15: Lift coefficient histories for the 2D and 3D cases with the MTG for NACA0012 at at $\alpha = 10°$ and Re = 12,000.

Further analysis was done comparing the lift calculations at a wider range of angles of attack. Figure 6.16 shows the experimental and computational comparison of the time-averaged lift coefficients, as a function of angles of attack (α), for the baseline and turbulence generator cases. A preliminary 3D model using only 2^{nd} order spatial and temporal schemes was evaluated and had poor performance modeling the lift of the baseline wing. It followed the baseline experimental data at low angles but deviated significantly at higher angles. Due to computational run time, a time-averaged lift coefficient for the 3D case for only $\alpha = 10°$ with the 3rd order spatial and 4^{th} order temporal schemes was conducted. These results agreed well with the experimental results with only a small discrepancy for the case with the MTG. It should be noted that the simulation agrees quite well with $\alpha = 9.5°$ and $\alpha = 10.5°$ and that experimental uncertainty at $\alpha = 10°$ may explain this discrepancy. At $\alpha = 10°$ the lift coefficient was higher when turbulence was present for both the simulation and experiment. The lift results from 2D simulations with the turbulence generator did not agree particularly well with the experimental results. However, these results may superficially appear to be accurate if care isn't taken to compare to comparable experiments. More investigations are needed to answer the question to what extent 2D simulations could reliably predict airfoil performance in unsteady freestream flows.

6.3 Summary of Major Findings

This chapter detailed an investigation of freestream turbulence with a static NACA 0012 airfoil at low Reynolds number of 12,000. Results of 2D and 3D simulations were compared with the experimental results. A summary of key findings from this chapter are summarized below.

- A turbulence generation mechanism was developed that appropriately reproduced grid turbulence. The turbulence generated in 3D simulations was found to closely match wind tunnel turbulence statistics.

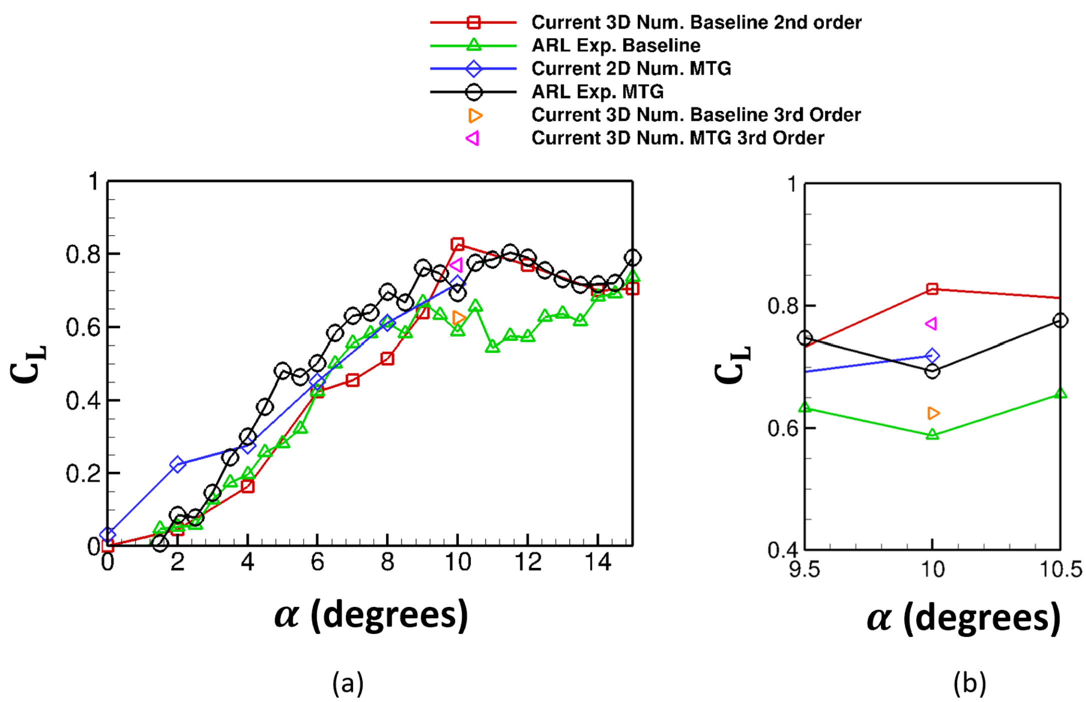

Figure 6.16: (a) The Time-averaged lift coefficients as a function of α for Re=12,000 and (b) Close view of average lift coefficient around 10 degrees.

- Due to a lack of vortex stretching, 2D simulations were ineffective at reproducing experimental turbulence. As a result, the flow had a slower vortex breakdown and larger scale vortices. Large-scale vortices dominated airfoil performance, resulting in greater force fluctuation on the airfoil but statistically similar lift to higher fidelity simulations.

- In general, the flow remained attached on the suction side of the airfoil at high angles of attack when turbulence was present. At similar angles the airfoil was stalled in a uniform freestream. The lift coefficient was also higher in the presence of turbulence.

- The 3D simulations closely matched experimental wind tunnel results, but some discrepancies were observed at higher angles of attack.

- The presence of background turbulence was found to have similar effects to increasing Reynolds numbers in this study.

Chapter 7: Conclusions and Future Work Recommendations

This thesis explores the flow physics of stationary and flapping wings in highly unsteady environments. The ultimate goal was to understand how wings behave at low Reynolds numbers in highly unsteady environments, such as vertical gusts and unsteady freestream conditions, and to identify critical flow structures that contribute to airfoil performance. The following sections summarize the research reported in the previous chapters, as well as key observations and conclusions about the interaction of a static and oscillating NACA0012 airfoil with a vertical gust and unsteady freestream environments.

7.1 Summary of Research and Conclusions

The first part of this thesis presented a numerical investigation of gust-wing interaction at low Reynolds numbers using advanced high-order CFD methods. The work identified key dynamics that provide clues to multiple gust mitigation strategies. For a stationary airfoil the gust caused an increase in lift followed by a highly unsteady stall process. A pitch-down maneuver was demonstrated as an effective method of responding to the gust and it was also observed that the effects of the gust can be mitigated with a simple pitch response maneuver. A larger change in pitch angle was observed to cause negative lift with a high potential to overshoot into a negative angle stall state. A step-wise pitch-down approach was demonstrated as an effective method for maintaining steady lift even when the AoA generated by the gust continued to grow.

A gust mitigation strategy using oscillating airfoils was also demonstrated. The influence of reduced frequency and Strouhal number were evaluated and showed that oscillating the airfoil had several different effects. At low reduced frequencies the gust continues to dominate the flow field and force coefficients, generating highly unsteady noise on top of the typically sinusoidal lift curves generated by pitching airfoils. Pitching at higher reduced frequencies overcomes the flow disturbances caused by the vertical gust. However, the gust significantly increased both the lift and thrust generated by the oscillatory motion, with the average lift shifting above the static stall lift. A relative fluctuation metric along with power consumption were used to evaluate the effectiveness of the gust mitigation strategy. The optimal reduced frequency using these metrics was $k = 2.86$ which had a low relative fluctuation with the lowest power consumption. Results also showed that the Stouhal number was not a dominant factor when attempting to mitigate a vertical gust. At the optimal reduced frequency the Strouhal number, as varied by controlling oscillating amplitude, had little effect on the relative fluctuation and suggests that even small amplitude oscillations can be used to mitigate gusts.

The second part of this thesis documents the influence of unsteady flow environments on an oscillating airfoil.Steady and unsteady incoming flow conditions were compared and the flow physics of the thrust enhancement mechanisms of unsteady environments was explored. The unsteady flow environment served to alter oscillating wing performance in two key ways: altering the effective Reynolds number and shifting the value of the offset drag term C_D. The unsteadiness in the flow caused an increase in thrust generation at lower Reynolds numbers, which caused low Reynolds number oscillating airfoils in unsteady flow to behavior similar to higher Reynolds number cases in steady environments. A simple fit-based correction method showed that an effective Reynolds number can be used to model the shift caused by the unsteady freestream.

The underlying flow physics showed that unsteadiness in the freestream expectedly generated variations in the sinusoidal thrust data. This unsteadiness was directly related to the large, coherent incoming flow structures. The increase in average thrust coefficient was shown to be caused by constructive interaction of freestream vortex structures and the oscillating airfoil. Drag inducing interactions were also observed but were less common than thrust increasing events, resulting in a higher average thrust. An extension to the thrust model proposed by Senturk and Smits' [123] was developed to incorporate the effects of unsteady flow environments. An increase in thrust production was incorporated into the offset drag term of the scaling law. A linear relationship between the turbulence intensity and offset drag was demonstrated to accurately thrust produced in unsteady flow environments back onto the scaling law.

The final part of this thesis examined the impact of an unsteady freestream on the performance of the static NACA0012 airfoil using two-dimensional (2D) and three-dimensional (3D) simulations. A turbulence generation mechanism was developed that adequately reproduced grid turbulence when compared with wind tunnel experiments. The turbulence generated in 3D simulations were shown to closely match turbulence statistics from wind tunnel experiments. Separate 2D simulations were ineffective at reproducing experimental turbulence due to lack of vortex stretching. This resulted in slower vortex breakdown and larger scale vortices in the flow. The large-scale vortices dominated airfoil performance, producing a larger force fluctuation on the airfoil, but with similar average lift as higher fidelity simulations. The 3D simulations allowed for faster turbulent breakdown of large scale structures in the flow, more closely resembling real-world turbulence. The small-scale structures did not generate large force fluctuation, but did significantly alter boundary layer evolution. The background turbulence from the turbulence generator caused the flow to remain attached on the suction side of the airfoil at high angles of attack, while at the similar angles this same airfoil in a uniform freestream was stalled. Due to this the lift coefficient was also higher with turbulence compared to the uniform freestream case.

The 3D simulation results agree reasonably well with the experimental results for both baseline and turbulence generator cases, with some discrepancies at higher angles of attack. Additionally, these results demonstrate that in the presence of background turbulence, high Reynolds number features similar to those observed in chapter 5 for 2D oscillating airfoils are observed.

To summarize, the thesis's key conclusions clearly demonstrate that unsteadiness caused by vertical gusts and freestream turbulence can profoundly modify the aerodynamic performance of an airfoil at low Reynolds numbers. These findings will potentially help improve design and control of future unconventional UAVs by revealing unsteady aerodynamics in highly unstructured real-world flow environments.

7.1.1 Original Contributions

This subsection highlights for the reader new contributions of this work to the field. These contributions are briefly described below:

1. This work reports for the first time that an oscillating wing with a high reduced frequency can effectively mitigate the detrimental effects of gusts, resulting in a predictable oscillatory lift and drag/thrust behavior. This effect was shown to be dominated by the reduced frequency, and is relatively insensitive to varying the Strouhal number. These results suggest there may be effective gust mitigation strategies leveraging oscillating wing behaviors on MAVs.

2. This study documents the impact of unsteady flow environments on the propulsive performance of a pitching NACA0012 airfoil and identifies key flow dynamics in the unsteady environment that can enhance pitching airfoil thrust production. By incorporating a turbulence intensity correction into the original scaling laws, the author successfully extends Sentruk and Smits' [123] recent work on scaling laws of the propulsive performance of a pitching airfoil under uniform upstream flow conditions to those applicable in highly unsteady flow environments.

3. The required model fidelity for accurately representing turbulence in CFD at low Reynolds number was demonstrated. Both 2D and 3D simulations

were evaluated along with comparisons to experimental results. The results of the study showed that higher-order 3D simulations are required to accurately model the effects of turbulence on airfoil performance at low Reynolds numbers.

7.2 Future Works

The current research demonstrated the mitigation of gusts by generating large-scale unsteady features around the airfoil. However, the underlying flow physics generating these structures, such as that from the nonlinear vortex interaction at different spatiotemporal scales, is beyond the scope of this study and is left for discussion in future work on this topic.

For data-driven control algorithms, current research on gust mitigation measures provides a framework. Furthermore, the robust gust mitigation with data driven control algorithm should be connected with the fluid solver in order to implement the effective control mechanism for gust mitigation.

The scientific community can benefit from an extension of the current work into fully 3D gust studies and 3D oscillating wings in turbulence environments, specifically to learn more about the effects of three-dimensionality on motions in unsteady environments. Chapter 6 showed that the 3D analysis of stationary wings in turbulence situations has considerable impacts, and suggests that many future studies should focus on this type of simulation. However, in order to properly comprehend the vast spectrum of affects on both large and small scale eddies, it is necessary to investigate how these small scale turbulence eddies may impact for the unsteady motions in complex, dynamic and chaotic environments.

Bibliography

[1] G. Jones, M. Santer, M. Debiasi, and G. Papadakis, "Control of flow separation around an airfoil at low reynolds numbers using periodic surface morphing," *Journal of Fluids and Structures*, vol. 76, pp. 536–557, 2018.

[2] L. Petricca, P. Ohlckers, and C. Grinde, "Micro-and nano-air vehicles: State of the art," *International journal of aerospace engineering*, vol. 2011, 2011.

[3] W. Shyy, H. Aono, S. K. Chimakurthi, P. Trizila, C.-K. Kang, C. E. Cesnik, and H. Liu, "Recent progress in flapping wing aerodynamics and aeroelasticity," *Progress in Aerospace Sciences*, vol. 46, no. 7, pp. 284–327, 2010.

[4] M. F. Platzer, K. D. Jones, J. Young, and J. C. Lai, "Flapping wing aerodynamics: progress and challenges," *AIAA journal*, vol. 46, no. 9, pp. 2136–2149, 2008.

[5] D. G. Bohl and M. M. Koochesfahani, "Mtv measurements of the vortical field in the wake of an airfoil oscillating at high reduced frequency," *Journal of Fluid Mechanics*, vol. 620, pp. 63–88, 2009.

[6] M. R. Visbal, R. E. Gordnier, and M. C. Galbraith, "High-fidelity simulations of moving and flexible airfoils at low reynolds numbers," in *Animal Locomotion*, pp. 341–360, Springer, 2010.

[7] M. Ashraf, J. Young, and J. Lai, "Reynolds number, thickness and camber effects on flapping airfoil propulsion," *Journal of Fluids and structures*, vol. 27, no. 2, pp. 145–160, 2011.

[8] A. Mackowski and C. Williamson, "Direct measurement of thrust and efficiency of an airfoil undergoing pure pitching," *Journal of Fluid Mechanics*, vol. 765, pp. 524–543, 2015.

[9] P. Lissaman, "Low-reynolds-number airfoils," *Annual review of fluid mechanics*, vol. 15, no. 1, pp. 223–239, 1983.

[10] S. Watkins, J. Milbank, B. J. Loxton, and W. H. Melbourne, "Atmospheric winds and their implications for microair vehicles," *AIAA journal*, vol. 44, no. 11, pp. 2591–2600, 2006.

[11] T. J. Mueller, "The influence of laminar separation and transition on low reynolds number airfoil hysteresis," *Journal of Aircraft*, vol. 22, no. 9, pp. 763–770, 1985.

[12] M. O'meara and T. J. Mueller, "Laminar separation bubble characteristics on an airfoil at low reynolds numbers," *AIAA journal*, vol. 25, no. 8, pp. 1033–1041, 1987.

[13] T. N. Pornsin-Sirirak, Y. Tai, H. Nassef, and C. Ho, "Titanium-alloy mems wing technology for a micro aerial vehicle application," *Sensors and Actuators A: Physical*, vol. 89, no. 1-2, pp. 95–103, 2001.

[14] P. Donely, "Summary of information relating to gust loads on airplanes," tech. rep., NASA, 1949.

[15] A. Mohamed, S. Watkins, M. Ol, and A. Jones, "Flight-relevant gusts: computation-derived guidelines for micro air vehicle ground test unsteady aerodynamics," *Journal of Aircraft*, vol. 58, no. 3, pp. 693–699, 2021.

[16] J. Bartl, K. F. Sagmo, T. Bracchi, and L. Sætran, "Performance of the nrel s826 airfoil at low to moderate reynolds numbers—a reference experiment for cfd models," *European Journal of Mechanics-B/Fluids*, vol. 75, pp. 180–192, 2019.

[17] D. A. Olson, A. W. Katz, A. M. Naguib, M. M. Koochesfahani, D. P. Rizzetta, and M. R. Visbal, "On the challenges in experimental characterization of flow separation over airfoils at low reynolds number," *Experiments in fluids*, vol. 54, no. 2, pp. 1–11, 2013.

[18] J. G. Coder and M. D. Maughmer, "Comparisons of theoretical methods for predicting airfoil aerodynamic characteristics," *Journal of Aircraft*, vol. 51, no. 1, pp. 183–191, 2014.

[19] S. Aftab, A. Mohd Rafie, N. Razak, and K. Ahmad, "Turbulence model selection for low reynolds number flows," *PloS one*, vol. 11, no. 4, p. e0153755, 2016.

[20] M. Yu and L. Wang, "A high-order flux reconstruction/correction procedure via reconstruction formulation for unsteady incompressible flow on unstructured moving grids," *Computers & Fluids*, vol. 139, pp. 161–173, 2016.

[21] Z. J. Wang and H. Gao, "A unifying lifting collocation penalty formulation including the discontinuous galerkin, spectral volume/difference methods for conservation laws on mixed grids," *Journal of Computational Physics*, vol. 228, no. 21, pp. 8161–8186, 2009.

[22] H. G. Küssner, "Zusammenfassender bericht über den instationären auftrieb von flügeln," *Luftfahrtforschung*, vol. 13, no. 12, pp. 410–424, 1936.

[23] T. H. von Karman and W. R. Sears, "Airfoil theory for non-uniform motion," *Journal of the Aeronautical Sciences*, vol. 5, no. 10, pp. 379–390, 1938.

[24] Z. F. Smith, "Micro air vehicle scale gust-wing interaction in a wind tunnel," Master thesis, University of Maryland, College Park, 2018.

[25] Z. F. Smith, A. R. Jones, and J. T. Hrynuk, "Micro air vehicle scale gust-wing interaction in a wind tunnel," in *2018 AIAA Aerospace Sciences Meeting*, p. 0573, 2018.

[26] J. An, Z. Yan, C. Qiu, and W. Zhou, "The numerical computation of aircraft response to arbitrary vertical gust distributions," *Journal of Aircraft*, vol. 22, no. 11, pp. 988–992, 1985.

[27] Y. Lian and W. Shyy, "Aerodynamics of low reynolds number plunging airfoil under gusty environment," in *45th AIAA Aerospace Sciences Meeting and Exhibit*, p. 71, 2007.

[28] Y. Lian, "Numerical study of a flapping airfoil in gusty environments," in *27th AIAA Applied Aerodynamics Conference*, p. 3952, 2009.

[29] X. Xu, X. Zhu, Z. Zhou, and M. Chang, "Numerical simulation of gust response for uav airfoil," in *Proceedings of the 2010 Asia-Pacific International Symposium on Aerospace Technology*, vol. 1, p. 403, 2010.

[30] C. d. Liauzun, "Aeroelastic response to gust using cfd techniques," in *Fluids Engineering Division Summer Meeting*, vol. 54518, pp. 269–276, 2010.

[31] M. Jones and N. Yamaleev, "The effect of a gust on the flapping wing performance," in *50th AIAA Aerospace Sciences Meeting including the New Horizons Forum and Aerospace Exposition*, p. 1080, 2012.

[32] G. Perrotta and A. R. Jones, "Unsteady forcing on a flat-plate wing in large transverse gusts," *Experiments in Fluids*, vol. 58, no. 8, pp. 1–11, 2017.

[33] S. Corkery, H. Babinsky, and J. Harvey, "On the development and early observations from a towing tank-based transverse wing–gust encounter test rig," *Experiments in Fluids*, vol. 59, no. 9, pp. 1–16, 2018.

[34] N. Poudel, M. Yu, Z. F. Smith, and J. T. Hrynuk, "A combined experimental and computational study of a vertical gust generator in a wind tunnel," in *AIAA Scitech 2019 Forum*, p. 2166, 2019.

[35] H. Biler, G. Sedky, A. R. Jones, M. Saritas, and O. Cetiner, "Experimental investigation of transverse and vortex gust encounters at low reynolds numbers," *AIAA Journal*, vol. 59, no. 3, pp. 786–799, 2021.

[36] I. Andreu-Angulo, H. Babinsky, H. Biler, G. Sedky, and A. R. Jones, "Effect of transverse gust velocity profiles," *AIAA Journal*, vol. 58, no. 12, pp. 5123–5133, 2020.

[37] M. H. Patel and G. Hancock, "A gust tunnel facility," tech. rep., Aeronautical Research Council Reports and Memoranda, 1976.

[38] D. A. Buell, "An experimental investigation of the velocity fluctuations behind oscillating vanes," tech. rep., NASA Technical note NASA TND-5543, 1969.

[39] Y. S. Baik, L. P. Bernal, K. Granlund, and M. V. Ol, "Unsteady force generation and vortex dynamics of pitching and plunging aerofoils," *Journal of Fluid Mechanics*, vol. 709, p. 37, 2012.

[40] H. Biler, C. Badrya, and A. R. Jones, "Experimental and computational investigation of transverse gust encounters," *AIAA Journal*, vol. 57, no. 11, pp. 4608–4622, 2019.

[41] C. Badrya, J. D. Baeder, and A. R. Jones, "Application of prescribed velocity methods to a large-amplitude flat-plate gust encounter," *AIAA Journal*, vol. 57, no. 8, pp. 3261–3273, 2019.

[42] C. Badrya, H. Biler, A. R. Jones, and J. D. Baeder, "Effect of gust width on flat-plate response in large transverse gust," *AIAA Journal*, vol. 59, no. 1, pp. 49–64, 2021.

[43] W. Shyy, D. A. Jenkins, and R. W. Smith, "Study of adaptive shape airfoils at low reynolds number in oscillatory flows," *AIAA journal*, vol. 35, no. 9, pp. 1545–1548, 1997.

[44] R. Prater and Y. Lian, "Aerodynamic response of stationary and flapping wings in oscillatory low reynolds number flows," in *50th AIAA aerospace sciences meeting including the new horizons forum and aerospace exposition*, p. 418, 2012.

[45] Y. Lian and W. Shyy, "Laminar-turbulent transition of a low reynolds number rigid or flexible airfoil," *AIAA journal*, vol. 45, no. 7, pp. 1501–1513, 2007.

[46] T. Gao and X.-Y. Lu, "Insect normal hovering flight in ground effect," *Physics of Fluids*, vol. 20, no. 8, p. 087101, 2008.

[47] A. Fisher, S. Ravi, S. Watkins, J. Watmuff, C. Wang, H. Liu, and P. Petersen, "The gust-mitigating potential of flapping wings," *Bioinspiration & biomimetics*, vol. 11, no. 4, p. 046010, 2016.

[48] J. Vance, I. Faruque, and J. Humbert, "Kinematic strategies for mitigating gust perturbations in insects," *Bioinspiration & biomimetics*, vol. 8, no. 1, p. 016004, 2013.

[49] S. Ravi, J. D. Crall, L. McNeilly, S. F. Gagliardi, A. A. Biewener, and S. A. Combes, “Hummingbird flight stability and control in freestream turbulent winds,” *Journal of Experimental Biology*, vol. 218, no. 9, pp. 1444–1452, 2015.

[50] S. Ravi, D. Kolomenskiy, T. Engels, K. Schneider, C. Wang, J. Sesterhenn, and H. Liu, “Bumblebees minimize control challenges by combining active and passive modes in unsteady winds,” *Scientific reports*, vol. 6, no. 1, pp. 1–10, 2016.

[51] P. Chirarattananon, Y. Chen, E. F. Helbling, K. Y. Ma, R. Cheng, and R. J. Wood, “Dynamics and flight control of a flapping-wing robotic insect in the presence of wind gusts,” *Interface focus*, vol. 7, no. 1, p. 20160080, 2017.

[52] M. Gu, J. Wu, and Y. Zhang, “Wing rapid responses and aerodynamics of fruit flies during headwind gust perturbations,” *Bioinspiration & Biomimetics*, vol. 15, no. 5, p. 056001, 2020.

[53] H. Liu, D. Kolomenskiy, T. Nakata, and G. Li, “Unsteady bio-fluid dynamics in flying and swimming,” *Acta Mechanica Sinica*, vol. 33, no. 4, pp. 663–684, 2017.

[54] V. M. Ortega-Jimenez, J. S. Greeter, R. Mittal, and T. L. Hedrick, “Hawkmoth flight stability in turbulent vortex streets,” *Journal of Experimental Biology*, vol. 216, no. 24, pp. 4567–4579, 2013.

[55] V. M. Ortega-Jimenez, N. Sapir, M. Wolf, E. A. Variano, and R. Dudley, “Into turbulent air: size-dependent effects of von kármán vortex streets on hummingbird flight kinematics and energetics,” *Proceedings of the Royal Society B: Biological Sciences*, vol. 281, no. 1783, p. 20140180, 2014.

[56] V. M. Ortega-Jimenez, M. Badger, H. Wang, and R. Dudley, “Into rude air: hummingbird flight performance in variable aerial environments,” *Philosophical Transactions of the Royal Society B: Biological Sciences*, vol. 371, no. 1704, p. 20150387, 2016.

[57] T. Engels, D. Kolomenskiy, K. Schneider, F.-O. Lehmann, and J. Sesterhenn, “Bumblebee flight in heavy turbulence,” *Physical review letters*, vol. 116, no. 2, p. 028103, 2016.

[58] J. Crall, J. Chang, R. Oppenheimer, and S. Combes, “Foraging in an unsteady world: bumblebee flight performance in field-realistic turbulence,” *Interface Focus*, vol. 7, no. 1, p. 20160086, 2017.

[59] J. A. Cheney, J. P. Stevenson, N. E. Durston, J. Song, J. R. Usherwood, R. J. Bomphrey, and S. P. Windsor, “Bird wings act as a suspension system that rejects gusts,” *Proceedings of the Royal Society B*, vol. 287, no. 1937, p. 20201748, 2020.

[60] T. Nakata, R. Noda, S. Kumagai, and H. Liu, "A simulation-based study on longitudinal gust response of flexible flapping wings," *Acta Mechanica Sinica*, vol. 34, no. 6, pp. 1048–1060, 2018.

[61] M. A. Badger, H. Wang, and R. Dudley, "Avoiding topsy-turvy: how anna's hummingbirds (calypte anna) fly through upward gusts," *Journal of Experimental Biology*, vol. 222, no. 3, 2019.

[62] T. Jakobi, D. Kolomenskiy, T. Ikeda, S. Watkins, A. Fisher, H. Liu, and S. Ravi, "Bees with attitude: the effects of directed gusts on flight trajectories," *Biology open*, vol. 7, no. 10, 2018.

[63] D. Favier, C. Maresca, and J. Rebont, "Dynamic stall due to fluctuations of velocity and incidence," *AIAA Journal*, vol. 20, no. 7, pp. 865–871, 1982.

[64] Z.-W. Shi and X. Ming, "Effects of unsteady freestream on aerodynamic characteristics of a pitching delta wing," *Journal of Aircraft*, vol. 45, no. 6, pp. 2182–2185, 2008.

[65] Z. Shi and X. Ming, "Experimental investigation on a pitching motion delta wing in unsteady free stream," *Modern Physics Letters B*, vol. 23, no. 03, pp. 409–412, 2009.

[66] K. Gharali and D. A. Johnson, "Dynamic stall simulation of a pitching airfoil under unsteady freestream velocity," *Journal of Fluids and Structures*, vol. 42, pp. 228–244, 2013.

[67] J. Yu, T. Leu, and J.-J. Miau, "Investigation of reduced frequency and freestream turbulence effects on dynamic stall of a pitching airfoil," *Journal of Visualization*, vol. 20, no. 1, pp. 31–44, 2017.

[68] X. Amandolese and E. Széchényi, "Experimental study of the effect of turbulence on a section model blade oscillating in stall," *Wind Energy: An International Journal for Progress and Applications in Wind Power Conversion Technology*, vol. 7, no. 4, pp. 267–282, 2004.

[69] Q. Li, Y. Kamada, T. Maeda, J. Murata, and Y. Nishida, "Effect of turbulent inflows on airfoil performance for a horizontal axis wind turbine at low reynolds numbers (part ii: Dynamic pressure measurement)," *Energy*, vol. 112, pp. 574–587, 2016.

[70] J. M. Chen and C.-C. Choa, "Freestream disturbance effects on an airfoil pitching at constant rate," *Journal of aircraft*, vol. 36, no. 3, pp. 507–514, 1999.

[71] B. E. Merrill and Y. T. Peet, "Effect of impinging wake turbulence on the dynamic stall of a pitching airfoil," *AIAA journal*, vol. 55, no. 12, pp. 4094–4112, 2017.

[72] T. S. Leu, J. Yu, C. Hu, J. Miau, S. Liang, J. Li, J. Cheng, and S. Chen, "Experimental study of free stream turbulent effects on dynamic stall of pitching airfoil by using particle image velocimetry," in *Applied Mechanics and Materials*, vol. 225, pp. 103–108, Trans Tech Publ, 2012.

[73] R. N. Conger and B. Ramaprian, "Pressure measurements on a pitching airfoil in a water channel," *AIAA journal*, vol. 32, no. 1, pp. 108–115, 1994.

[74] N. J. Kay, P. J. Richards, and R. N. Sharma, "Effect of turbulence and sinusoidal pitching on low-reynolds-number lift," *AIAA Journal*, vol. 58, no. 6, pp. 2377–2387, 2020.

[75] R. Gopalkrishnan, M. S. Triantafyllou, G. S. Triantafyllou, and D. Barrett, "Active vorticity control in a shear flow using a flapping foil," *Journal of Fluid Mechanics*, vol. 274, pp. 1–21, 1994.

[76] J. C. Liao, D. N. Beal, G. V. Lauder, and M. S. Triantafyllou, "Fish exploiting vortices decrease muscle activity," *Science*, vol. 302, no. 5650, pp. 1566–1569, 2003.

[77] J. C. Liao, D. N. Beal, G. V. Lauder, and M. S. Triantafyllou, "The kármán gait: novel body kinematics of rainbow trout swimming in a vortex street," *Journal of experimental biology*, vol. 206, no. 6, pp. 1059–1073, 2003.

[78] Q. Liao, G.-J. Dong, and X.-Y. Lu, "Vortex formation and force characteristics of a foil in the wake of a circular cylinder," *Journal of fluids and structures*, vol. 19, no. 4, pp. 491–510, 2004.

[79] O. Akanyeti and J. C. Liao, "A kinematic model of kármán gaiting in rainbow trout," *Journal of Experimental Biology*, vol. 216, no. 24, pp. 4666–4677, 2013.

[80] L.-M. Chao, D. Zhang, Y.-H. Cao, and G. Pan, "Numerical studies on the interaction between two parallel d-cylinder and oscillated foil," *Modern Physics Letters B*, vol. 32, no. 06, p. 1850034, 2018.

[81] Q. Xiao, K. Sun, H. Liu, and J. Hu, "Computational study on near wake interaction between undulation body and a d-section cylinder," *Ocean Engineering*, vol. 38, no. 4, pp. 673–683, 2011.

[82] X.-m. Shao and D.-y. Pan, "Hydrodynamics of a flapping foil in the wake of a d-section cylinder," *Journal of Hydrodynamics, Ser. B*, vol. 23, no. 4, pp. 422–430, 2011.

[83] C. Li, W. Yang, X. Xu, J. Wang, M. Wang, and L. Xu, "Numerical investigation of fish exploiting vortices based on the kármán gaiting model," *Ocean Engineering*, vol. 140, pp. 7–18, 2017.

[84] X. Shao, D. Pan, J. Deng, and Z. Yu, "Hydrodynamic performance of a fishlike undulating foil in the wake of a cylinder," *Physics of Fluids*, vol. 22, no. 11, p. 111903, 2010.

[85] J. Stack, "Tests in the variable density wind tunnel to investigate the effects of scale and turbulence on airfoil characteristics," Tech. Rep. 364, NACA, 1931.

[86] T. J. Mueller, L. J. Pohlen, P. E. Conigliaro, and B. J. Jansen, "The influence of free-stream disturbances on low reynolds number airfoil experiments," *Experiments in Fluids*, vol. 1, no. 1, pp. 3–14, 1983.

[87] J. A. Hoffmann, "Effects of freestream turbulence on the performance characteristics of an airfoil," *AIAA journal*, vol. 29, no. 9, pp. 1353–1354, 1991.

[88] E. Laitone, "Wind tunnel tests of wings at reynolds numbers below 70 000," *Experiments in fluids*, vol. 23, no. 5, pp. 405–409, 1997.

[89] P. Mish and W. Devenport, "Mean loading effects on the surface pressure fluctuations on an airfoil in turbulence," in *7th AIAA/CEAS Aeroacoustics Conference and Exhibit*, p. 2211, 2001.

[90] L. Gilling, N. Sørensen, and L. Davidson, "Detached eddy simulations of an airfoil in turbulent inflow," in *47th AIAA Aerospace Sciences Meeting Including The New Horizons Forum and Aerospace Exposition*, p. 270, 2009.

[91] R. F. Huang and H. W. Lee, "Effects of freestream turbulence on wing-surface flow and aerodynamic performance," *Journal of aircraft*, vol. 36, no. 6, pp. 965–972, 1999.

[92] S. Wang, Y. Zhou, M. M. Alam, and H. Yang, "Turbulent intensity and reynolds number effects on an airfoil at low reynolds numbers," *Physics of Fluids*, vol. 26, no. 11, p. 115107, 2014.

[93] P. Devinant, T. Laverne, and J. Hureau, "Experimental study of wind-turbine airfoil aerodynamics in high turbulence," *Journal of Wind Engineering and Industrial Aerodynamics*, vol. 90, no. 6, pp. 689–707, 2002.

[94] E. Cruz, *The effect of turbulence on micro air vehicle airfoils*. PhD thesis, RMIT University, 2012.

[95] C. Sicot, S. Aubrun, S. Loyer, and P. Devinant, "Unsteady characteristics of the static stall of an airfoil subjected to freestream turbulence level up to 16%," *Experiments in fluids*, vol. 41, no. 4, pp. 641–648, 2006.

[96] T. Tsuchiya, D. Numata, T. Suwa, and K. Asai, "Influence of turbulence intensity on aerodynamic characteristics of an naca 0012 at low reynolds numbers," in *51st AIAA Aerospace Sciences Meeting Including the New Horizons Forum and Aerospace Exposition*, p. 65, 2013.

[97] S. Ravi, S. Watkins, J. Watmuff, K. Massey, M. Marino, and P. Petersen, "Influence of turbulence intensity on the flow structure over a thin airfoil at lower reynolds numbers," in *28th Congress of the International Council of the Aeronautical Sciences 2012*, pp. 946–954, ICAS Brisbane, Australia, 2012.

[98] J. Delnero, J. Marañon di Leo, F. Bacchi, J. Colman, and U. Boldes, "Experimental determination of the influence of turbulent scale on the lift and drag coefficients of low reynolds number airfoils," *Latin American applied research*, vol. 35, no. 3, pp. 183–188, 2005.

[99] M. Breuer, "Effect of inflow turbulence on an airfoil flow with laminar separation bubble: An les study," *Flow, Turbulence and Combustion*, vol. 101, no. 2, pp. 433–456, 2018.

[100] Z. Yang and I. E. Abdalla, "Effects of free-stream turbulence on a transitional separated–reattached flow over a flat plate with a sharp leading edge," *International Journal of Heat and Fluid Flow*, vol. 30, no. 5, pp. 1026–1035, 2009.

[101] W. Balzer and H. Fasel, "Numerical investigation of the role of free-stream turbulence in boundary-layer separation," *Journal of Fluid Mechanics*, vol. 801, pp. 289–321, 2016.

[102] S. Hosseinverdi and H. F. Fasel, "Numerical investigation of laminar–turbulent transition in laminar separation bubbles: the effect of free-stream turbulence," *Journal of Fluid Mechanics*, vol. 858, pp. 714–759, 2019.

[103] G. Sedky, F. D. Lagor, and A. Jones, "Unsteady aerodynamics of lift regulation during a transverse gust encounter," *Physical Review Fluids*, vol. 5, no. 7, p. 074701, 2020.

[104] G. Sedky, A. R. Jones, and F. D. Lagor, "Lift regulation during transverse gust encounters using a modified goman–khrabrov model," *AIAA Journal*, vol. 58, no. 9, pp. 3788–3798, 2020.

[105] I. Andreu Angulo and H. Babinsky, "Negating gust effects by actively pitching a wing," in *AIAA Scitech 2020 Forum*, p. 1057, 2020.

[106] I. Andreu Angulo and H. Babinsky, "Unsteady modelling of pitching wings for gust mitigation," in *AIAA Scitech 2021 Forum*, p. 1999, 2021.

[107] M. R. Visbal, "High-fidelity simulation of transitional flows past a plunging airfoil," *AIAA journal*, vol. 47, no. 11, pp. 2685–2697, 2009.

[108] L. Wang and M. Yu, "Comparison of row, esdirk, and bdf2 for unsteady flows with the high-order flux reconstruction formulation," *Journal of Scientific Computing*, vol. 83, pp. 1–27, 2020.

[109] L. Wang and M. Yu, "An implicit high-order preconditioned flux reconstruction method for low-mach-number flow simulation with dynamic meshes," *International Journal for Numerical Methods in Fluids*, vol. 91, no. 7, pp. 348–366, 2019.

[110] L. Wang and M. Yu, "On the parallel implementation and performance study of high-order rosenbrock-type implicit runge-kutta methods for the fr/cpr solutions of the navier-stokes equations," in *2018 AIAA Aerospace Sciences Meeting*, p. 1095, 2018.

[111] M. Yu, Z. Wang, and H. Hu, "A high-order spectral difference method for unstructured dynamic grids," *Computers & Fluids*, vol. 48, no. 1, pp. 84–97, 2011.

[112] H. T. Huynh, "A flux reconstruction approach to high-order schemes including discontinuous galerkin methods," in *18th AIAA Computational Fluid Dynamics Conference*, p. 4079, 2007.

[113] P. E. Vincent, P. Castonguay, and A. Jameson, "A new class of high-order energy stable flux reconstruction schemes," *Journal of Scientific Computing*, vol. 47, no. 1, pp. 50–72, 2011.

[114] L. Wang and M. Yu, "Jacobian-free implicit p-adaptive high-order compact direct flux reconstruction methods for unsteady flow simulation," in *AIAA Aviation 2019 Forum*, p. 3062, 2019.

[115] P. L. Roe, "Approximate riemann solvers, parameter vectors, and difference schemes," *Journal of computational physics*, vol. 43, no. 2, pp. 357–372, 1981.

[116] F. Bassi, A. Crivellini, S. Rebay, and M. Savini, "Discontinuous galerkin solution of the reynolds-averaged navier–stokes and k–ω turbulence model equations," *Computers & Fluids*, vol. 34, no. 4, pp. 507–540, 2005.

[117] M. Yu, Z. Wang, and Y. Liu, "On the accuracy and efficiency of discontinuous galerkin, spectral difference and correction procedure via reconstruction methods," *Journal of Computational Physics*, vol. 259, pp. 70–95, 2014.

[118] P.-O. Persson, J. Bonet, and J. Peraire, "Discontinuous galerkin solution of the navier–stokes equations on deformable domains," *Computer Methods in Applied Mechanics and Engineering*, vol. 198, no. 17-20, pp. 1585–1595, 2009.

[119] P. R. Hammer, M. R. Visbal, A. M. Naguib, and M. M. Koochesfahani, "Lift on a steady 2-d symmetric airfoil in viscous uniform shear flow," *Journal of Fluid Mechanics*, vol. 837, 2018.

[120] H. Liu and K. Kawachi, "A numerical study of undulatory swimming," *Journal of Computational Physics*, vol. 155, no. 2, pp. 223–247, 1999.

[121] J. Young and J. C. Lai, "Oscillation frequency and amplitude effects on the wake of a plunging airfoil," *AIAA journal*, vol. 42, no. 10, pp. 2042–2052, 2004.

[122] P. R. Hammer, *Computational study of the effect of Reynolds number and motion trajectory asymmetry on the aerodynamics of a pitching airfoil at low Reynolds number*. Ph.D. thesis, Michigan State University, 2016.

[123] U. Senturk and A. J. Smits, "Reynolds number scaling of the propulsive performance of a pitching airfoil," *AIAA Journal*, vol. 57, no. 7, pp. 2663–2669, 2019.

[124] A. R. Jones, "Gust encounters of rigid wings: Taming the parameter space," *Physical Review Fluids*, vol. 5, no. 11, p. 110513, 2020.

[125] J. Eldredge, C. Wang, and M. Ol, "A computational study of a canonical pitch-up, pitch-down wing maneuver," in *39th AIAA fluid dynamics conference*, p. 3687, 2009.

[126] D. J. Garmann, M. R. Visbal, and P. D. Orkwis, "Three-dimensional flow structure and aerodynamic loading on a revolving wing," *Physics of Fluids*, vol. 25, no. 3, p. 034101, 2013.

[127] N. Poudel, M. Yu, and J. T. Hrynuk, "Computational study on the effects of unsteady freestream on an airfoil performance at low reynolds numbers," in *AIAA Scitech 2021 Forum*, p. 0965, 2021.

[128] N. Poudel, M. Yu, and J. T. Hrynuk, "Gust mitigation with an oscillating airfoil at low reynolds number," *Physics of Fluids*, vol. 33, no. 10, p. 101905, 2021.

[129] M. Yu, B. Wang, Z. Wang, and S. Farokhi, "Evolution of vortex structures over flapping foils in shear flows and its impact on aerodynamic performance," *Journal of Fluids and Structures*, vol. 76, pp. 116–134, 2018.

[130] D. Floryan, T. Van Buren, C. W. Rowley, and A. J. Smits, "Scaling the propulsive performance of heaving and pitching foils," *Journal of Fluid Mechanics*, vol. 822, pp. 386–397, 2017.

[131] M. A. Prsic, M. C. Ong, B. Pettersen, and D. Myrhaug, "Large eddy simulations of flow around a smooth circular cylinder in a uniform current in the subcritical flow regime," *Ocean engineering*, vol. 77, pp. 61–73, 2014.

[132] Y. Zhang and K. Zhao, "The influence of reynolds number on boundary layer development and stall characteristics of airfoil," *Advances in Aeronautical Science and Engineering*, vol. 10, no. 3, pp. 319–329, 2019.